5-2021

Electrochemical Oxidation of Individual Silver Nanoparticles: Exploring the Effect of Particle Shape, Capping Ligand, Electrolyte, and Potential on the Signal

Jazlynn Sikes
University of Arkansas, Fayetteville

Electrochemical Oxidation of Individual Silver Nanoparticles: Exploring the Effect of Particle Shape, Capping Ligand, Electrolyte, and Potential on the Signal

A dissertation submitted in partial fulfillment
of the requirements for the degree of
Doctor of Philosophy in Chemistry

by

Jazlynn Sikes
Arkansas Tech University
Bachelor of Science in Chemistry, 2013

May 2021
University of Arkansas

This dissertation is approved for recommendation to the Graduate Council.

_____
Ingrid Fritsch, Ph.D.
Dissertation Director

_____   _____
Bill Durham, Ph.D.   David Paul, Ph.D.
Committee Member   Committee Member

_____
Julie Stenken, Ph.D.
Committee Member

Abstract

Nanomaterials have revolutionized science and technology. Their unique properties can be exploited, and nanoparticles are being used as catalysts, antimicrobials, drug delivery vehicles, sensors, and more. However, the fundamental properties of nanomaterials and their interactions with their surrounding environments are still poorly understood. In this work, a single-particle approach was used to observe the effects of capping ligand, surrounding solution, and particle shape on the oxidative process to gain deeper understanding of silver nanoparticle properties. When allowed the opportunity, the particles will adsorb to the electrode surface then oxidize in rapid succession upon electrode activation, regardless of capping ligand as long as the electrolyte and applied potential are appropriate. The presence of potassium chloride encourages the oxidation of polyethylene glycol capped particles at an increasing rate over time, but rarely allows oxidation poly-vinylpyrrolidone capped particles. Instead, these particles are better oxidized to silver oxide either in potassium nitrate at high potentials or under alkaline conditions at lower potentials. Successful oxidation of poly-vinylpyrrolidone capped particles enabled the work to be expanded from spheres to cubes and plates, the shape of which bore no effect on the rate of oxidation to silver chloride. Furthermore, a new method of single particle characterization was developed to improve the accuracy and precision of nanoparticle characterization. By combining redox magnetohydrodynamics with dark field microscopy, silver and gold coated silica particles were successfully sized from a flowing mixture in both forward and reverse directions.

Acknowledgements

I would like to give thanks to my advisor, Dr. Ingrid Fritsch, for the guidance, words of wisdom, and support through the years. She has not only provided technical and scientific advice, but has also offered countless words of encouragement throughout this process and has taught me how to "listen to the data," and "the data doesn't lie, we just don't know what it's telling us." I also thank my committee members, Dr. Bill Durham, Dr. David Paul, and Dr. Julie Stenken for their input, advice, and always providing very constructive criticism during every annual meeting and seminar presentation; all have made me a better scientist. I acknowledge my lab mates for their continuous friendship and support.

Thanks to Dr. Prof. Kristina Tschulik at Ruhr Universität Bochum in Bochum, Germany for hosting me in her lab during Spring of 2019, and for the advice she has continued to give during our ongoing collaboration. I also am forever appreciative of the generosity her lab members showed to me during this time and the friendships which have followed me home. Special thanks are due to her student, Kannasoot Kanokkanchana, for allowing me to beta test the NanoDAQ2 which he built. This study abroad was funded by the Sturgis International Fellowship, a grant made possible by the generous support of the Roy and Christine Sturgis Charitable Trust

Last but not least, special thanks my husband, parents, and family for always supporting my goals and ambitions. They have all been great cheerleaders not only through this process, but throughout my entire life.

Table of Contents

Introduction

While nanoparticle research has only occurred for a few decades, the incorporation of metallic nanoparticles into objects dates back centuries due to the vibrant colors exhibited by metals such as silver and gold while in the nano phase.[1] However, color is not the only property in which nanoparticles differ from bulk phase materials. And as with centuries ago, today's nanoparticles are incorporated into consumer goods even though their chemical properties and reactivity are poorly understood.[2-4] The number of nanomaterial-containing products has been increasing for the past few decades, so that now thousands of commercial products contain nanomaterials. Of the many types of nanomaterials in use, silver nanoparticles are in more commercially available goods than any other nanomaterial.[2, 5]

Silver nanoparticles are widely available in bandages, medical equipment, cosmetics, and clothing due to its antimicrobial properties,[6-8] For more industrial purposes, catalytic properties of silver nanoparticles are also of interest [9-11] due to its ability to catalyze reactions attractive for alternative fuel cells, such as water splitting and alcohol oxidation, while being much cheaper than platinum.[12-15] Because nanoparticles have more surface sites on which catalysis can occur for less total metal mass than bulk materials, the cost is drastically decreased.

As a single aspect (e.g. size, shape, capping ligand) of the nanoparticle changes, properties such as catalytic abilities and toxicity also change.[3, 4, 16, 17] This means that alteration of the shape, size, capping ligand, and/or surrounding environment of a silver nanoparticle can lead to different behaviors and properties.[16, 18, 19 16, 20, 21] For example, cubes have been shown to better catalyze the oxygen reduction reaction than spheres of the same size by nearly 25%.[22] Because silver nanoparticles are produced using a wide variety of capping ligands, shapes, and sizes, it is imperative to understand the fundamentals of how and why morphology and surface

functionalization changes lead to behavior changes. Citrate capped particles are the most common due to their ease of synthesis and uninhibited surfaces. When biological applications are being considered, polyethylene glycol (PEG) capped particles are often used instead due to the low toxicity and ease of functionalization of the PEG.[23, 24] If shapes other than spheres are of interest, poly-vinylpyrrolidone (PVP) is often the default capping ligand due to its required presence during the synthesis.[25] Experiments described herein were performed on particles containing a citrate, PEG, or PVP capping ligand for the purpose of characterizing the particles themselves and understanding their interactions with their surroundings.

Most commercial methods of characterizing silver nanoparticles, such as dynamic light scattering for particle sizing, inductively coupled plasmon spectroscopy and atomic absorption spectroscopy for metal content determination, and UV-vis spectroscopy for optical property determination and monitoring suspension stability over time provide only an average over the entire sample, instead of information about the individual particles. However, unlike molecules in a solution, nanoparticles in suspension are analogous to a population of people - each particle in the sample is unique. Transmission electron spectroscopy and atomic force microscopy individual particle sizing information, and single particle inductively coupled plasmon spectroscopy the silver content of individual particles but give little-to-no insight into the *properties* of the particles. Electrochemical methods have been utilized to analyze the catalytic efficiency of materials for decades and can be used to probe several properties of individual nanoparticles - size, catalytic abilities, oxidative mechanism, particle stability, etc. - providing more overall information than any of the previously listed methods of particle characterization.

To investigate how changing the morphology and/or environment of silver nanomaterials affects their properties, electrochemical methods were employed. Electrochemical properties of

individual silver nanoparticles can be observed using chronoamperometry via non-destructive electrocatalytic amplification[26, 27] or by destructive oxidation of the particle itself.[28, 29] Experiments herein utilized the destructive method of particle oxidation to investigate the size and oxidizability of individual polyethylene glycol capped silver nanoparticles (PEG-AgNS), as the destructive method provides both characteristic information about the particle itself and insight into the mechanism of silver nanoparticle oxidation.[30-33] When the silver particle encounters an electrode held at an adequate potential (chronoamperometry), oxidation can occur, which results in a brief spike in the measured current (Figure 1). The current spike is directly indicative of how much silver was oxidized during the contact with the electrode and can be used to determine the size of the particle or the extent of particle oxidation. Three routes of particle oxidation are possible; complete oxidation in a one-step manner, complete oxidation in a multi-step manner,[29, 34] or partial oxidation followed by diffusion from the surface. Knowing the particle size beforehand allows for the development of methods that will promote complete one-step oxidation. The electrode material, surrounding electrolyte, and method of sample preparation all affect the extent of particle oxidation.

Simply holding the electrode at a potential kinetically capable of oxidizing the particle will not necessarily result in oxidation upon contact with the electrode. The barrier imposed by the capping ligand is one of the factors hindering oxidation. Electron tunneling distances generally are on the scale of angstroms[35] but nanoparticle capping ligands are generally nanometers thick. Once the oxidation method is refined, electrochemistry can provide a cheap method of sizing single nanoparticles and observing their catalytic effects on an individual level. Additionally, the conditions which promote partial vs. complete oxidation can be investigated, providing valuable insight into the interactions of particles with their surroundings.

Because a single nanoparticle contains 10^4-10^6 atoms of silver depending on the particle size and material, particle oxidation generally occurs within a few milliseconds and the maximum current achieved is usually in the picoampere or low nanoampere regions. Consequently, potentiostats must be capable of collecting thousands of data points per seconds while simultaneously having very low background electronic noise, and peak distortion must be carefully monitored. Until very recently, the instrumentation and electronics has been incapable of reliably detecting signals from the oxidation of *individual* particles due to the rapid oxidation and low currents pushing the limits of instrument capabilities because most instruments were not built for rapid sub-nanoampere measurements, and the first single particle oxidation papers were published in 2011. Additionally, early papers were published at a temporal resolution that only collected fewer than 10 data points per particle. Data published more recently has been collected with much greater temporal resolution, which provides much more information about the particle oxidation, but it has been largely limited to citrate-capped particles. As a result, how modifications to the particle surface, environment, electrode, etc. affect the signal produced are very poorly understood and require further investigation.

Further complicating matters, particle oxidation does not always occur upon contact with the electrode, and the multitude of factors which can hinder oxidation are still being discovered and investigated.[36, 37] It has been observed that the presence of capping ligands and/or electrolytes which form soluble silver complexes can hinder oxidation.[32, 33, 38] However, oxidation of citrate-capped particles in the appropriate electrolytes often still show evidence of a barrier to oxidation, and these barriers are not well understood. Surface fouling of the electrode is one culprit that hinders oxidation of the electrode, which is difficult to control, especially on the microdisk electrodes required for these types of experiments. Other methods of

understanding barriers to electrooxidation, which will provide more reproducible results, must be further researched and developed.

Overview of the studies described herein

The following work describes in-depth single particle analysis of several types of silver nanoparticles. Because single particle analysis pushes the limits of commercial instrumentation, data analysis must be approached with caution, as described in Chapter 1. Inadequate data transfer rates of older instruments resulted in "long" time gaps between the ending of one experiment and beginning of another. The oxidation frequency on each chronoamperogram (CA) was analyzed in 0.1 s intervals. The results initially indicated an apparent Cottrellian-like pattern of particle oxidation. However, this was found to actually be the result of particle adsorption to the electrode surface during the data transfer time. The absorbed particles oxidized in a rapid succession during the first second after the electrode was stepped to an oxidizing potential.

The work was then expanded to the relationship between time and oxidation frequency of PEG-AgNS in KCl over *several* CAs. When placed into groups of 10, it was observed that the first groups contained fewer particle oxidations than the later groups of 10. This relationship was determined to not be also due to absorption, but rather due to the chemistry between PEG and KCl.

Successful oxidations of the PEG-AgNS in KCl and unsuccessful oxidation of PVP-AgNS in KCl created curiosity as to why KCl allows the oxidation of one polymer capped particle but not the other. Literature indicated that KCl is a "salting-in" electrolyte to PEG, but "salting-out" to PVP. [39] Chapter 2 explores the effect of "salting-in" electrolytes on PVP-AgNS and concluded that "salting-in" properties do not inherently encourage particle oxidation. Therefore, methods of PVP-AgNP oxidation still needed to be developed.

Chapter 3 outlines not only the successful oxidation of PVP-AgNP, but also explores the effect of particle shape on the oxidation rate. Oxidation of PVP silver nanospheres (AgNS), nanocubes (AgNC), and nanoplates (AgNPl) indicated that particle shape, and thus particle surface area, does not affect the oxidation rate of silver to silver oxide. Chapter 4 expands the exploration to alkaline conditions, where the mechanism of oxidation to silver oxide is different than in the absence of added acid or base. Under these conditions, the oxidation rate remained independent of particle shape.

The methods described so far involve destructive characterization of the particles. A non-destructive method of particle characterization was developed and is described in Chapter 5. Redox magnetohydrodynamics was paired with dark field microscopy for the simultaneous sizing of gold coated silica and silver nanoparticles. One-dimensional mean square displacement was used to extract the diffusion coefficients (and therefore sizes) of the individual particles in the flowing suspension. Pumping was performed in two directions, allowing for reanalysis of particles to occur.

References

1.   Freestone, I.; Meeks, N.; Sax, M.; Higgitt, C., The Lycurgus Cup - A Roman nanotechnology. *Gold Bulletin* **2007,** *40* (4), 270-277.

2.   Vance, M. E.; Kuiken, T.; Verjerano, E. P.; McGinnis, S. P.; Hochella, M. F.; Rejeski, D.; Hull, M. S., Nanotechnology in the real world: Redeveloping the nanomaterial consumer products inventory. *Bielstein Journal of Nanotechnology* **2015,** *5*, 1769-1780.

3.   Kelly, K.; Coronado, E.; Zhao, L.; Schatz, G., The optical properties of metal nanoparticles: The influence of size, shape, and dielectric environment. *Journal of Physical Chemistry B* **2003,** *107* (3), 668-677.

4.   Liz-Marzán*, L. M., Tailoring Surface Plasmons through the Morphology and Assembly of Metal Nanoparticles. *Langmuir* **2006,** *22* (1), 32-41.

5.   ANEC; Organization, T. E. C. s. How much nano do we buy? http://www.beuc.eu/publications/2010-00645-01-e.pdf.

6.   Dakal, T.; Kumar, A.; Majumdar, R.; Yadav, V., Mechanistic Basis of Antimicrobial Actions of Silver Nanoparticles. *Frontiers in Microbiology* **2016,** *7*.

7.   El Arrassi, A.; Bellova, P.; Javid, S.; Motemani, Y.; Khare, C.; Sengstock, C.; Koller, M.; Ludwig, A.; Tschulik, K., A Unified Interdisciplinary Approach to Design Antibacterial Coatings for Fast Silver Release. *Chemelectrochem* **2017,** *4* (8), 1975-1983.

8.   Loza, K.; Diendorf, J.; Sengstock, C.; Ruiz-Gonzalez, L.; Gonzalez-Calbet, J.; Vallet-Regi, M.; Koller, M.; Epple, M., The dissolution and biological effects of silver nanoparticles in biological media. *Journal of Materials Chemistry B* **2014,** *2* (12), 1634-1643.

9.   Herves, P.; Perez-Lorenzo, M.; Liz-Marzan, L.; Dzubiella, J.; Lu, Y.; Ballauff, M., Catalysis by metallic nanoparticles in aqueous solution: model reactions. *Chemical Society Reviews* **2012,** *41* (17), 5577-5587.

10.   Ananikov, V. P.; Beletskaya, I. P., Toward the Ideal Catalyst: From Atomic Centers to a "Cocktail" of Catalysts. *Organometallics* **2012,** *31* (5), 1595-1604.

11.   Wildgoose, G. G.; E., C.; Compton, R. G., Metal Nanoparticles and Related Materials Supported on Carbon Nanotubes: Methods and Applications. *Small* **2005,** *2* (2), 182-193.

12.   Joya, K.; Ahmad, Z.; Joya, Y.; Garcia-Esparza, A.; de Groot, H., Efficient electrochemical water oxidation in neutral and near-neutral systems with a nanoscale silver-oxide catalyst. *Nanoscale* **2016,** *8* (32), 15033-15040.

13.   Li, D.; Wei, C.; Wang, Q.; Liu, L.; Zhong, D.; Hao, G.; Zuo, Z.; Zhao, Q., Oxygen Evolution on in Situ Selective Formation of AgO: Plane Is the Key Factor. *Journal of Physical Chemistry C* **2019,** *123* (17), 10967-10973.

14.   Kohler, J.; Abahmane, L.; Wagner, J.; Albert, J.; Mayer, G., Preparation of metal nanoparticles with varied composition for catalytical applications in microreactors. *Chemical Engineering Science* **2008,** *63* (20), 5048-5055.

15.   Mitsudome, T.; Mikami, Y.; Funai, H.; Mizugaki, T.; Jitsukawa, K.; Kaneda, K., Heterogeneous catalysis - Oxidant-free alcohol dehydrogenation using a reusable hydrotalcite-supported silver nanoparticle catalyst. *Angewandte Chemie-International Edition* **2008,** *47* (1), 138-141.

16.   and, R. N.; El-Sayed, M. A., Shape-Dependent Catalytic Activity of Platinum Nanoparticles in Colloidal Solution. *Nano Letters* **2004,** *4* (7), 1343-1348.

17.   Leif J. Sherry; Shih-Hui Chang; George C. Schatz, a.; Duyne*, R. P. V.; and, B. J. W.; Xia, Y., Localized Surface Plasmon Resonance Spectroscopy of Single Silver Nanocubes. *Nano Letters* **2005,** *5* (10), 2034-2038.

18.   Gorka, D. E.; Osterberg, J. S.; Gwin, C. A.; Colman, B. P.; Meyer, J. N.; Bernhardt, E. S.; Gunsch, C. K.; DiGulio, R. T.; Liu, J., Reducing Environmental Toxicity of Silver Nanoparticles through Shape Control. *Environmental Science & Technology* **2015,** *49*, 10093-10092.

19.   Jimenez-Lamana, J.; Slaveykova, V., Silver nanoparticle behaviour in lake water depends on their surface coating. *Science of the Total Environment* **2016,** *573*, 946-953.

20.   Bansal, V.; Li, V.; O'Mullane, A. P.; Bhargava, S. K., Shape dependent electrocatalytic behaviour of silver nanoparticles. *CrystEngComm* **2010,** *12*, 4280-4286.

21.   Krause, K. J.; Brings, F.; Schnitker, J.; Kätelhön, E.; Rinklin, P.; Compton, R. G.; Lemay, S. G.; Wolfrum, B., The Influence of Supporting Ions on the Electrochemical Detection of Individual Silver Nanoparticles: Understanding the Shape and Frequency of Current Transients in Nano-impacts. *Chemistry - A European Journal* **2017,** *23* (19), 4638-4643.

22.   Lee, C.-L.; Tsai, Y.-L.; Huang, C.-H.; Huang D, K.-L., Performance of silver nanocubes based on electrochemical surface area for catalyzing oxygen reduction reaction. *Electrochemistry Communications* **2013,** *29*, 37–40.

23.   Kumar, S.; Alnasif, N.; Fleige, E.; Kurniasih, I.; Kral, V.; Haase, A.; Luch, A.; Weindl, G.; Haag, R.; Schafer-Korting, M.; Hedtrich, S., Impact of structural differences in hyperbranched polyglycerol-polyethylene glycol nanoparticles on dermal drug delivery and biocompatibility. *Eur J Pharm Biopharm* **2014,** *88* (3), 625-34.

24.   Barrios-Gumiel, A.; Sanchez-Nieves, J.; Pérez-Serrano, J.; Gómez, R.; de la Mata, F. J., PEGylated AgNP covered with cationic carbosilane dendrons to enhance antibacterial and inhibition of biofilm properties. *International Journal of Pharmaceutics* **2019,** *569*, 118591.

25.   Chang, S.; Chen, K.; Hua, Q.; Ma, Y.; Huang, W., Evidence for the Growth Mechanisms of Silver Nanocubes and Nanowires. *Journal of Physical Chemistry C* **2011,** *115* (16), 7979-7986.

26.   Xiao, X.; Fan, F.-R. F.; Zhou, J.; Bard, A. J., Current Transients in Single Nanoparticle Collision Events. *JACS* **2008,** *130* (45), 16669-16677.

27.   Bard, A. J.; Zhou, H.; Kwon, S. J., Electrochemistry of Single Nanoparticles via Electrocatalytic Amplification. *Israel Journal of Chemistry* **2010,** *50* (3), 267-276.

28.   Zhou, Y. G.; Rees, N. V.; Compton, R. G., The Electrochemical Detection and Characterization of Silver Nanoparticles in Aqueous Solution. *Angewandte Chemie International Edition* **2011,** *50* (18), 4219-4221.

29.   Ustarroz, J.; Kang, M.; Bullions, E.; Unwin, P., Impact and oxidation of single silver nanoparticles at electrode surfaces: one shot versus multiple events. *Chemical Science* **2017,** *8* (3), 1841-1853.

30.   Katelhon, E.; Tanner, E.; Batchelor-McAuley, C.; Compton, R., Destructive nano-impacts: What information can be extracted from spike shapes? *Electrochimica Acta* **2016,** *199*, 297-304.

31.   Saw, E. N.; Kratz, M.; Tschulik, K., Time-resolved impact electrochemistry for quantitative measurement of single-nanoparticle reaction kinetics | SpringerLink. *Nano Research* **2017,** *10* (11), 3680-3689.

32.   Ngamchuea, K.; Clark, R.; Sokolov, S.; Young, N.; Batchelor-McAuley, C.; Compton, R., Single Oxidative Collision Events of Silver Nanoparticles: Understanding the Rate-Determining Chemistry. *Chemistry-a European Journal* **2017,** *23* (63), 16085-16096.

33.   Ma, W.; Ma, H.; Yang, Z.; Long, Y., Single Ag Nanoparticle Electro-oxidation: Potential-Dependent Current Traces and Potential-Independent Electron Transfer Kinetic. *Journal of Physical Chemistry Letters* **2018,** *9* (6), 1429-1433.

34.   Oja, S.; Robinson, D.; Vitti, N.; Edwards, M.; Liu, Y.; White, H.; Zhang, B., Observation of Multipeak Collision Behavior during the Electro-Oxidation of Single Ag Nanoparticles. *Journal of the American Chemical Society* **2017,** *139* (2), 708-718.

35.   Winkler, J.; Gray, H., Long-Range Electron Tunneling. *Journal of the American Chemical Society* **2014,** *136* (8), 2930-2939.

36.   Robinson, D.; Kondajji, A.; Castaneda, A.; Dasari, R.; Crooks, R.; Stevenson, K., Addressing Colloidal Stability for Unambiguous Electroanalysis of Single Nanoparticle Impacts. *Journal of Physical Chemistry Letters* **2016,** *7* (13), 2512-2517.

37.   Katelhon, E.; Cheng, W.; Batchelor-McAuley, C.; Tschulik, K.; Compton, R. G., Nanoparticle-Impat Experiments are Highly Sensitive to the Presence of Adsorbed Species on Electrode Surfaces. *ChemElectroChem* **2014,** *1* (6), 1057-1062.

38.   Toh, H. S.; Jurkschat, K.; Compton, R. G., The Influence of the Capping Agent on the Oxidation of Silver Nanoparticles: Nano-impacts versus Stripping Voltammetry. *Chemistry - A European Journal* **2015,** *21* (7), 2998-3004.

39.   Sadeghi, R.; Jahani, F., Salting-In and Salting-Out of Water-Soluble Polymers in Aqueous Salt Solutions. *Journal of Physical Chemistry B* **2012,** *116* (17), 5234-5241.
Figures:
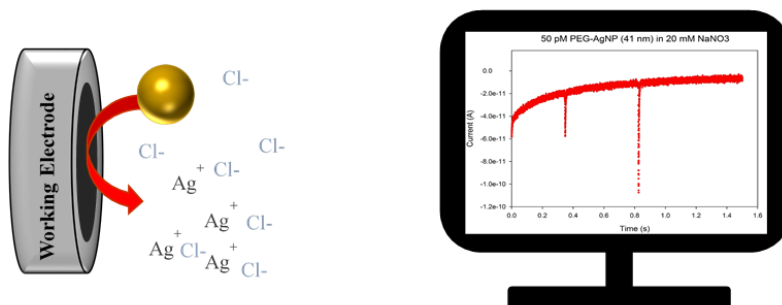
Figure 1: Basic mechanism of individual silver nanoparticle oxidation (right), and the spike-shaped signal produced upon oxidation (left).

Chapter 1: Dependance of PEG-capped silver nanoparticle oxidation frequency on the time between electrode immersion and activation, and the exposure time to KCl

1.1 Abstract

The frequency of single-particle oxidation in particles·s^{-1}, analogous to coulombs·s^{-1}, was compared to the Cottrell model of chronoamperometric oxidation and reduction of a redox species. Previously, a Fickian-like diffusion process for single particle oxidation has been reported, but further exploration is required to fully understand the dynamics of particle-electrode interaction. Initial experiments depicted a linear relationship between the frequency of particle oxidation and time$^{-1/2}$ during the mathematically determined "Cottrell region" of 1.7 seconds, indicating that a Cottrellian relationship could exist. However, when using improved instrumentation the relationship shifted towards a more "steady-state" pattern, indicating that no significant particle concentration gradient is formed at the electrode; at least in the concentration ranges normally employed for single-particle oxidation. Instead, forced time between subsequent chronoamperograms allowed for pre-concentration of particles at the electrode to occur. Furthermore, consecutive chronoamperograms revealed that over longer timescales, the particle oxidation frequency slowly increased. This relationship was attributed to an interaction between the polyethylene glycol capping ligand and the potassium chloride electrolyte instead of an interaction between the particle and the electrode.

1.2 Introduction

The extent to which nano-electrochemistry can be compared with classic electrochemical models was investigated.[1-5] In general, oxidation or reduction of molecules occurs when the potential (or overpotential) is kinetically suitable and the molecule is close enough to the electrode surface, and the signal produced upon oxidation or reduction is predictable.[6] Each

subsequent chronoamperometry (CA) responses at a microdisk electrode for both the non-faradaic double-layer charging current and the faradaic current are nearly identical. The thickness of the electrical double layer is inversely proportional to the electrolyte concentration. Using Gouy-Chapmen theory,[6] the estimated double layer thickness in 20, 50, and 100 mM KCl is 2.15, 1.36, and 0.96 nm, respectively, which is more than ten times smaller than the diameter of the nanoparticles used. The charging current discharges exponentially and is generally discharged in a matter of microseconds when using a microelectrode. The Faradaic current, however, decreases over millisecond or second timescales in the Cottrell region due to the formation of a concentration gradient before reaching steady-state, where it can remain at a stable current for seemingly unlimited time until the redox species is depleted.[7] Single particle oxidation, however, produces CAs which contain particle spikes at irregular frequencies.[8-12] Understanding the frequency at which particles oxidize at the electrode over time provides insight into the aggregation and agglomeration kinetics of particles in suspension.[10, 13-15]

Nanoparticles possess several barriers to oxidation.[1, 13, 15-17] The extent to which they can be compared to the classic models is poorly understood, and the barrier to each particle in the suspension is unique. Particles are often coated with a polymer capping ligand, which results in more stable suspensions. They can be functionalized and tailored for targeted uses such as cancer imaging [18, 19] and treatment.[20] For live biological research, the capping ligand can determine the compatibility and toxicity within the cell, [21, 22] as well as the effectiveness of drug delivery to the cell.[23] In particular, polyethylene glycol (PEG) is a popular capping ligand due to its high solubility in water and non-toxic nature in biological systems.[23, 24] Adding a polymer capping ligand further hinders electron tunneling between the electrode and the particle's core. The estimated capping ligand thickness of the 5 kDa PEG capped AgNS is approximately 10 nm, yet

electron tunneling occurs on angstrom distances.[12] Consequently, consecutive chronoamperograms of a nanoparticle suspension are also each unique, unlike those from a classic redox species. Investigations into the overall pattern of single particle oxidation can reveal how parallel a nanoparticle redox system is to a classic redox system and provide insight into the particle-electrode interface. Additionally, it cannot be assumed that results obtained in one electrolyte will be applicable to a different electrolyte, even when the exact same type of nanoparticle is being investigated.[1, 14, 25-27] Each nanoparticle-electrolyte suspension agglomerates at a unique rate,[27-31] further changing the dynamics of the particle with the electrode over time.

Furthermore, a polymer-gated mechanism of PEG-AgNP oxidation in a room temperature ionic liquid (RTIL) has been reported by the Compton group[32, 33] but detailed investigation of the mechanism of PEG-AgNP oxidation under aqueous conditions has not previously been reported to the best of our knowledge. To ensure the observations are due solely to the particles, flux of the electrolyte species must be considered, especially when the electrolyte doubles as a reactant, to ensure mitigation of limitations due to diffusion and migration.

Although the chosen electrolyte concentrations are ~9-10x larger than the *nanoparticle* concentration, the localized *silver* concentration upon oxidation is much higher. A perfectly spherical 40 nm AgNP contains approximately 2 million atoms of Ag^+. With a diffusion coefficient of ~1.5×10^{-5} $cm^2 \cdot s^{-1}$ [34] and an average time of 1 ms required for oxidation of a silver ion,[35] the approximate concentration of Ag^+ can be calculated using the diffusion length Equation (1.1)[6] to be approximately 0.3 mM. This is 2 orders of magnitude smaller than the electrolyte concentration, thus migration of the electrolyte should not be a limiting factor for oxidation of a single particle.

$$l = \sqrt[2]{2Dt} \qquad\qquad (1.1)$$

Each individual CA from a nanoparticle suspension contains varying numbers of oxidative events and times at which they occur. As a result, experiments containing numerous CAs are required to understand the overall pattern of oxidation. Furthermore, the capping ligand present played a significant role as to when the maximum particle oxidation frequency was achieved.

1.3 Experimental

1.3.1: Materials and Chemicals

Experiments were performed using 0.02 mg·mL^{-1} 40 nm PEG-capped silver nanospheres suspended in water, potassium chloride (99.9% purity), and potassium nitrate (99.9% purity) purchased from Sigma Aldrich. The working electrodes were 2 mm Pt, 10 μm Pt, and 10 μm Au purchased from CH Instruments. The reference electrode was a home-made Ag/AgCl (sat'd KCl) electrode, and a platinum flag was used as the counter electrode. All solutions and suspensions were made using RICCA reagent grade bottled water and all rinsing was performed using Ultrapure filtered water with a resistance of 18.2 MΩ.

1.3.2: Stripping Potential Determination

The 2 mm Pt working electrode was polished and dried prior to use. Linear sweep voltammetry (LSV) was first performed in 20 mM KCl to obtain a background. The electrode was then rinsed, dried, and 2 μL PEG-AgNP were drop-cast onto the surface. The cast was allowed to dry under a slow nitrogen flow. Once dry, LSV was performed from 0 V to 0.8 V vs. Ag/AgCl (sat'd KCl) at a scan rate of 50 mV·s^{-1}.

1.3.3: Instrumentation Parameters

For single particle experiments, three different potentiostats were used; a CHI 650A (CHInstruments, San Antonio, TX), a PalmSens4 (BASi, West Lafayette IN), and an NPI VA-

10X (NPI Electronics, Tamm, Germany. For single particle experiments, three different

potentiostats were used; a CHI 650A, a PalmSens4, and an NPI VA-10X. Table 1.1 summarizes

the data collection settings utilized for each potentiostat.

Initial experiments were performed using a CHI 650 A potentiostat at a sampling interval

of 0.2 ms. The CHI 650 A is only capable of collecting at this sampling rate for three seconds

due to limited internal storage and the inability to transfer data in real-time. Instead, data is

stored first internally then transferred to the computer upon experiment completion, which takes

approximately 15 seconds. During this time, the cell is at open circuit potential and undisturbed.

Using repetitive runs, the next experiment began automatically upon data transfer completion.

Thus, collection of 60 s of data at three-second intervals actually occurs over ~320 s.

The experiments were repeated using a PalmSens4 and an NPI VA-10x. The PalmSens4

sampling rate was half that of the CHI but performed chronoamperometry for 10 s and needed

only ~5 s for data transfer upon experiment completion, improving the collection of 60 seconds

of data to occur over ~110 s. The NPI VA-10x transferred the data in real-time, thus allowing for

more in-depth analysis of the relationship between particle, electrolyte, and electrode. For each

instrument, at least 20 consecutive CAs were performed at 450 mV and 650 mV, and the times at

which oxidation began was charted and compared.

1.4 Results and Discussion

1.4.1: Investigating oxidation frequency over individual chronoamperograms

The LSV contained a stripping peak at 150 mV (Figure 1.1), indicating oxidation of the

drop-cast silver. To promote oxidation upon single particle interaction, 450 mV and 650 mV

were chosen as the experimental potentials. KCl was chosen because it has been previously

reported to allow for complete oxidation of C-AgNPs [26, 36] During the initial experiments, 40 nm

PEG-AgNPs in 20 mM KCl were oxidized using the CHI 650 A and a 10 µm platinum working electrode, it was noted that most anodic spikes occurred during the first second of the three-second CA, leading to the suspicion of a Cottrell-like behavior. Figure 1.2 combines the time at which oxidation began for each particle during 200 three-second chronoamperometric measurements. Approximately 60% of the particles were oxidized during the first second of each three-second CA, and the remaining ~40% occurred during the last 2/3 of the CAs. These initial experiments suggested that a Fickian-like model was indeed occurring as previously reported.[37] The oxidation frequency vs $t^{-1/2}$ was plotted to further investigate the applicability of the Cottrell equation to destructive oxidative analysis of silver nanoparticles (Figure 1.3, left). The Cottrell Equation (1.2) was modified to account for the frequency of single particle oxidation (Equation 1.3) where $C^{\ddagger}$ represents particles per cm^3 instead of moles per cm^3, represented by C^* in the original Cottrell equation.

$$i(t) = \frac{nFAD^{1/2}C^*}{\pi^{1/2}t^{1/2}} \qquad (1.2)$$

$$f_{SPO} = \frac{AD^{1/2}C^{\ddagger}}{\pi^{1/2}t^{1/2}} \qquad (1.3)$$

The diffusion coefficient of the 40 nm AgNSs estimated by the Stokes-Einstein equation was 8×10^{-8} $cm^2 \cdot s^{-1}$. Because data from multiple CAs was combined, the slope was divided by the total number of CAs performed to provide a normalized average of the diffusion coefficient for the total data set. Analysis of the slope of Figure 1.3 (a) resulted in a diffusion coefficient of 2×10^{-6} $cm^2 \cdot s^{-1}$, a 2,400% error.

The experiments repeated using a PalmSens4 and 10 µm diameter gold working electrode are plotted in Figure1.4 (right), and the anticipated slope is indicated by the dashed line. Analysis resulted in a diffusion coefficient of 4×10^{-7} $cm^2 \cdot s^{-1}$, a slightly improved percent error of 400%.

Although several groups of experiments performed with both instruments showed a Cottrellian-like relationship, the large diffusion coefficients, coupled with the statistically different results from the two instruments, indicated that an unaccounted variable remained. The primary difference between the two instruments was the amount of time between each CA. The PalmSens4 began the subsequent CA experiments approximately 3x faster than the CHI, and the estimated diffusion coefficient was 5 times smaller. This indicates that particles could be sticking to the electrode surface during the data transfer time, which would cause $C^{\ddagger}$ at the electrode surface to be larger than the assumed $C^{\ddagger}$ of the bulk solution. Furthermore, the sampling interval of the PalmSens4 per CA was half that of the CHI 650A, which could contribute to the scaling discrepancy of 3:5.

Oxidation of PEG-AgNPs in 2 mM, 50 mM, and 100 mM KCl was also performed using the PalmSens4 to investigate the effect of electrolyte concentration on Cottrell-like relationship, and to investigate the possibility of counter-ion limitation. Figure 1.4 depicts 10 consecutive CAs at each electrolyte concentration under otherwise identical experimental conditions. Using 2 mM KCl, no oxidative events were observed, though 2M is an order of magnitude larger than the estimated localized Ag^{+} concentration. Using 50 mM KCl, the apparent Cottrellian relationship was present, as with the 20 mM KCl. However, the relationship was non-existent when 100 mM KCl was used. There were also more oxidative events in the 100 mM KCl, indicating that oxidation can occur more easily in the higher electrolyte concentrations.

To overcome temporal resolution limitations, subsequent experiments in 20 mM KCl were performed using an NPI VA-10x voltage amplifier coupled to the NanoDAQ2, an analog-to-digital converter and potentiostat built at Ruhr Universität Bochum by Kannasoot Kanokkanchana in the lab of Dr. Professor Kristina Tschulik. This instrumentation allowed for a

more accurate depiction of the real-time behavior of particles in a suspension. For these experiments, citrate capped particles were first used to eliminate the additional oxidation barrier incurred from a polymer capping ligand, and then PVP capped particles were employed to observe if particles of both capping ligands followed similar trends. PEG-capped particles were unfortunately unavailable at the time these experiments were performed. At time t = 0 of the first chronoamperogram, the concentration of both the particles and electrolyte at the electrode surface (x = 0) is the same as that of the bulk suspension. To let C_0 of the electrolyte to equilibrate with C_{bulk}, there was a 2 second pause between each CA.

The NPI VA-10x is incapable of holding an open circuit, which was automatically maintained by the previously discussed potentiostats, during the data transfer time. Instead, the potential automatically switched to 110 mV after the programmed chronoamperometric measurement was complete. 110 mV was chosen because a cyclic voltammogram (CV) of particles which have been drop-cast onto a macrodisk electrode indicates that no oxidation or reduction occurs at this potential for all used electrolytes. At this time, it is unclear if the presence of an applied potential during the instrument quiet time could prevent the adsorption of particles (citrate or polymer capped) to the electrode.

Experiments using the NPI reveal a different pattern of oxidation from the experiments that performed using the CHI 650A and PalmSens4, as shown in Figure 1.5. The oxidative spikes occurred in a more steady-state pattern throughout the entire CA, as opposed the previously observed larger number of spikes at the beginning of the CA. This confirms the suspicion that some particles adsorbed to the electrode surface between subsequent chronoamperograms of earlier experiments, and that the initially observed pattern of oxidation was misleading. Instead, the primary contributors to oxidation patterns are electrode fouling and particle agglomeration,

and a Cottrellian-like relationship does not exist for pM concentrations of particles in mM concentrations of electrolyte when temporal resolution is sufficient. It is hypothesized that the observed Cottrellian-like relationship was due to a "preconcentration" of the particles at the electrode during the data transfer time. This opens the opportunity for a concentration gradient, which then allows for oxidation to occur with a $t^{-1/2}$ relationship. Since the concentration gradient is not formed solely due to the particles' diffusion coefficients, the Cottrell model is invalid for the analysis of this dependency, as evidenced by the large slopes observed in Figure 1.3.

1.4.1: Investigating the oxidation frequency over longer time-scales

Initial experiments in 20 mM KCl revealed that the second series of experiments performed at 450 mV contained significantly more spikes than the first (Figure 1.6). For this to occur, it was hypothesized that either the particles were losing their capping ligands by "walking" on the electrode surface and surrounding insulator, thus making oxidation easier, or there was an interaction between the PEG and KCl that allowed for electron tunneling through the capping ligand once a sufficient amount of electrolyte was incorporated into the PEG, which requires a "soaking time". To test this hypothesis, experiments were designed to probe the "soaking time" hypothesis. One suspension of 20 mM KCl and 30 pM PEG AgNP was tested immediately upon creation, and another suspension was allowed to equilibrate for five minutes before the insertion of the electrodes.

Figure 1.7 depicts a histogram of the time at which oxidation began (bin = 0.1 s) for the first 10 CAs performed at 450 mV without (top) and with (bottom) the pre-treatment in KCl. Without the five-minute pretreatment, only two particles were electrooxidized over the first 10 ten-second CAs. In contrast, there were nearly 100 particle oxidative events during the first 10 CAs after the five-minute pretreatment, indicating that there was an interaction between the PEG

and KCl which allows for the electron tunneling between the electrode and the particle surface. The polymer-gated mechanism of PEG-AgNP oxidation described by Compton et. Al[32, 33] was based on an increased oxidation frequency with increased exposure to the electrode. However, these experiments revealed a higher oxidation frequency with subjection to electrolyte instead of exposure to the electrode surface, indicating that an interaction between the electrolyte and capping ligand occurs instead of polymer-gating. For oxidation of a particle to occur, electrons must travel from the particle to the electrode surface. Electron tunneling generally occurs over distances on the order of 10 Å, shorter than the ~6 nm length of 5 kDa PEG.[12, 38, 39]

At present, the hypothesis is the addition of electrolyte into the PEG lowers the band-gap enough so that PEG allows long-range electron tunneling at 450 and 650 mV.[40-42] Long range electron tunneling occurs when band-gaps are close enough together to allow the electron hopping to occur.[41] Band-gaps of PEG have been shown to decrease in the presence of electrolyte,[43-45] and can be attributed to the presence K^+.[45] The solubility of PEG mixed with salts in methanol,[43, 45] aqueous,[46-48] biologic,[23, 49] and ionic solid electrolytes[4, 50] have been studied in relation to a variety of applications. These results were consistent across multiple experiments performed in 20 mM and 50 mM KCl. When the KCl concentration was increased to 100 mM, however, oxidation began immediately upon creation of the suspension. The results were also consistent between a 10 µm platinum working electrode and a 10 µm gold working electrode, further confirming that interaction with the electrode was not the limiting step in the oxidation of PEG-capped AgNP in 20 or 50 mM KCl. The findings of these studies can help explain the specific chemistry occurring during the oxidation of PEG-AgNP.

Furthermore, analysis of the charge passed during each current spike indicates that at 450 mV and 650 mV, complete oxidation occurred, with an average size of 32 nm being calculated at

both 450 mV and 650 mV for the TEM-calculated 42 nm PEG-AgNP (Table 1.2). The possibility of incomplete oxidation or multi-step oxidation must be considered in each system, [13, 51, 52] and the charge passed during each current spike is a valuable indication of the interaction between the electrode and particle during oxidation. Citrate-capped AgNPs in halide electrolytes generally fully oxidize in one current spike,[26, 35, 36] and the presence of PEG did not alter that relationship.

In 100 mM KCl, oxidation began during the first 10 CAs at 450 mV, but the oxidation frequency increased over the full 40 CAs. The average oxidation frequency in 20 mM KCl without "soaking time" was 0.24 ± 0.23 particles·s^{-1}, whereas the average oxidation frequency in 100 mM KCl was 1.11 ± 0.66 particles·s^{-1}. Based on the Stokes-Einstein calculated diffusion coefficients and the particle concentrations, 2.8 particles·s^{-1} was expected. Furthermore, the total number of particles oxidized during each group of 10 CAs is summarized in Table 1.3. Over the course of the first 40 CAs, the total number of particles oxidized increased regardless of the potential, indicating that even at 100 mM an integration of the electrolyte into the capping ligand which increases oxidation frequency occurs.

1.5 Conclusion

Instrument limitations can provide misleading information and must be considered during the analysis. PEG-capped AgNPs in 20 mM and 50 mM KCl adsorb to the electrode or surrounding insulator of Au and Pt microdisk electrodes, forming a concentration gradient that gives the appearance of a $t^{-1/2}$ dependence of oxidation frequency from CA to CA when given the opportunity. Without this opportunity, particle concentrations on the order of pM do not form a significant concentration gradient and the oxidation frequency remains, on average, unchanged throughout the CA. Furthermore, the presence of even 20 mM KCl is sufficient to prevent

oxidation barriers that would occur due to unavailability of chloride. The 20 mM KCl interacts

with the PEG capping ligand, leading to an increase in oxidation frequency over longer time

scales.

References

1. Cheng, W.; Compton, R., Electrochemical detection of nanoparticles by 'nano-impact' methods. *Trends in Analytical Chemistry* **2014,** *58*, 79–89.

2. Pererio, M.; Baldomir, D., Structure of small silver clusters and static response to an external electric field. *PHYSICAL REVIEW A* **2007,** *75*, 033202 1-10.

3. Bansal, V.; Li, V.; O'Mullane, A. P.; Bhargava, S. K., Shape dependent electrocatalytic behaviour of silver nanoparticles. *CrystEngComm* **2010,** *12*, 4280-4286.

4. Chaudhary, V.; Thakur, A.; Bhowmick, A., Improved optical and electrical response in metal-polymer nanocomposites for photovoltaic applications. *Journal of Materials Science* **2011,** *46* (18), 6096-6105.

5. Zhou, Y. G.; Rees, N. V.; Compton, R. G., The Electrochemical Detection and Characterization of Silver Nanoparticles in Aqueous Solution. *Angewandte Chemie International Edition* **2011,** *50* (18), 4219-4221.

6. Bard, A. J.; Faulkner, L. R., *Electrochemical Methods: Fundamentals and Applications, 2nd Edition*. 2 ed.; John Wiley & Sons: 2000; p 864.

7. Fick, A., On Liquid Diffusion (Reprinted from the London, Edinburgh, and Dublin Philosophical Magazine and Journal of Science, Vol 10, Pg 30, 1855). *J Membrane Sci* **1995,** *100* (1), 33-38.

8. Boika, A.; Bard, A. J., Time of First Arrival in Electrochemical Collision Experiments as a Measure of Ultralow Concentrations of Analytes in Solution. *Analytical Chemistry* **2015,** *87* (8), 4341-4346.

9. McFarland, A. D.; Van Duyne, R. P., Single Silver Nanoparticles as Real-Time Optical Sensors with Zeptomole Sensitivity. *Nano Lett.* **2003,** *3* (8), 1057-1062.

10. Xiao, X.; Fan, F.-R. F.; Zhou, J.; Bard, A. J., Current Transients in Single Nanoparticle Collision Events. *JACS* **2008,** *130* (45), 16669-16677.

11. Bard, A. J.; Zhou, H.; Kwon, S. J., Electrochemistry of Single Nanoparticles via Electrocatalytic Amplification. *Israel Journal of Chemistry* **2010,** *50* (3), 267-276.

12. Kim, J.; Kim, B.; Cho, S.; Bard, A., Tunneling Ultramicroelectrode: Nanoelectrodes and Nanoparticle Collisions. *Journal of the American Chemical Society* **2014,** *136* (23), 8173-8176.

13. Ustarroz, J.; Kang, M.; Bullions, E.; Unwin, P., Impact and oxidation of single silver nanoparticles at electrode surfaces: one shot versus multiple events. *Chemical Science* **2017,** *8* (3), 1841-1853.

14. Krause, K. J.; Brings, F.; Schnitker, J.; Kätelhön, E.; Rinklin, P.; Compton, R. G.; Lemay, S. G.; Wolfrum, B., The Influence of Supporting Ions on the Electrochemical Detection

of Individual Silver Nanoparticles: Understanding the Shape and Frequency of Current Transients in Nano-impacts. *Chemistry - A European Journal* **2017,** *23* (19), 4638-4643.

15.   Chen, C.-H.; Ravenhill, E. R.; Momotenko, D.; Kim, Y.-R.; Lai, S. C. S.; Unwin, P. R., Impact of Surface Chemistry on Nanoparticle–Electrode Interactions in the Electrochemical Detection of Nanoparticle Collisions. *Langmuir* **2015,** *31*, 11932-11942.

16.   Toh, H. S.; Jurkschat, K.; Compton, R. G., The Influence of the Capping Agent on the Oxidation of Silver Nanoparticles: Nano-impacts versus Stripping Voltammetry. *Chemistry - A European Journal* **2015,** *21* (7), 2998-3004.

17.   Katelhon, E.; Cheng, W.; Batchelor-McAuley, C.; Tschulik, K.; Compton, R. G., Nanoparticle-Impat Experiments are Highly Sensitive to the Presence of Adsorbed Species on Electrode Surfaces. *ChemElectroChem* **2014,** *1* (6), 1057-1062.

18.   Xiaohua Huang; Ivan H. El-Sayed; Wei Qian, a.; Mostafa A. El-Sayed*, Cancer Cell Imaging and Photothermal Therapy in the Near-Infrared Region by Using Gold Nanorods. *Journal of the American Chemical Society* **2006,** *128* (6), 2115-2120.

19.   Wang, K.; Shangguan, L.; Liu, Y.; Jiang, L.; Zhang, F.; Wei, Y.; Zhang, Y.; Qi, Z.; Wang, K.; Liu, S., In Situ Detection and Imaging of Telomerase Activity in Cancer Cell Lines via Disassembly of Plasmonic Core–Satellites Nanostructured Probe. *Analytical Chemistry* **2017,** *89* (13).

20.   Guardia, P.; Corato, R. D.; Lartigue, L.; Wilhelm, C.; Espinosa, A.; Garcia-Hernandez, M.; Gazeau, F.; Manna, L.; Pellegrino, T., Water-Soluble Iron Oxide Nanocubes with High Values of Specific Absorption Rate for Cancer Cell Hyperthermia Treatment. *ACSNano* **2012,** *6* (4), 3080-3091.

21.   Loza, K.; Diendorf, J.; Sengstock, C.; Ruiz-Gonzalez, L.; Gonzalez-Calbet, J.; Vallet-Regi, M.; Koller, M.; Epple, M., The dissolution and biological effects of silver nanoparticles in biological media. *Journal of Materials Chemistry B* **2014,** *2* (12), 1634-1643.

22.   Zhang, F.; Durham, P.; Sayes, C. M.; Lau, B. L. T.; Bruce, E. D., Particle uptake efficiency is significantly affected by type of capping agent and cell line. *Journal of Applied Toxicology* **2015,** *35*, 1114-1121.

23.   Kumar, S.; Alnasif, N.; Fleige, E.; Kurniasih, I.; Kral, V.; Haase, A.; Luch, A.; Weindl, G.; Haag, R.; Schafer-Korting, M.; Hedtrich, S., Impact of structural differences in hyperbranched polyglycerol-polyethylene glycol nanoparticles on dermal drug delivery and biocompatibility. *Eur J Pharm Biopharm* **2014,** *88* (3), 625-34.

24.   Hajtuch, J.; Hante, N.; Tomczyk, E.; Wojcik, M.; Radomski, M.; Santos-Martinez, M.; Inkielewicz-Stepniak, I., Effects of functionalized silver nanoparticles on aggregation of human blood platelets. *International Journal of Nanomedicine* **2019,** *14*, 7399-7417.

25.   Plowman, B.; Tschulik, K.; Walport, E.; Young, N.; Compton, R., The fate of nano-silver in aqueous media. *Nanoscale* **2015,** *7* (29), 12361-12364.

26.   Saw, E. N.; Kratz, M.; Tschulik, K., Time-resolved impact electrochemistry for quantitative measurement of single-nanoparticle reaction kinetics | SpringerLink. *Nano Research* **2017,** *10* (11), 3680-3689.

27.   Ngamchuea, K.; Clark, R.; Sokolov, S.; Young, N.; Batchelor-McAuley, C.; Compton, R., Single Oxidative Collision Events of Silver Nanoparticles: Understanding the Rate-Determining Chemistry. *Chemistry-a European Journal* **2017,** *23* (63), 16085-16096.

28.   Sokolov, S. V.; Tschulik, K.; Batchelor-McAuley, C.; Jurkschat, K.; Comptin, R. G., Reversible or Not? Distinguishing Agglomeration and Aggregation. *Analytical Chemistry* **2015,** (87), 10033-10039.

29.   Dirkse, T. P.; Wiers, B., The Stability and Solubility of AgO in Alkaline Solutions. *Journal of the Electrochemical Society* **1959,** *106* (4), 284-287.

30.   Robinson, D.; Kondajji, A.; Castaneda, A.; Dasari, R.; Crooks, R.; Stevenson, K., Addressing Colloidal Stability for Unambiguous Electroanalysis of Single Nanoparticle Impacts. *Journal of Physical Chemistry Letters* **2016,** *7* (13), 2512-2517.

31.   Jimenez-Lamana, J.; Slaveykova, V., Silver nanoparticle behaviour in lake water depends on their surface coating. *Science of the Total Environment* **2016,** *573*, 946-953.

32.   Tanner, E.; Tschulik, K.; Tahany, R.; Jurkschat, K.; Batchelor-McAuley, C.; Compton, R., Nanoparticle Capping Agent Dynamics and Electron Transfer: Polymer-Gated Oxidation of Silver Nanoparticles. *Journal of Physical Chemistry C* **2015,** *119* (32), 18808-18815.

33.   Tanner, E.; Batchelor-McAuley, C.; Compton, R., Nanoparticle Capping Agent Controlled Electron-Transfer Dynamics in Ionic Liquids. *Chemistry-a European Journal* **2016,** *22* (17), 5976-5981.

34.   Johnston, R.; Spiro, M., Diffusion Coefficients of Ag+ and Ag(SO3)23- by Rotating Disk Method. *Journal of Physical Chemistry* **1967,** *71* (12), 3784-3791.

35.   Saw, E.; Blanc, N.; Kanokkanchana, K.; Tschulik, K., Time-resolved impact electrochemistry - A new method to determine diffusion coefficients of ions in solution. *Electrochimica Acta* **2018,** *282*, 317-323.

36.   Ngamchuea, K.; Clark, R. O. D.; Sokolov, S. V.; Batchelor-McAuley, C.; Compton, R. G., Single Oxidative Collision Events of Silver Nanoparticles: Understanding the Rate-Determining Chemistry. *Chemistry - A European Journal* **2017,** *23* (63), 16085-16096.

37.   Stuart, E. J. E.; Zhou, Y.-G.; Rees, N. V.; Compton, R. G., Particle-impact nanoelectrochemistry: a Fickian model for nanoparticle transport. *RCS Advances* **2012,** *2*, 12701-12705.

38.   Scanlon, M.; Peljo, P.; Mendez, M.; Smirnov, E.; Girault, H., Charging and discharging at the nanoscale: Fermi level equilibration of metallic nanoparticles. *Chemical Science* **2015,** *6* (5), 2705-2720.

39.   Peljo, P.; Manzanares, J.; Girault, H., Variation of the Fermi level and the electrostatic force of a metallic nanoparticle upon colliding with an electrode. *Chemical Science* **2017,** *8* (7), 4795-4803.

40.   Zhao, J.; Bradbury, C.; Fermin, D., Long-range electronic communication between metal nanoparticles and electrode surfaces separated by polyelectrolyte multilayer films. *Journal of Physical Chemistry C* **2008,** *112* (17), 6832-6841.

41.   Winkler, J.; Gray, H., Long-Range Electron Tunneling. *Journal of the American Chemical Society* **2014,** *136* (8), 2930-2939.

42.   Michaeli, K.; Beratan, D.; Waldeck, D.; Naaman, R., Voltage-induced long-range coherent electron transfer through organic molecules. *Proceedings of the National Academy of Sciences of the United States of America* **2019,** *116* (13), 5931-5936.

43.   Hakem, I.; Lal, J.; Bockstaller, M., Binding of monovalent ions to PEO in solution: Relevant parameters and structural transitions. *Macromolecules* **2004,** *37* (22), 8431-8440.

44.   Wildgoose, G. G.; E., C.; Compton, R. G., Metal Nanoparticles and Related Materials Supported on Carbon Nanotubes: Methods and Applications. *Small* **2005,** *2* (2), 182-193.

45.   Lundberg, R. D.; Bailey, F. E.; Callard, R. W., Interactions of Inorganic Salts with Poly(ethylene oxide). *Journal of Polymer Science Part a-1-Polymer Chemistry* **1966,** *4* (6PA1), 1563-&.

46.   Poudel, L.; Podgornik, R.; Ching, W., The Hydration Effect and Selectivity of Alkali Metal Ions on Poly(ethylene glycol) Models in Cyclic and Linear Topology. *Journal of Physical Chemistry a* **2017,** *121* (24), 4721-4731.

47.   Dan, A.; Ghosh, S.; Moulik, S., The solution behavior of poly(vinylpyrrolidone): Its clouding in salt solution, solvation by water and isopropanol, and interaction with sodium dodecyl sulfate. *Journal of Physical Chemistry B* **2008,** *112* (12), 3617-3624.

48.   Sadeghi, R.; Jahani, F., Salting-In and Salting-Out of Water-Soluble Polymers in Aqueous Salt Solutions. *Journal of Physical Chemistry B* **2012,** *116* (17), 5234-5241.

49.   Magarkar, A.; Karakas, E.; Stepniewski, M.; Rog, T.; Bunker, A., Molecular Dynamics Simulation of PEGylated Bilayer Interacting with Salt Ions: A Model of the Liposome Surface in the Bloodstream. *Journal of Physical Chemistry B* **2012,** *116* (14), 4212-4219.

50.   Taboada, M.; Galleguillos, H.; Graber, T., Compositions, densities, conductivities, and refractive indices of potassium chloride or/and sodium chloride plus PEG 4000 plus water at 298.15 and liquid-liquid equilibrium of potassium chloride or sodium chloride plus PEG 4000 plus water at 333.15 K. *Journal of Chemical and Engineering Data* **2005,** *50* (1), 264-269.

51.   Sun, L.; Wang, W.; Chen, H.-Y., Dynamic Nanoparticle-Substrate Contacts Regulate Multi-Peak Behavior of Single Silver Nanoparticle Collisions. *ChemElectroChem Communications* **2018,** (5), 2995-2999.

52.   Oja, S.; Robinson, D.; Vitti, N.; Edwards, M.; Liu, Y.; White, H.; Zhang, B., Observation of Multipeak Collision Behavior during the Electro-Oxidation of Single Ag Nanoparticles. *Journal of the American Chemical Society* **2017,** *139* (2), 708-718.

Tables

Table 1.1: Data collection settings for the three potentiostats

Potentiostat	Sampling Interval (s)	Data Collection Time (s)	Data Transfer Time (s)
CHI 650 A	0.0002	3	~15
PalmSens4	0.0004	10	~5-7
NPI VA-10x	0.000033	10	Real-time

Table 1.2: Electrochemically calculated size and total particles oxidized of 40 nm PEG-AgNP in 20 mM electrolyte

	650 mV		750 mV	
Electrolyte	Diameter	N	Diameter	N
KCl	31 ± 13.8 nm	315	32 ± 14.6 nm	329
KNO$_3$	29 ± 3.9 nm	34	32 ± 11.1 nm	27

Table 1.3: Number of particles oxidized in 100 mM KCl during consecutive 10-second CAs

CA number	N	Frequency (particles·s^{-1})
1-10 (450 mV)	57	0.57
11-20 (650 mV)	60	0.60
21-30 (450 mV)	158	1.58
31-40 (650 mV)	162	1.62

Figures
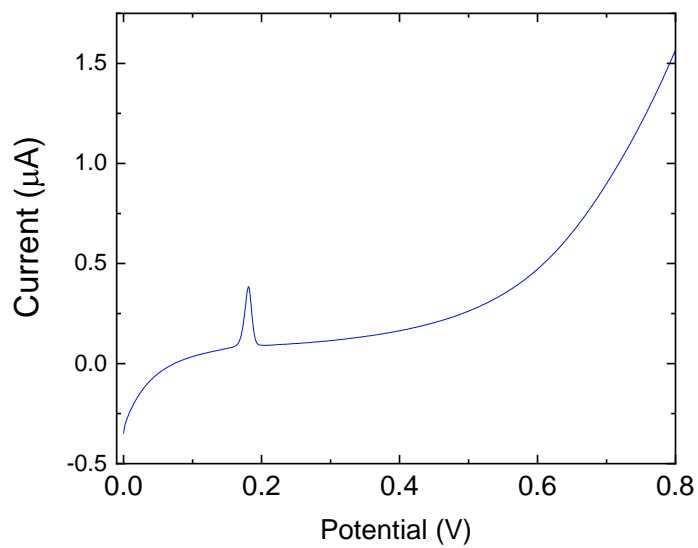
Figure 1.1: Linear sweep of drop-cast 40 nm PEG-AgNP in KCl at 0.5 V·s⁻¹, beginning at 0 V and ending at 0.8 V vs Ag/AgCl (sat'd KCl). The working electrode was a 2mM Pt disk.
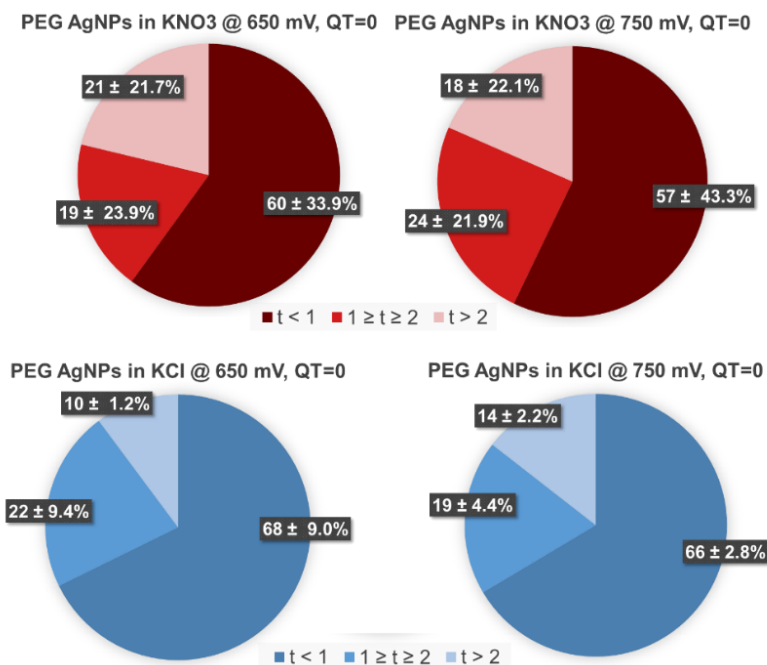
Figure 1.2: The time at the beginning of oxidation of PEG capped AgNPs in 20 mM electrolyte. For each pie chart, an entire experiment of 50 CAs was combined into a single chart. All potentials are vs Ag/AgCl (sat'd KCl)
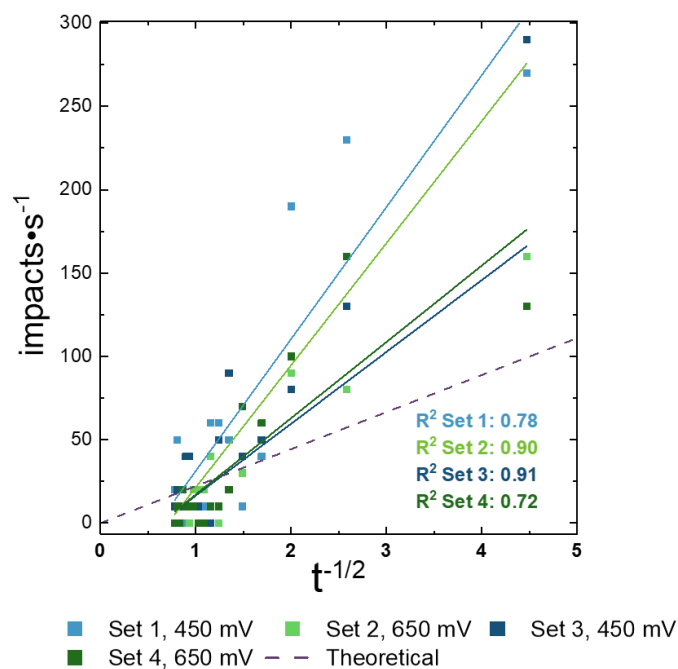
Figure 1.3: Particles per second vs. time at particle oxidation of 30 pM PEG capped AgNP in 20 mM KCl at 450 mV and 650 mV vs Ag/AgCl (sat'd KCl). The dashed line indicates the theoretical plot for a 30 pM suspension of 40 nm AgNP at a diameter = 10 μm electrode.
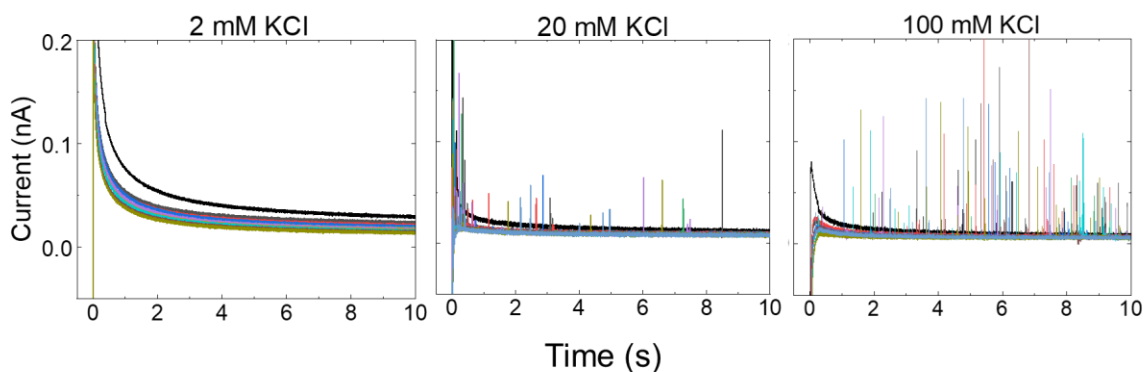
Figure 1.4: 30 pM PEG-AgNP at 450 mV vs Ag/AgCl (sat'd KCl) at varying KCl concentrations. Ten consecutive CAs are overlaid for each plot.
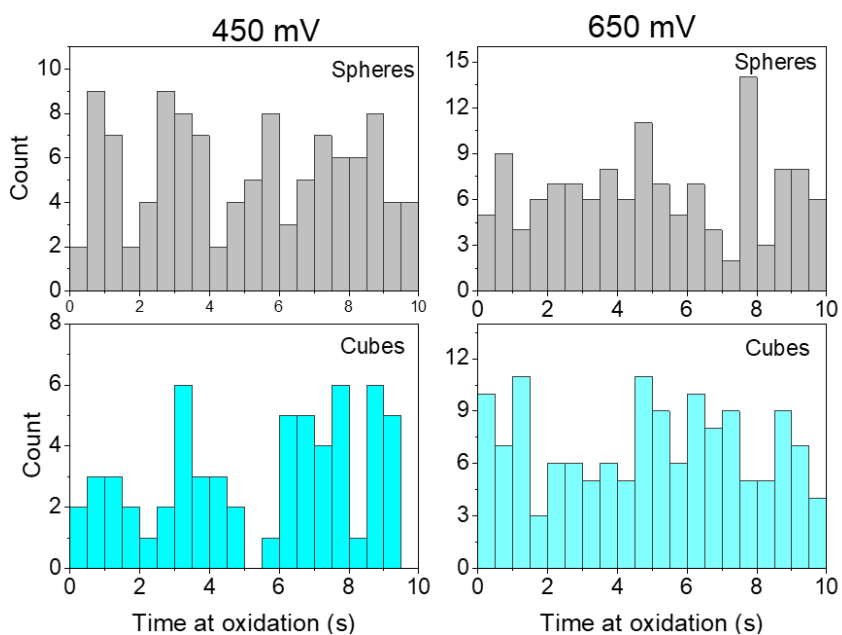
Figure 1.5: Time at which oxidation of PVP capped particles began in 41 mM KOH, using the NPI VA-10x. Potentials are vs. Ag/AgCl (sat'd KCl).
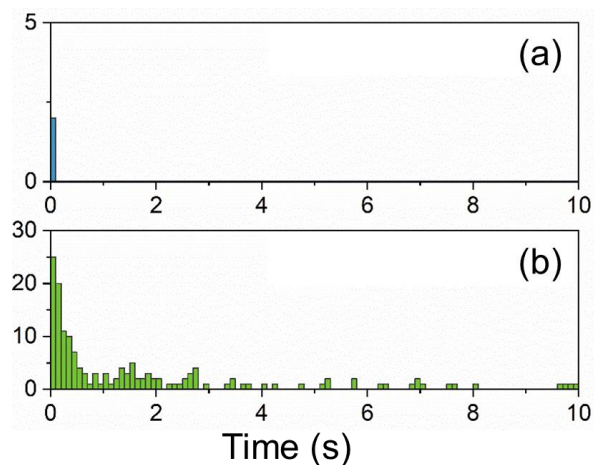
Figure 1.6: Oxidative events during chronoamperograms 1-10 (top) and 31-40 (bottom) of a suspension of 40 nm PEG-AgNP in 20 mM KCl. The potential used for plot (a) was 450 mV vs. Ag/AgCl (sat'd KCl), and the potential for plot (b) was 650 mV vs Ag/AgCl (sat'd KCl)
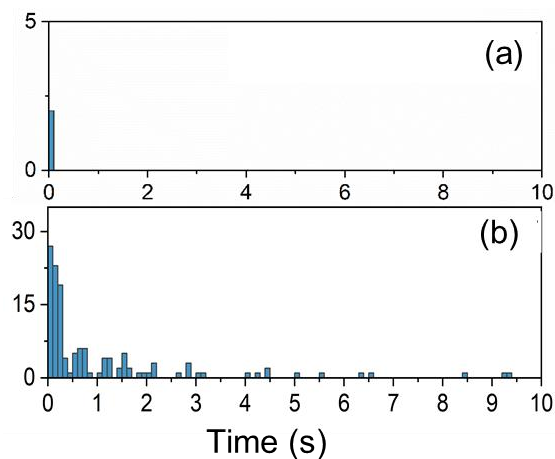
Figure 1.7: PEG capped AgNP in 20 mM KCl at 450 mV vs Ag/AgCl (sat'd KCl) immediately upon mixture with the KCl (a) and after letting the suspension equilibrate for five minutes (b).

Chapter 2: The Salting-In Effect and Silver Particle Oxidation

2.1: Abstract

This work explores the connection between salting-in, salting-out, and the oxidation of polymer capped silver nanoparticles in a suspension upon contact with an electrode. Investigating single particle oxidation is often attached with a trial-and-error approach, requiring large amounts of time and money before progress is achieved. Polymer capping ligands can prevent electron tunneling between the electrode and particle, and methodically improving the probability of oxidation is necessary for timely investigation into the mechanism of single particle oxidation. The salting-in and salting-out effect of polyethylene glycol and poly-vinylpyrrolidone has been previously investigated for biological research, and salting-in electrolytes were investigated to determine if they would improve the particle connection to the electrode, promoting oxidation. Lithium perchlorate, potassium chloride, and calcium chloride were mixed with poly-vinylpyrrolidone capped silver nanoparticles and drop-cast onto an electrode, then linear sweep voltammetry was used to determine if salting-in would promote oxidation. Although these electrolytes have been shown to salt-in to poly-vinylpyrrolidone, they did not promote oxidation of the PVP capped AgNP.

2.2: Introduction

Poly-vinylpyrrolidone (PVP) and other polymers commonly used for capping and stabilizing nanoparticles are often used specifically for insulating the particle from its surrounding environment.[1-4] While protecting the particle from aggregating or agglomerating, PVP also inhibits particle oxidation due to the insulating properties.[5-7] PVP capped particles have been notoriously difficult to oxidize,[8] but is required for the synthesis of several shapes including cubes and wires.[1] Experimentation on PEG and PVP particles revealed that in KCl, the area

produced by drop-cast 5kDa PEG capped particles was almost double the area produced by 45 kDa PVP capped particles. It has been reported that KCl salts in to PEG, but salts out of PVP.[7, 9]The larger stripping peak from the PEG-capped AgNP and ability to obtain oxidative single-particle events after some equilibration time (discussed further in Chapter 1) were involved in the formation of the hypothesis connecting salting-in and particle oxidation Herein, salting-in properties were explored as an avenue to overcome the poor electrode contact induced by polymers.

Salts can either increase (salting-in) or decrease (salting-out) the solubility of proteins or polymers in solvents. Frank Hofmeister determined that anions have a larger effect on protein solubility than cations, and developed the Hofmeister Series which orders cations and anions in the order of greatest to least promotion of protein solubility in water.[10] When salting-in occurs, it is hypothesized that an ionic interaction occurs between the ion(s) and localized dipoles or lone pairs of electrons in the polymer. PVP has been previously investigated to understand its salting-in and out behaviors, and how they compare to proteins.[5, 9]

The interaction of PVP with ions was first investigated using aromatic ions[6, 11, 12] and later expanded to inorganic salts with salting-in and salting-out studies.[7, 9] When salting-in occurs, conductivity generally increases.[13] Additionally, studies on long-range electron tunneling have revealed that incorporation of salts into polymers can lower their band-gaps,[14, 15] increasing the likelihood of electron tunneling through the ligand. While KCl promotes salting-out of PVP, LiCl and $CaCl_2$ were not found to do so.[9] Additionally, perchlorates are not found to induce salting-out of polymers.[16] Using salting-in electrolytes (LiCl and $CaCl_2$) and comparing with a salting out electrolyte (KCl), the effect of salting-in on single particle oxidation of polymer-capped nanoparticles was explored. Chloride-containing electrolytes were chosen due to relative

ease of oxidizing silver nanospheres (AgNS) in halides[17-19] to minimize the barriers to oxidation.

2.3: Experimental

2.3.1: Chemicals and materials

The 40 nm PVP, citrate, and polyethylene glycol (PEG) capped AgNS were purchased from

Nanocomposix (San Diego, CA). The LiCl, $CaCl_2 \cdot 2H_2O$ (98%), and KCl (99%) were purchased

from Sigma Aldrich (St. Louis, MO). The 2 mm Pt working electrode was purchased from CH

Instruments (Austin, Tx). Polycrystalline diamond suspension polish of 1 μm, 0.05 μm non-

crystallizing alumina polish, nylon PSA polishing cloths, and MasterText2 polishing cloths were

purchased from Buehler (Lake Bluff, IL). The potentiostat used was a PalmSens4, purchased

through BASinc.

2.3.2 Methods

Prior to all experiments, the 2 mm Pt electrode was polished per BASi protocol[20] in 1 μm

polycrystalline diamond suspension polish, followed by 0.05 μm non-crystallizing alumina

polish. To ensure proper electrode function, the electrodes were characterized in 1 mM

$K_3Fe(CN)_6$ via cyclic voltammetry each day that experiments were performed. Next, blank

chronoamperograms were obtained in the aqueous electrolyte of interest, sans nanoparticles.

Afterwards, AgNS were mixed to produce a suspension of 50 pM AgNP in 50 mM electrolyte,

mixed, and immediately drop-cast onto the electrode. The electrode was dried under a nitrogen

flow in a dark environment. After drying for at least 30 minutes, the electrode was immediately

immersed into 50 mM electrolyte and linear sweep performed at 25 mV·s^{-1}. To compare, the

procedure was also performed using citrate capped AgNS.

2.4: Results and Discussion

AgNS capped with citrate, PVP, and PEG were drop-cast onto macrodisk electrodes and

analyzed via anodic stripping voltammetry (ASV) to examine the extent of particle oxidation. If little-to-no oxidation occurs from drop-cast and subsequent ASV, then single particle oxidation in said electrolyte will not occur. Thus, ASV is suitable for rapidly pre-screening electrolytes to avoid investing time in electrolytes that will not be sufficient for SPO. Figure 2.1 depicts the resulting anodic stripping voltammetry (ASV) of 40 nm PVP, citrate, and PEG capped AgNPs in 50 mM KCl. For each experiment, the same mass of AgNS (and thus silver) was drop-cast to the electrode. As such, the stripping peaks should be of similar area (~10 nC), even considering the possibility of uncontrolled detachment of particles from the electrode upon immersion in the electrolyte. However, only the citrate capped particles produced a significant stripping peak. The PEG capped particles produced a peak of approximately 2% the area of the citrate AgNS peak, and the PVP capped particles produced a peak of about 1% of the area produced by the citrate capped AgNS. The peak area from the citrate-capped particles, served as a baseline for the expected stripping peak size. Though it causes salting-out of PVP, KCl has been shown to cause salting-in of PEG.[21]

Figure 2.2 depicts the ASV of 40 nm PVP-AgNP in three different electrolytes – 50 mM KCl, LiCl, and CaCl$_2$. By using 50 mM, the extent of oxidation of silver should not be limited by availability of the compensatory anion. The salting-in CaCl$_2$ and the salting-out KCl produced the same size peaks. Interestingly, ASV in the LiCl solution did not produce a peak at all, suggesting that if it does salt in, it does not affect the electrochemical oxidation. One salting in electrolyte (CaCl$_2$) and one salting out electrolyte (KCl) produced similarly sized small peaks, and another salting in electrolyte (LiCl) not resulting in any particle oxidation indicates that salting-in of the cation does not improve electrical conductivity of the capping ligand, and that a disconnection between the electrode and the metal core remained. The concentration of the anion

in each of these experiments was identical, as was the ionic strength of KCl (salting-out electrolyte) and LiCl (salting-in electrolyte). The similar stripping peaks exhibited by KCl having an ionic strength of 0.050 M and $CaCl_2$ with an ionic strength of 0.150 M suggest that the ionic strength of LiCl (0.05 M) was not the reason for lack of anodic stripping in the LiCl electrolyte.

2.5: Conclusion

Salting-in electrolytes do not inherently promote electron tunneling through PVP to the AgNS core, which is required for particle oxidation upon contact with the electrode. Efforts to improve the electrical conductivity of PVP, thus increasing the connection between particle and electrode, require further exploration.

References

1.   Chang, S.; Chen, K.; Hua, Q.; Ma, Y.; Huang, W., Evidence for the Growth Mechanisms of Silver Nanocubes and Nanowires. *Journal of Physical Chemistry C* **2011,** *115* (16), 7979-7986.

2.   Bansal, V.; Li, V.; O'Mullane, A. P.; Bhargava, S. K., Shape dependent electrocatalytic behaviour of silver nanoparticles. *CrystEngComm* **2010,** *12*, 4280-4286.

3.   Jimenez-Lamana, J.; Slaveykova, V., Silver nanoparticle behaviour in lake water depends on their surface coating. *Science of the Total Environment* **2016,** *573*, 946-953.

4.   Chao, Y.-J.; Lyu, Y.-P.; Wu, Z.-W.; Lee, C.-L., Seed-mediated growth of Ag nanocubes and their size-dependent activities toward oxygen reduction reaction. *Int. J. Hydrogen Energ.* **2016,** *41* (6), 3896–3903.

5.   Hatta, F.; Yahya, M.; Ali, A.; Subban, R.; Harun, M.; Mohamad, A., Electrical conductivity studies on PVA/PVP-KOH alkaline solid polymer blend electrolyte. *Ionics* **2005,** *11* (5-6), 418-422.

6.   MOLYNEUX, P.; FRANK, H., Interaction of Polyvinylpyrrolidone with Aromatic Compounds in Aqueous Solution .2. Effect of Interaction on Molecular Size of Polymer. *Journal of the American Chemical Society* **1961,** *83* (15), 3175-&.

7.   Chiyokawa, S.; Suyama, K.; Takaizumi, K., Volumetric study of the interaction between chloride salts and polyvinylpyrrolidone in aqueous solution. *Journal of Solution Chemistry* **2003,** *32* (8), 743-752.

8.   Zhou, Y. G.; Rees, N. V.; Compton, R. G., The Electrochemical Detection and Characterization of Silver Nanoparticles in Aqueous Solution. *Angewandte Chemie International Edition* **2011,** *50* (18), 4219-4221.

9.   Dan, A.; Ghosh, S.; Moulik, S., The solution behavior of poly(vinylpyrrolidone): Its clouding in salt solution, solvation by water and isopropanol, and interaction with sodium dodecyl sulfate. *Journal of Physical Chemistry B* **2008,** *112* (12), 3617-3624.

10.   Hofmeister, F., Zur Lehre von der Wirkung der Salze. *Archiv für experimentelle Pathologie und Pharmakologie* **1888,** *24* (4), 247-260.

11.   MOLYNEUX, P.; FRANK, H., Interaction of Polyvinylpyrrolidone with Aromatic Compounds in Aqueous Solution 1.. Thermodynamics of Binding Equilibria and Interaction Forces. *Journal of the American Chemical Society* **1961,** *83* (15), 3169-&.

12.   MOLYNEUX, P.; FRANK, H., Interaction of Polyvinylpyrrolidone with Aromatic Compounds in Aqueous Solution .3. Model for Molecular Expansions Caused by Anionic Consolutes. *Journal of the American Chemical Society* **1964,** *86* (22), 4753-&.

13.   Taboada, M.; Galleguillos, H.; Graber, T., Compositions, densities, conductivities, and refractive indices of potassium chloride or/and sodium chloride plus PEG 4000 plus water at 298.15 and liquid-liquid equilibrium of potassium chloride or sodium chloride plus PEG 4000 plus water at 333.15 K. *Journal of Chemical and Engineering Data* **2005,** *50* (1), 264-269.

14.   Winkler, J.; Gray, H., Long-Range Electron Tunneling. *Journal of the American Chemical Society* **2014,** *136* (8), 2930-2939.

15.   Zhao, J.; Bradbury, C.; Fermin, D., Long-range electronic communication between metal nanoparticles and electrode surfaces separated by polyelectrolyte multilayer films. *Journal of Physical Chemistry C* **2008,** *112* (17), 6832-6841.

16.   Maeda, K.; Takata, T.; Hara, M.; Saito, N.; Inoue, Y.; Kobayashi, H.; Domen, K., **2005,** *- 127* (- 23), - 8287.

17.   Stuart, E. J. E.; Rees, N. V.; Cullen, J. T.; Compton, R. G., Direct electrochemical detection and sizing of silver nanoparticles in seawater media. *Nanoscale* **2012,** *5*, 174-177.

18.   Saw, E.; Blanc, N.; Kanokkanchana, K.; Tschulik, K., Time-resolved impact electrochemistry - A new method to determine diffusion coefficients of ions in solution. *Electrochimica Acta* **2018,** *282*, 317-323.

19.   Wonner, K.; Evers, M. V.; Tschulik, K., Simultaneous Opto- and Spectro-Electrochemistry: Reactions of Individual Nanoparticles Uncovered by Dark-Field Microscopy. *Journal of the American Chemical Society* **2018,** *140* (40), 12658–12661.

20.   BASinc A-1302 Electrode Polishing and Care. https://www.basinc.com/assets/library/manuals/epc.pdf.

21.   Sadeghi, R.; Jahani, F., Salting-In and Salting-Out of Water-Soluble Polymers in Aqueous Salt Solutions. *Journal of Physical Chemistry B* **2012,** *116* (17), 5234-5241.
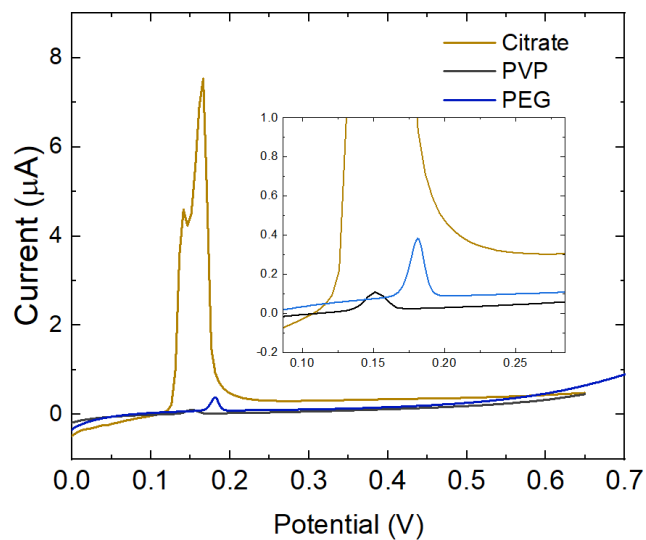
Figures

Figure 2.1: Anodic stripping voltammetry vs Ag/AgCl (sat'd KCl) at 50 V/s of electrodes modified with 40 nm AgNPs having different ligands that were drop cast onto the surface, and evaluated in 50 mM KCl
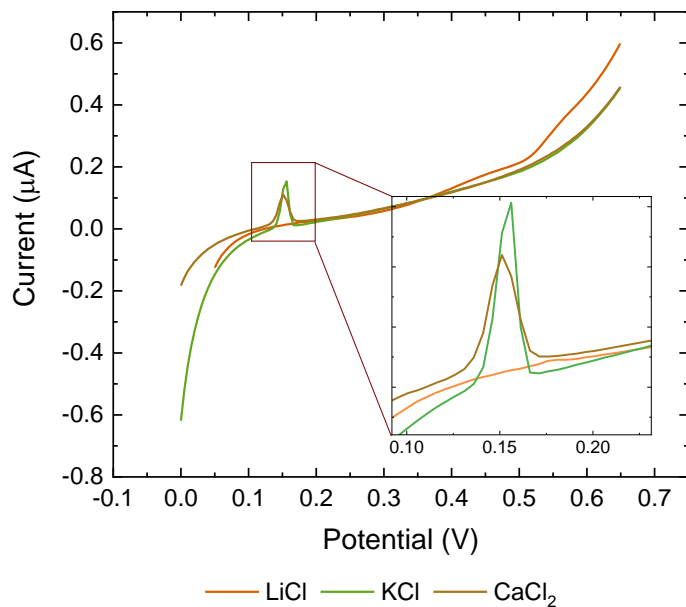

Figure 2.2: Anodic stripping voltammetry vs Ag/AgCl (sat'd KCl) at 0.05 V/s of electrodes modified with 40 nm PVP-AgNPs in different 50 mM LiCl, KCl, and CaCl$_2$

Chapter 3: Investigations into the dependance of the shape silver nanospheres, nanocubes, and nanoplates on the signal produced upon single particle oxidation

3.1 Abstract

The shape of a silver nanoparticle (AgNP) greatly affects its physical, catalytic, and antimicrobial properties. Oxidation of polyvinyl pyrrolidone capped silver nanospheres (AgNSs), nanocubes (AgNCs), and nanoplates (AgNPls) was investigated to gain a deeper understanding of their oxidative mechanisms. Upon oxidation of AgNP in potassium nitrate (KNO_3), silver oxide is formed, which readily catalyzes water oxidation. The resulting signal is a current spike followed by a step in the baseline current. The duration, integrated charge, and step height of the spike-step were analyzed for each particle shape. The time required to oxidize a particle at an anodically polarized electrode was used to probe the effect of particle shape on the mechanism in a chloride-free environment. It was discovered that oxidation rate of silver in the particle to silver oxide is dependent only on the silver content, not the available surface area, regardless of particle shape. Additionally, integration under the current spike indicates that the particles likely oxidized primarily to Ag (I) in a mixed-valance complex, even though the Pourbaix diagram indicates oxidation to Ag (II) is likely under the experimental conditions.

3.2 Introduction

Nanoparticles are synthesized in a variety of shapes, as differently shaped particles exhibit different catalytic abilities,[1] antimicrobial properties,[2, 3] optical characteristics,[4] and other behaviors.[4-6] The effect of conversion of Ag in the nanoparticle to Ag^+ and other oxidative products on nanoparticle behavior is of considerable interest. For example, the release of Ag^+ has been considered as one reason for the toxicity of AgNPs to microorganisms,[3, 7, 8] and therefore, understanding the oxidation mechanism is vital to control this phenomenon.

Managing the growth of a specific silver particle shape is often accomplished with poly-vinyl pyrrolidone (PVP),[9, 10] which also serves as the capping ligand on these particles, thus PVP was chosen as the particle capping ligand for the investigation into varying shape. Along with using the integrated charge to estimate particle size,[11] the peak width and height have been previously used to explore the oxidation kinetics.[12-15] The step in the baseline current immediately following a current spike has been observed,[16, 17] but not examined in-depth. Herein, the peak integration method of particle sizing is used in attempt to understand the chemistry occurring within the current spike and to what degree it can be separated from the subsequent step in the background current. Exploration into the effect of particle shape on the oxidation kinetics is performed using the total duration of the current spike.

To understand the effect of particle shape, PVP-capped silver nanospheres, nanocubes, and nanoplates were oxidized and the peak widths, heights, and charge passed were analyzed to investigate the mechanism of oxidation. It is hypothesized that if particles oxidize from the outside-in, a higher surface-area-to-volume ratio would result in a faster oxidation rate. If, however, the particles were to have a lattice mismatch large enough to induce breaking of the particle, the oxidation rate would not be largely affected by the surface-area-to-volume ratio.

As discussed in Chapter 2, PVP-capped particles often do not oxidize under the same conditions which citrate or even PEG-capped particles oxidize.[18] Citrate-capped particles have been shown to oxidize at ~350 mV in the presence of potassium nitrate (KNO_3) and ~150 mV in the presence of potassium chloride.[12, 18, 19] However, the oxidation frequency in KNO_3 is significantly lower than in KCl, even at potentials up to 700 mV.[15, 20] Drop-cast and linear sweep voltammetry (LSV) is often used to estimate the potential at which single particles will oxidize. When a drop-cast and LSV is performed using PVP-capped particles in KNO_3 or KCl at

potentials in which citrate-capped particles oxidize, only a small stripping peak is observed, indicating that much of the silver remains unoxidized and that there is a poor connection between the electrode and particle core. Because oxidation of PVP capped particles in halide salts has not been successful, KNO_3 was explored as a promising electrolyte. Previous work has reported the oxidation of citrate capped particles in KNO_3,[11] albeit with slower kinetics than in KCl or other halides.[14, 15] In halides, insoluble silver halides are formed which promotes the rapid oxidation. In contrast, multi-peak oxidation has been observed in nitrate electrolytes, which is generally attributed to the formation of Ag^+ causing particle repulsion from the electrode.[21, 22] Furthermore, single particle oxidation is most often explored using citrate as a capping ligand[11, 15, 22-24] To ensure the observations were in fact due to the shape of the particle without any contribution from PVP, citrate capped spheres were also investigated and compared to those of PVP capped spheres.

For these reasons, new experimental procedures compatible with PVP had to be developed. Oxidation of PVP capped AgNS, AgNC, and AgNPl was performed in 50 mM KNO_3 at 1500 and 1650 mV. The effect of particle shape on the oxidation kinetics was explored by comparing the duration of the current spike for each shape. The integration of the current spike revealed the total charge passed, and particle sizes were calculated assuming an electron transfer of 1, $^{10}/_7$, and 2 per atom of Ag oxidized in attempt to understand the chemistry occurring during particle oxidation. Finally, the step in the baseline current was evaluated to determine if formation of the AgOx species had any correlation with the original particle shape.

3.3 Experimental

3.3.1: Chemicals and materials

PVP capped AgNPls, PVP capped AgNS, and citrate capped AgNS, were purchased from

Nanocomposix (Prague, CZ), and PVP-capped silver nanocubes were synthesized in the lab of

Dr. Jingyi Chen at the University of Arkansas.[25] Figure 3.1 shows an example of a transmission

electron micrograph of the AgNCs. Agar powder and Potassium nitrate (99.99%) were purchased

from Sigma Aldrich (Germany). MasterMet2 0.2 μm silica polish and the MasterTex Polishing

pad were purchased from BASinc (West Lafayette, IN). Ultrapure water with resistance

measuring 18.2 MΩ was used for the sample preparation. All electrochemical experiments were

performed using an NPI VA-10X voltage amplifier with frequency booster (NPI Electronic,

Tamm, Germany) which had been calibrated for low-current high-frequency data collection.[26]

The chronoamperograms (CAs) were performed with current sampling at 30,000 points per

second, and a 5 kHz low pass 8-pole Bessel filter was used. A 10 μm diameter platinum working

electrode (BASi West Lafayette, IN), a homemade Ag/AgCl (3 M KCl) reference electrode

equipped with an agar junction, and a platinum wire counter electrode were used.

Transmission electron microscopy (TEM) images were captured using a TEM

microscope (JEOL JEM-1011) with an accelerating voltage of 100 kV. The hydrodynamic

diameters and zeta potentials of nanoconstructs were determined using a dynamic light scattering

instrument (Brookhaven ZetaPALS). The concentration of metals was determined using a flame

atomic absorption spectrometer (GBC 932). UV-vis spectra were taken on a UV-vis

spectrophotometer (Agilent Cary 50).

3.3.2 Methods

3.3.2.1 Electrochemical cell preparation

Prior to beginning the first CA for each suspension, the working electrode was polished

for two minutes in 0.02 μm silica polish following BASi protocol then rinsed in a stream of DI

water. To remove residual polish, the electrode was then polished in DI water on a fresh

MasterTex polishing pad. An agar junction made with 50 mM KNO$_3$ in a pasture pipette was placed on the end of the reference electrode to prevent unwanted chloride from entering the reaction. Background experiments in 50 mM KNO$_3$ at 1500 and 1650 mV to ensure no cross-contamination was present, observed by the absence of anodic spikes on the chronoamperograms.

3.3.2.2 Solution preparation

After confirming the absence of contaminant particles, a total 200 μL suspension of AgNPs in electrolyte was prepared in a shortened 1.5 mL Eppendorf centrifuge tube and immediately used. The spheres and plates were used immediately from the bottle provided by Nanocomposix, but the cubes were purified three times via centrifugation for 10 minutes at 15,000 rcf on an Eppendorf 5424R centrifuge controlled at 23°C prior to usage because their post-synthesis procedure involved only one wash. DI water was used for the re-suspension of the pellet after each cleaning. Chronoamperometry (CA) was performed at 1500 mV and 1650 mV for 10 s per CA (stepped from 110 mV). Due to the NPI's inability to hold at open circuit potential (OCP), the potential was set to 110 mV after each CA, and one second of data was collected at 110 mV prior to the collection at 1500 and 1650 mV.

3.3.2.2 Signal Processing

The peaks were analyzed using Signal Counter. The area integrated was between the onset of the current spike (at least three times the magnitude of the background current) and when the magnitude of the background noise suddenly changed, indicated by the red line in Figure 3.2. The current step was calculated from the y-position at the corresponding beginning and ending x-position. Particle size determination via current integration assumed perfect geometry in the spheres, cubes, and plates, as well as a silver density of 10.5x10^6 g·m^3 for each

shape. Particle sizes were calculated assuming an electron transfer per Ag atom of n = 1, $^{10}/_7$, and 2 and compared to the size indicated by TEM.

3.4 Results and Discussion

3.4.1: Oxidation of PVP-capped AgNCs

Overcoming the barrier to oxidation posed by PVP had to first be achieved. During an experiment containing AgNC and 50 mM KNO_3 (Figure 3.2), in-situ cleaning of the 10 μm Pt working electrode was attempted by cycling the electrode to extremely positive (1500 mV) and extremely negative (-300 mV) potentials. These cyclic voltammograms (CVs) revealed that oxidative spikes from PVP-capped particles begin appearing at ~1500 mV. CA at 1500 and 1650 mV was then performed to investigate further.

Summarized in Table 3-1, when CA was stepped to 1500 mV the charge passed during each event was lower than anticipated for the particle size. Increasing the potential to 1650 mV led to an increase in oxidation frequency and allowed for complete particle oxidation under the assumption that n is between 1 and 2 per Ag atom. The total charge passed at 1650 mV was slightly larger than anticipated for the formation of Ag (I) (Table 3-1), suggesting that there is additional chemistry occurring within the integrated current spike; whether that is electron transfer beyond n = 1 or concurrent water oxidation atop the newly formed silver oxide is to be determined.

It is known that silver oxide may serve as a catalysis for water oxidation. It has previously been hypothesized that the spike-step shape during a single particle impact with the electrode is due to the formation of AgOx nanoclusters and water oxidation occurring on the clusters.[16, 27] It is reasonable to expect that some of the water oxidation also occurs within the milliseconds-long current spike that could explain the excess charge under the peak. However, the possibility of

forming higher oxidation states of silver cannot be ignored,[28] including the possibility of mixed-valance states in oxysilver nitrate, documented to form an average electron transfer of $^{11}/_7$ and $^{10}/_7$ electrons per atom of Ag.[28-30] Furthermore, the Pourbaix diagram indicates the possibility of forming Ag (II) at the potentials used.[31] To investigate, the electrochemical sizes of the particles at 1650 mV were recalculated using number of electrons transferred per Ag atoms as $^{10}/_7$, and 2,[29, 30] the results of which are summarized in Table 3-2. Without additional characterization of the formed product, it is impossible to say definitively what is the true value of n in these experiments. The data indicate that the formation of oxysilver complexes is plausible, and that formation of Ag(II) (thus AgO) within the current spike is unlikely to be the primary reaction, based on the calculated size from the cubes.

A t-test performed comparing the electrochemical data and TEM data is summarized in Table 3-3. All electrochemically determined sizes of the cubes were statistically different from the TEM calculated value of 34 ± 3 nm calculated at the 95% confidence level. At a 99% confidence level, the sizes calculated from n = $^{10}/_7$ were statistically the same as sizing from TEM. Careful interpretation of the data is needed because the calculated size distributions are not completely Gaussian in nature. Additionally, the estimation of metal content from the TEM assumes that the AgNCs are perfect cubes. However, Figure 3.1 shows that the cubes have rounded corners and not all have the same length on all six sides. Thus, further considerations must be made when determining if the electrochemical data matches the TEM data. Rather, an analysis of the calculated t-values and percent errors in Table 3-4 indicate that a value of n = 2 is least likely and n = $^{10}/_7$ is most likely. However, the possibility of n = 2 paired with incomplete oxidation within the current spike cannot be omitted using only the present data.

3.4.2: Analysis of the oxidative signal produced by citrate and PVP capped particles

To determine if the initial current spike was due primarily to the direct oxidation of the particle, the current spike was integrated and particle size was calculated, assuming the formation of Ag(I). When the current step is large, the opportunity for water oxidation contribute to some of the current in the prescribed area increases. Additionally, larger particles produced a larger step in the background current - supporting a hypothesis proposed Willets and co-workers[17] which states that oxidation of AgNPs in KNO_3 at large potentials results in the formation of AgOx nanoclusters. A larger step in the current response can only be caused by a larger catalytic surface area. It is reasonable to assume that larger particles would form more nanoclusters, leading to a larger catalytic surface area.

Though pH was not controlled during these experiments, the local pH was estimated from the electrode size and average current step height to be around 6.8 nA. The Pourbaix diagram indicates the formation of AgO under these experimental conditions.[32] Integration under the spike indicated that Ag (I) was the primary product formed within the current spike, contrary to the Ag (II) indicated by the Pourbaix diagram. It is hypothetically possible that Ag (I) is initially formed. Then, once the AgOx nanoclusters form and the CA is within the step-portion of the region, the higher-ordered complexes are formed. Regardless of what occurs after the current spike, the data indicate that the PVP-capped particles are fully oxidized in the initial spike in current. Thus, it is the features of the spike that were used (i.e., spike width and quantity of charge under the spike) to investigate further the effects of particle shape on the oxidation.

3.4.3: Effect of particle shape on the time required for particle oxidation

Several research groups have shown that the observing the total duration or maximum height of current spikes is a powerful tool for analyzing the kinetics of single particle oxidation

when other conditions remain constant and the potential is set so that diffusion is not a limiting factor and the peak shape is properly preserved.[12, 15, 33] Additionally, the peak duration can also be affected by multi-step oxidation, wherein the particle partially or completely loses and restores contact with the electrode at a rapid pace, often faster than the sampling interval of the instrumentation.[22, 24, 34]

The peak durations for PVP capped particles at 1500 and 1650 mV were evaluated to determine how potential affects the oxidation kinetics. As the potential increased, the average peak duration decreased. At 1650 mV, the peak duration was 0.95 ± 0.450 ms and 1.32 ± 0.751 ms for the spheres and cubes, respectively. At 1500 mV the peak durations were slightly longer, at 1.20 ± 0.73 and 2.38 ± 1.69 ms for the spheres and cubes, respectively. Previous work by Tschulik and co-workers report an *increase* in peak duration of oxidized citrate capped AgNPs with an increase in potential between 500 mV and 660 mV in KNO_3 and absence of chloride. They attribute this behavior to the release of Ag^+ that causes repulsion of the particle from the electrode surface that results in a rapid multi-step oxidation.[15] In contrast, a *decrease* in peak duration with an increase potential between 1500 and 1650 mV in the same electrolyte was observed here. This result further supports the hypothesis that silver oxide species form rapidly under these conditions, *diminishing* the availability of Ag^+ and repulsion from the electrode surface, thereby decreasing the occurrence of multi-part oxidations and allowing more complete oxidation in a single event. This is parallel with previous work performed in KCl solutions in which solid AgCl is rapidly formed, and increasing chloride concentration decreases the time required for particle oxidation.[33, 35, 36] With this "rapid reaction mechanism" at large oxidizing potentials, spike widths were analyzed to determine if changing the particle shape influences the duration of the anodic spike in 50 mM KNO_3, providing insight into the oxidation mechanism.

Equation 3.1[12] relates the anticipated peak duration, t_{max}, that can be measured as the width at the spike's base, to the radius of a AgNS at overpotentials large enough that the dissolution is solubility limited,[22, 37] where r_o represents the particle's radius, ρ represents the atomic density, N_A is Avogadro's number, D is the diffusion coefficient, and C_{max} is the maximum solubility-allowed concentration.

$$t_{max} = \frac{r_0^2 \rho}{2 \ln(2) \, N_A D C_{max}}$$

(3.1)

Equation 3.1 can be reconfigured to relate t_{max} to the integrated charge, Q, under an anodic spike by substituting Equation 3.2 for r_0. Equation 3.2 is obtained by assuming the particle is a perfect sphere of volume $4/3 \, \pi \, r_o^3$ and that $n = 1$.[11]

$$r_o = \left(\frac{3 Q N_A}{4 \pi n F \rho_2} \right)^{\left(\frac{1}{3} \right)}$$

(3.2)

The resulting relationship in Equation 3.3 shows that t_{max} is proportional to $Q^{2/3}$,

$$t_{max} \propto a \times \frac{Q^{2/3} \rho_2^{1/3}}{2 \ln(2) D n^{2/3} F^{2/3} N_A^{1/3} C_{max}}$$

(3.3)

where a is a generic factor based on the particle geometry, Q the integrated charge of a single spike, ρ_2 the atomic density of silver, D the diffusion coefficient of silver oxide, N_A Avogadro's number, and C_{max} the saturation concentration of silver oxide. Comparing Equations 3.2 and 3.4, it is apparent that solving for r^2 from the equation for radius of a sphere and l^2 of a cube would result in different equations for t_{max}.

$$lr_{np} = \sqrt[3]{\frac{Q N_A}{F \rho_3}}$$

(3.4)

To investigate the effect of particle shape, six types of particles were oxidized at 1650 mV. Citrate-capped 30 nm, 50 nm, and 70 nm AgNS, and PVP-capped 30 nm AgNS, 34 nm AgNCs, and ~ 53 nm AgNPls were analyzed and compared. Figure 3.4 depicts the peak width for each particle type vs charge, $Q^{2/3}$, for all particles (a), the PVP-capped particles (b), and the citrate-capped particles (c). The degree of linearity exhibited by the PVP-capped particles of differing shapes demonstrates that at 1650 mV, the peak duration is dependent on the total charge passed during oxidation, independent of the particle shape, meaning that a in Equation 3.3 is equal to 1. This suggests that shape and surface area are less important in the mechanism of oxidation than total charge at 1650 mV. The high degree of linearity also further supports the hypothesis that water oxidation is less likely to occur within the spike of a PVP-capped particle than a citrate-capped particle. As a result, oxidation of PVP-capped particles at the electrode surface is easier to reproduce. It is suggested that the rapid formation of AgOx particles and subsequent water oxidation occurring during the ~1 ms current spike contributes to the deviation from linearity exhibited by the citrate capped AgNPs, as other groups have suggested that the pattern of new AgO_x nanocluster formation is poorly controlled.[17] To ensure the observed relationship was real and not due to instrument limitations, the NPI VA-10X NanoDAQ2 combination was characterized with a function generator to ensure the response time of the instrument matched the program signal duration from the function generator.[26]

The peak height, duration, and charge for each particle oxidized at 1650 mV is summarized in Table 3-3. In general, as the particle size increased, both the peak height and peak width increased. It has been hypothesized previously that surface area is a factor in the time needed for particle oxidation. Equation 3.4 having identical values for a indicates that shape and surface area are less important in the mechanism of oxidation than total charge at 1650 mV. To

investigate further, the relationship between the surface-area-to-volume ratio and peak height-to-area ratio of the particles was plotted (Figure 3.5). The spheres and cubes exhibit a strong linear relationship, which is expected because the surface-area-to-volume relationship is proportional to charge for these shapes.

In contrast, the data from analysis of the plates did not on the same line as the other particles. The nanoplates have a significantly different surface-area-to-volume ratio compared to the other particles. If access to counter ions were the factor controlling particle oxidation rate at 1650 mV, then the spikes produced upon nanoplate oxidation would contain a much larger peak height and much smaller peak width. The plates contained the smallest average peak width at 0.65 ms, compared to that for all particle groups. Because the sampling interval was ~19x faster than the average peak width, instrument limitation was not the cause of this deviation and the relationship is assumed to be genuine. This further supports the substitution of $Q^{2/3}$ into the t_{max} relationship, regardless of particle shape, as the linear relationship with charge passed is not an instrument artifact.

3.4.4: Analysis of the step in the background current

The separate analysis of the current spike formed initially upon oxidation and the increase in step height further supports this hypothesis of AgOx nanoclusters forming immediately after the production of Ag^+ has been previously described by the Willetts group. As silver content increased, the step height produced immediately after particle oxidation also increased. Figure 3.5 depicts the area normalized step heights, and suggests the size of the step height was generally related to the amount of silver oxidized. Assuming that the step height is primarily caused by water oxidation catalyzed by the newly formed AgOx, larger AgNPs are likely to form more AgOx nanoclusters. The process Figure 3.3 shows that the current within the

step attempts to approach the baseline immediately prior to the spike, not quite reaching its original projected current. The drift towards the original baseline is attributed to the subsequent agglomeration of AgOx nanoclusters decreasing the active surface area for water oxidation catalysis.

To determine if this increase was directly related to the amount of Ag oxidized, the ratio of step height:charge passed was plotted (Figure 3.6). Interestingly, the greater the surface-area-to-volume ratio, the larger the step height in proportion to the total charge passed within the current spike. Additionally, the 30 nm spheres and 34 nm cubes have very similar histogram shapes (Figure 3.7). These particles contain on average similar surface-area-to-volume ratios, but different amounts of silver. This suggests that the random formation of AgOx nanoclusters after particle oxidation is influenced by the surface area available during the initial particle oxidation.

3.5 Conclusion

Various citrate and PVP capped particles were analyzed via single particle oxidation in KNO$_3$ at very large over potentials (1500 and 1650 mV). Analysis of the anodic peaks produced by each particle group indicated that within the current spike, the primary electrochemical reaction involves the oxidation of Ag to Ag(I), with the possibility of some higher-ordered AgOx complexes and catalysis of water occurring during the current spike. The time for particle oxidation was dependent on the total charge passed during oxidation, independent of the particle shape, indicating that the available surface area has little-to-no influence on the reaction kinetics at 1650 mV. The step height in baseline current immediately upon particle oxidation is due to water oxidation on AgOx nanoclusters, and larger particles form more active AgOx sites for catalysis. The current of the step diminishes with time, suggesting a decrease in water oxidation that might be explained by subsequent AgOx aggregation. Additionally, the ratio of the step

height to the charge passed during particle oxidation is proportional to the surface-area-to-volume ratio of the particles.

References

1.	and, R. N.; El-Sayed, M. A., Shape-Dependent Catalytic Activity of Platinum Nanoparticles in Colloidal Solution. *Nano Letters* **2004,** *4* (7), 1343-1348.

2.	Gorka, D. E.; Osterberg, J. S.; Gwin, C. A.; Colman, B. P.; Meyer, J. N.; Bernhardt, E. S.; Gunsch, C. K.; DiGulio, R. T.; Liu, J., Reducing Environmental Toxicity of Silver Nanoparticles through Shape Control. *Environmental Science & Technology* **2015,** *49*, 10093-10092.

3.	Dakal, T.; Kumar, A.; Majumdar, R.; Yadav, V., Mechanistic Basis of Antimicrobial Actions of Silver Nanoparticles. *Frontiers in Microbiology* **2016,** *7*.

4.	Kelly, K.; Coronado, E.; Zhao, L.; Schatz, G., The optical properties of metal nanoparticles: The influence of size, shape, and dielectric environment. *Journal of Physical Chemistry B* **2003,** *107* (3), 668-677.

5.	Liz-Marzán, L. M., Tailoring Surface Plasmons through the Morphology and Assembly of Metal Nanoparticles. *Langmuir* **2006,** *22* (1), 32-41.

6.	Sherry, L. J.; Chang, S.-H.; Schatz, G. C.; Van Duyne, R. P.; Wiley, B. J.; Xia, Y., Localized Surface Plasmon Resonance Spectroscopy of Single Silver Nanocubes. *Nano Letters* **2005,** *5* (10), 2034-2038.

7.	Loza, K.; Diendorf, J.; Sengstock, C.; Ruiz-Gonzalez, L.; Gonzalez-Calbet, J.; Vallet-Regi, M.; Koller, M.; Epple, M., The dissolution and biological effects of silver nanoparticles in biological media. *Journal of Materials Chemistry B* **2014,** *2* (12), 1634-1643.

8.	El Arrassi, A.; Bellova, P.; Javid, S.; Motemani, Y.; Khare, C.; Sengstock, C.; Koller, M.; Ludwig, A.; Tschulik, K., A Unified Interdisciplinary Approach to Design Antibacterial Coatings for Fast Silver Release. *Chemelectrochem* **2017,** *4* (8), 1975-1983.

9.	Sun, Y.; Xia, Y., Shape-Controlled Synthesis of Gold and Silver Nanoparticles. *Science* **2002,** *298* (5601), 2176-2179.

10.	Chang, S.; Chen, K.; Hua, Q.; Ma, Y.; Huang, W., Evidence for the Growth Mechanisms of Silver Nanocubes and Nanowires. *Journal of Physical Chemistry C* **2011,** *115* (16), 7979-7986.

11.	Zhou, Y. G.; Rees, N. V.; Compton, R. G., The Electrochemical Detection and Characterization of Silver Nanoparticles in Aqueous Solution. *Angewandte Chemie International Edition* **2011,** *50* (18), 4219-4221.

12.	Katelhon, E.; Tanner, E.; Batchelor-McAuley, C.; Compton, R., Destructive nano-impacts: What information can be extracted from spike shapes? *Electrochimica Acta* **2016,** *199*, 297-304.

13.   Ma, W.; Ma, H.; Yang, Z.; Long, Y., Single Ag Nanoparticle Electro-oxidation: Potential-Dependent Current Traces and Potential-Independent Electron Transfer Kinetic. *Journal of Physical Chemistry Letters* **2018,** *9* (6), 1429-1433.

14.   Ngamchuea, K.; Clark, R.; Sokolov, S.; Young, N.; Batchelor-McAuley, C.; Compton, R., Single Oxidative Collision Events of Silver Nanoparticles: Understanding the Rate-Determining Chemistry. *Chemistry-a European Journal* **2017,** *23* (63), 16085-16096.

15.   Saw, E. N.; Kratz, M.; Tschulik, K., Time-resolved impact electrochemistry for quantitative measurement of single-nanoparticle reaction kinetics | SpringerLink. *Nano Research* **2017,** *10* (11), 3680-3689.

16.   Zhang, F.; Defnet, P. A.; Fan, Y.; Hao, R.; Zhang, B., Transient Electrocatalytic Water Oxidation in Single-Nanoparticle Collision. *Journal of Physical Chemistry C* **2018,** *122* (11), 6447-6455.

17.   Sundaresan, V.; Monaghan, J.; Willets, K., Monitoring Simultaneous Electrochemical Reactions with Single Particle Imaging. *Chemelectrochem* **2018,** *5* (20), 3052-3058.

18.   Toh, H. S.; Jurkschat, K.; Compton, R. G., The Influence of the Capping Agent on the Oxidation of Silver Nanoparticles: Nano-impacts versus Stripping Voltammetry. *Chemistry - A European Journal* **2015,** *21* (7), 2998-3004.

19.   Stuart, E. J. E.; Rees, N. V.; Cullen, J. T.; Compton, R. G., Direct electrochemical detection and sizing of silver nanoparticles in seawater media. *Nanoscale* **2012,** *5*, 174-177.

20.   Plowman, B.; Tschulik, K.; Walport, E.; Young, N.; Compton, R., The fate of nano-silver in aqueous media. *Nanoscale* **2015,** *7* (29), 12361-12364.

21.   Ustarroz, J.; Kang, M.; Bullions, E.; Unwin, P. R., Impact and oxidation of single silver nanoparticles at electrode surfaces: one shot v. *Chemical Science* **2017,** *8*, 1841-1853.

22.   Oja, S.; Robinson, D.; Vitti, N.; Edwards, M.; Liu, Y.; White, H.; Zhang, B., Observation of Multipeak Collision Behavior during the Electro-Oxidation of Single Ag Nanoparticles. *Journal of the American Chemical Society* **2017,** *139* (2), 708-718.

23.   Stuart, E. J. E.; Zhou, Y.-G.; Rees, N. V.; Compton, R. G., Particle-impact nanoelectrochemistry: a Fickian model for nanoparticle transport. *RCS Advances* **2012,** *2*, 12701-12705.

24.   Ustarroz, J.; Kang, M.; Bullions, E.; Unwin, P., Impact and oxidation of single silver nanoparticles at electrode surfaces: one shot versus multiple events. *Chemical Science* **2017,** *8* (3), 1841-1853.

25.   Zhang, Q.; Li, W.; Wen, L.-P.; Chen, J.; Xia, Y., Facile synthesis of Ag nanocubes of 30 to 70 nm in edge
length with CF3cOOAg as a precursor. *Chem. Eur. J* **2010,** *16*, 10234-10239.

26.   Kanokkanchana, K.; Saw, E.; Tschulik, K., Nano Impact Electrochemistry: Effects of Electronic Filtering on Peak Height, Duration and Area. *Chemelectrochem* **2018,** *5* (20), 3000-3005.

27.   Sundaresan, V.; Monaghan, J. W.; Willets, K. A., Visualizing the Effect of Partial Oxide Formation on Single Silver Nanoparticle Electrodissolution. *The Journal of Physical Chemistry C* **2018,** *122*, 3138−3145.

28.   Graff, W.; Stadelmaier, H., Higher Oxides of Silver. *Journal of the Electrochemical Society* **1958,** *105* (8), 446-449.

29.   McMillan, J. A., Higher Oxidation States of Silver. *Chemical Reviews* **1962,** *62* (1), 65-80.

30.   Sulc, O., Über das sogenannte elektrolytische Silbersuperoxyd. *Zeitschrift für anorganische Chemie* **1900,** *24* (1), 305-313.

31.   Dirkse, T. P.; Wiers, B., The Stability and Solubility of AgO in Alkaline Solutions. *Journal of the Electrochemical Society* **1959,** *106* (4), 284-287.

32.   Pargar, F.; Koleva, D. A., Polarization Behaviour of Silver in Model Solutions. *International Journal of Structural and Civil Engineering Research* **2017,** *6* (3).

33.   Saw, E.; Blanc, N.; Kanokkanchana, K.; Tschulik, K., Time-resolved impact electrochemistry - A new method to determine diffusion coefficients of ions in solution. *Electrochimica Acta* **2018,** *282*, 317-323.

34.   Sun, L.; Wang, W.; Chen, H.-Y., Dynamic Nanoparticle-Substrate Contacts Regulate Multi-Peak Behavior of Single Silver Nanoparticle Collisions. *ChemElectroChem Communications* **2018,** (5), 2995-2999.

35.   Ngamchuea, K.; Clark, R. O. D.; Sokolov, S. V.; Batchelor-McAuley, C.; Compton, R. G., Single Oxidative Collision Events of Silver Nanoparticles: Understanding the Rate-Determining Chemistry. *Chemistry - A European Journal* **2017,** *23* (63), 16085-16096.

36.   Krause, K. J.; Brings, F.; Schnitker, J.; Kätelhön, E.; Rinklin, P.; Compton, R. G.; Lemay, S. G.; Wolfrum, B., The Influence of Supporting Ions on the Electrochemical Detection of Individual Silver Nanoparticles: Understanding the Shape and Frequency of Current Transients in Nano-impacts. *Chemistry - A European Journal* **2017,** *23* (19), 4638-4643.

37.   Chen, C.-H.; Ravenhill, E. R.; Momotenko, D.; Kim, Y.-R.; Lai, S. C. S.; Unwin, P. R., Impact of Surface Chemistry on Nanoparticle–Electrode Interactions in the Electrochemical Detection of Nanoparticle Collisions. *Langmuir* **2015,** *31*, 11932-11942.

Tables

Table 3.1: Sizing of capped AgNP in 50 mM KNO3 at 1500 mV and 1650 mV, assuming particles oxidize to Ag(I). (± = one standard deviation, N = 30-126).

Particle	TEM	1500 mV	1650 mV
Citrate Spheres[a]	51 ± 6 nm	na	57 ± 10.8 nm
Citrate Spheres[a]	29 ± 3 nm	na	39 ± 9.5 nm
Citrate Spheres[a]	73 ± 8 nm	27 ± 3.4 nm	83 ± 15.0 nm
PVP Spheres[a]	29 ± 3 nm	25 nm ± 7.2	35 ± 7.0 nm
PVP Cubes[b]	34 ± 3 nm	27 nm ± 5.4	38 ± 6.2 nm

a Sizes for spheres are expressed in diameter.
b Sizes for cubes are expressed in length of a side.

Table 3.2: Calculated sizes of AgNPs analyzed in 50 mM KNO3 at 1650 mV, and assuming different numbers of electrons transferred per silver atom. (± = one standard deviation, N = 30-126).

Size from TEM (nm)	Particle Shape and Ligand	1650 mV (n=1)	1650 (n = $^{10}/_7$)	1650 (n = 2)
51 ± 6	C-spheres[a]	57 ± 10.8 nm	51 ± 10 nm	45 ± 9 nm
29 ± 3	C-spheres[a]	39 ± 9.5 nm	35 ± 8 nm	31 ± 7 nm
73 ± 8	C-spheres[a]	83 ± 15.0 nm	74 ± 13 nm	66 ± 16 nm
29 ± 3	PVP spheres[a]	35 ± 7.0 nm	31 ± 5 nm	28 ± 6 nm
34 ± 3	PVP Cubes[b]	38 ± 6.2 nm	32 ± 5 nm	29 ± 5 nm

a Sizes for spheres are expressed in diameter.
b Sizes for cubes are expressed in length of a side.

Table 3.3: Peak heights and durations for particles in 50 mM KNO$_3$ (± = one standard deviation, N = 30-126).

Particle Shape with Size from TEM (ligand)	Surface area:volume	Peak Height (nA)	Peak Duration (ms)	Charge (pC)	peak height / charge (s^{-1})
29 nm spheres (citrate)	0.21	1.21 ±0.65	1.03 ±0.41	0.34 ± 0.25	4068.6 ± 1360
50 nm spheres (citrate)	0.12	2.12 ± 1.33	2.62 ± 1.29	1.04 ± 0.63	2408.0 ± 1258.2
70 nm spheres (citrate)	0.09	5.03 ± 2.53	3.94 ± 3.37	3.08 ± 1.69	1745.2 ± 705.2
29 nm spheres (PVP)	0.21	0.79 ±0.37	0.94 ± 0.45	0.24 ± 0.24	3726.9 ± 1330.6
34 nm cubes (PVP)	0.18	1.39 ±0.79	1.32 ± 0.75	0.46 ± 2.65	3159.4 ± 1318
Plates (PVP)	~1.8	0.37 ± 0.24	0.65 ± 0.41	0.09 ± 0.21	6773.9 ± 3228.2

Table 3.4: Calculated t-values for number of electrons transferred per Ag atom, n, for experiments at 1650 mV in KNO$_3$.

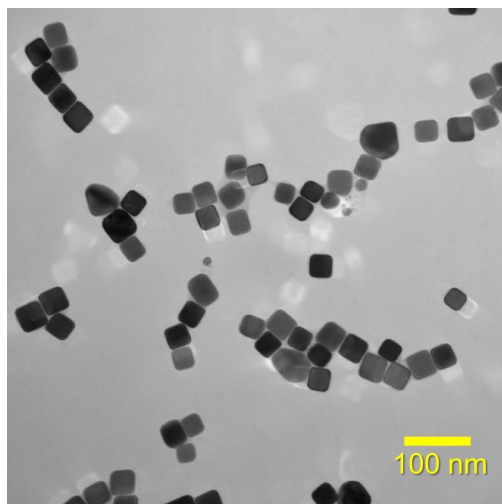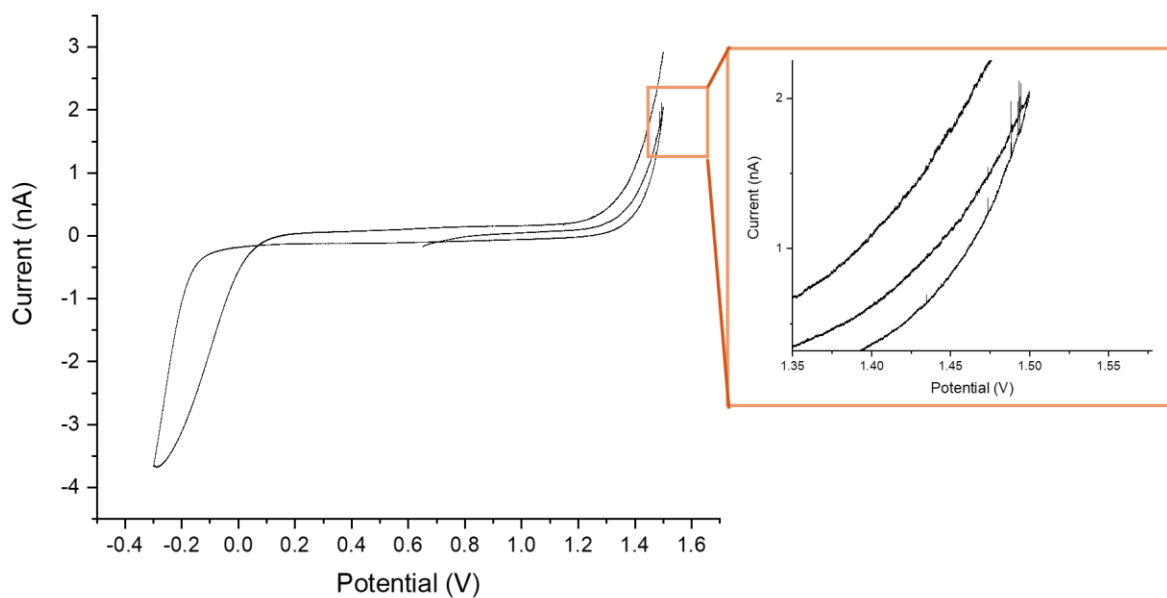| $n_{electrons}$	s_{pooled}	$\bar{x}_1$	% error	$\bar{x}_1 - \bar{x}_2$	t_{calc}
1	5.34	38	11.8	4	4.07
10/7	4.79	32	-5.9	-2	2.27
11/7	4.67	31	-8.8	-3	3.49
2	4.32	29	-14.7	-5	6.29

Figures

Figure 3.1: TEM of PVP-capped AgNCs

Figure 3.2: In-situ cleaning of the 10 μm Pt working electrode via cyclic voltammetry in 50 mM KNO$_3$ from 0.6 V to 1.5V, then to -0.3V and back to 1.5 V vs Ag/AgCl (sat'd KCl). The scan rate was 0.05 V·s^{-1}.
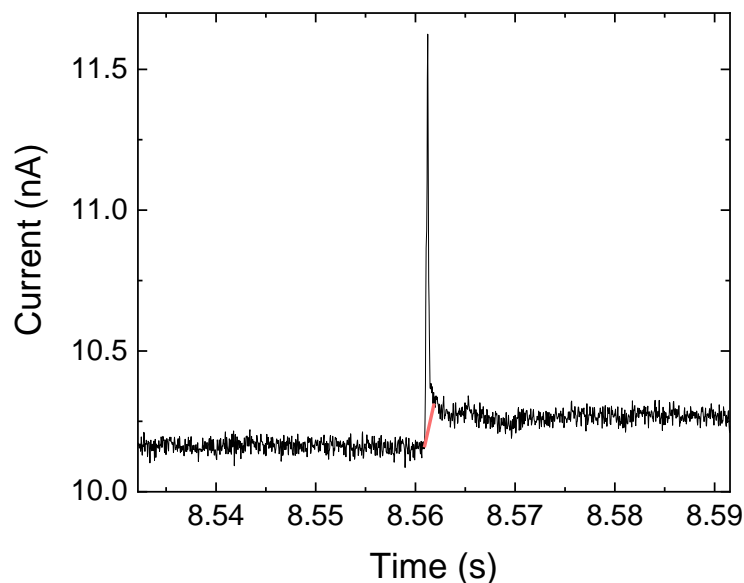
Figure 3.3: CA of a solution containing ~20 pM AgNCs in 50 mM KNO_3 at 1650 mV vs Ag/AgCl (sat'd KCl). The step in the baseline current is indicated by a red line.
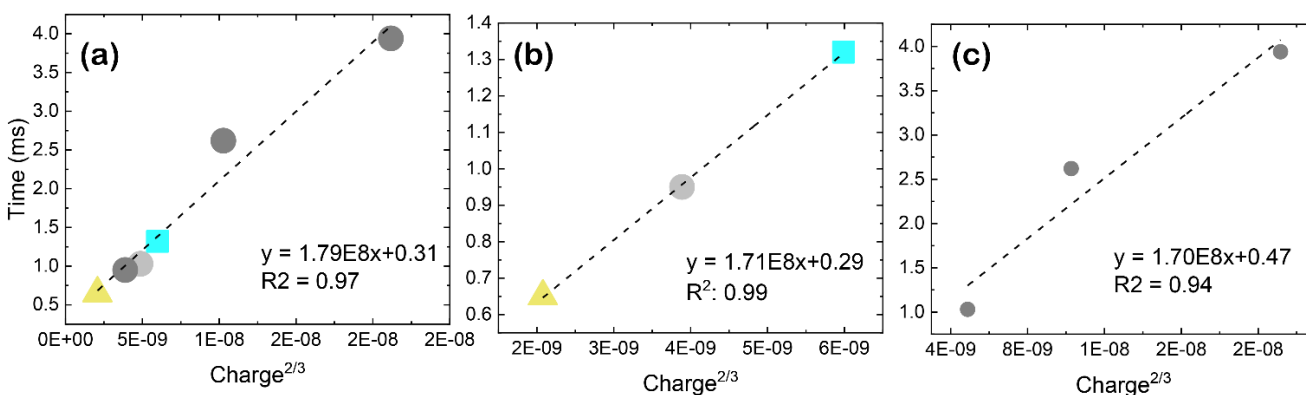

Figure 3.4: Charge vs. time of oxidation of (a) all particles, (b) all PVP-capped particles, and (c) all citrate-capped particles in 50 mM KNO_3 at 1650 mV. The shapes of the markers on the plots represent the particle shapes. Plot (a) combines the data from plots (b) and (c).
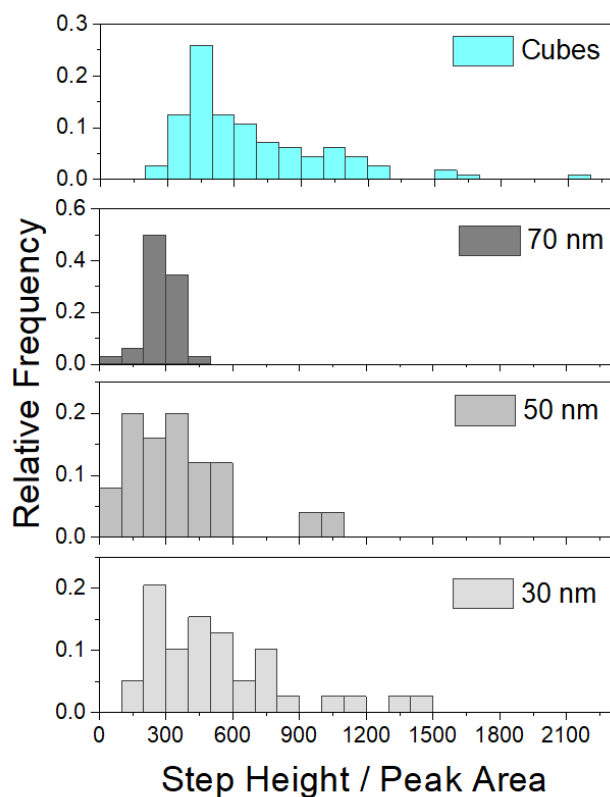
Figure 3.5: Step height divided by peak area of PVP AgNC and citrate AgNS at 1650 mV vs Ag/AgCl (sat'd KCl) in 50 mM KNO_3.
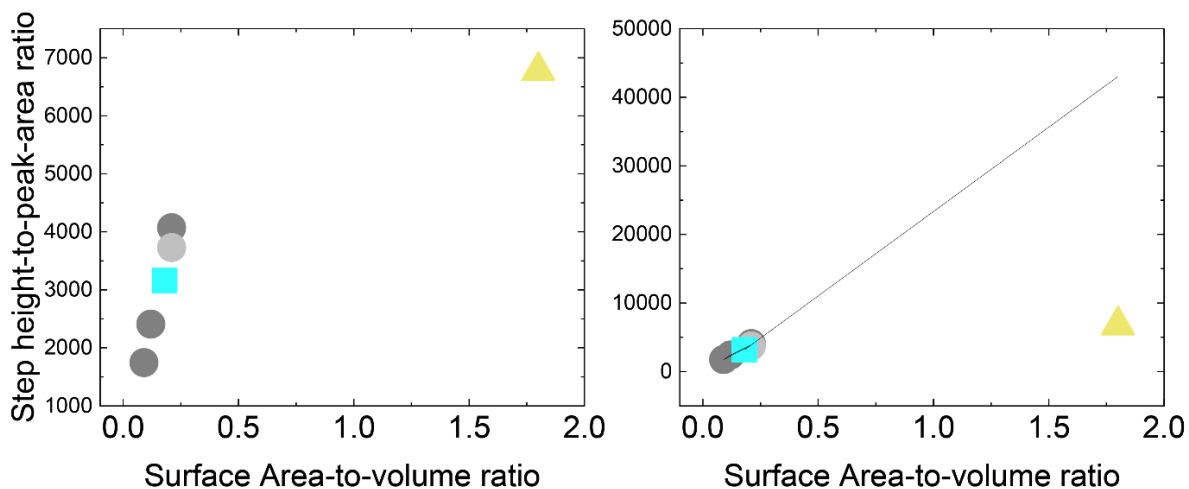
Figure 3.6: The left plot is of the raw data. The plot on the right includes the least squares linear regression for the spheres and cubes, to show where the data for plates would land if they followed the same dependence.

Figure 3.7: Peak duration of PVP capped spheres (gray) and cubes (blue) in 50 mM KNO_3. At 1650 mV, the spheres peak duration was 0.95 ± 0.450 ms for the spheres and 1.32 ± 0.751 ms for the cubes. All potentials are vs Ag/AgCl (sat'd KCl).

Chapter 4: Obtaining single particle oxidation of polymer-capped particles at lower potentials

4.1 Abstract

The single particle oxidations of poly-vinyl pyrrolidone (PVP) capped silver nanoparticles at potentials lower than 1 V vs. Ag/AgCl (sat'd KCl) were obtained in an alkaline e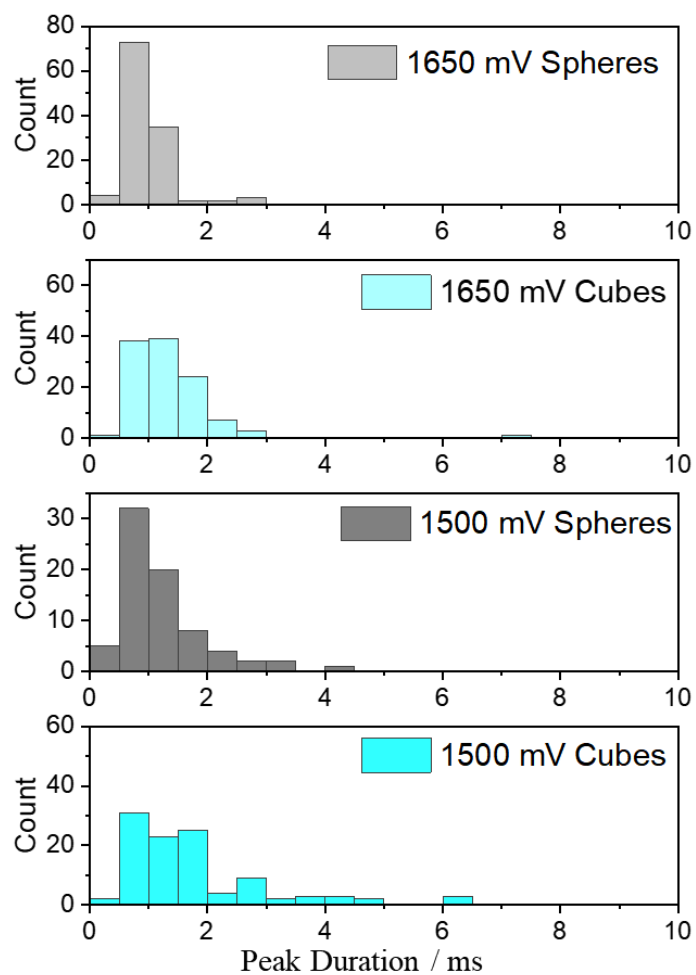nvironment (pH ~ 12.5). The shape and area of the current spike produced upon oxidation were analyzed to estimate the oxidation state of silver formed within the current spike. The previously observed oxidation of polyethylene glycol (PEG)-capped particles after they conditioned in KCl has not been effective for PVP capped particles. Using 50 mM KOH, the PVP-capped particles oxidized at the electrode immediately after mixing. The results were compared to those obtained from citrate-capped-particles to determine the contribution of the polymer capping ligand to the kinetic barrier to oxidation compared to those from less-protective citrate-capped particles. It was determined that the shape of the particle has no effect on the rate of particle oxidation under these alkaline conditions.

4.2 Introduction

Silver nanomaterials are of interest because they are present in more commercially-available products than any other nanomaterial,[1] usually for their antimicrobial properties.[2, 3] Furthermore, they are ideal candidates for catalytic applications.[4-6] The increasing usage of silver nanoparticles (AgNPs) in commercial[1] and industrial[7, 8] applications has created a further need to understand the mechanism of silver oxidation. Predicting the behaviors of nanoparticles is complex because their properties change as their morphologies (size and shape)[9-13] and capping ligands[14-16] change. Further complicating the matter, metals in the nanophase often exhibit different properties than in the bulk phase. [17-19]

Due to the heterogenous nature of nanoparticle suspension, single particle characterization provides vital detail that bulk analysis overlooks. Single particle electrochemical oxidation of nanoparticles in suspension has been used to investigate the AgNP dissolution process.[20-25] However, most of the single particle electrochemistry studies have focused on silver nanospheres (AgNSs) capped with citrate due to the relative simplicity of the synthesis and therefore the availability of this particle shape and capping agent. Tailoring the shape of the particle can enhance its performance for specific jobs while minimizing unwanted side effects.[26] Controlling the shape of the particle, for example, can increase the catalytic properties towards the hydrogen evolution and oxygen reduction reactions.[5, 27, 28] Silver nanocubes (AgNCs) and silver nanoplates (AgNPls),[6, 11, 29] can exhibit enhanced electrocatalytic activity when compared to AgNSs[5, 6] while simultaneously being less toxic to their surrounding environment.[11] However, there are fewer investigations with non-spherical than spherical nanoparticles largely because of the greater complexity of the synthesis and the high cost of purchasing from a manufacturer.

Polymer capping ligands can stabilize the particle suspension, and the polymer be chosen for a specific function. Investigating the effect of particle shape often involves using ligands capped with PVP due to its required presence in the synthesis process.[30, 31] Citrate and polyethylene glycol (PEG) capped particles electrochemically oxidize in the presence of potassium chloride (KCl).[32-34] However, PVP-capped AgNPs (PVP-AgNPs) are notoriously difficult to electrochemically oxidize.[15] This lack of reactivity is a hindrance in investigating anodic processes of single AgNPs, thus alternative conditions in which PVP-capped AgNPs can also be studied using the single entity electrochemical method must be explored. An impediment to oxidation through the PVP is the inability of surrounding ions to compensate for the change in charge upon formation of silver ions. We propose that because potassium hydroxide (KOH) is

known to increase the conductivity of PVP,[35] it also serves as a suitable electrolyte for single particle oxidation of PVP-AgNPs within an accessible electrode potential window. It also stands to reason that the kinetics of the single oxidation process will also change with the alkaline conditions. Thus, a dependence on different particle shapes is of interest. Other chemical processes, such as water oxidation, whose potential depends on pH, are expected to play a role in the single AgNP oxidations under alkaline conditions, as well.[36-39]

Herein we explore the signals produced by single particle oxidation of PVP capped AgNCs, AgNPls, and AgNS to further understand the oxidative processes in alkaline solution, which is expected to of nano silver to silver oxides (AgOx). The peak integration, height, and duration for each shape were dissected and compared to each other to explore the effect of particle shape of on the shape of the signal, as well as the chemistry occurring during AgNP oxidation under alkaline conditions. The results were then compared to citrate capped AgNS (C-AgNS) to ensure the observations were truly due to shape and not the added capping ligand.

4.3: Experimental

4.3.1: Chemicals and Materials

The 40 nm PVP-AgNS and citrate-AgNS were purchased from Nanocomposix (San Diego, CA). The PVP-AgNC and PVP-AgNPl were synthesized by the group of Dr. Jingyi Chen (University of Arkansas).[40, 41] KOH pellets were of ACS grade and purchased from Macron. Agar powder was purchased from Alfa Aesar (Ward Hill, MA). Working electrodes with a diameter of 2 mm Pt, 10 μm Pt, and 10 μm Au were purchased from CHInstruments (San Antonio, Tx). MasterTex polishing pads, 0.05 μm aluminum oxide polish, and a 10 μm Pt working electrode were purchased from BASi (West Lafayette, IN). A PalmSens4 purchased from BASinc was used for

drop-cast linear sweep experiments, an NPI VA-10x (Tamm, Germany) paired with NanoDaq2 was used for single particle chronoamperometric (CA) experiments.

4.3.2: Experimental Procedures

4.3.2.1 Drop-cast studies

Drop-cast and linear sweep voltammetry was performed on a freshly polished 2 mm Pt working electrode, Pt flag counter electrode, and homemade Ag/AgCl (Sat'd KCl) reference electrode equipped with a conductive agar junction. Initially, a 2 µL aliquot containing 50 pM PVP-AgNP and 35 mM KOH was drop-cast onto the 2 mm electrode and dried under a nitrogen flow at room temperature. Once visibly dry after 30 minutes passed, the electrode was immersed into an electrochemical cell containing 35 mM KOH and cyclic voltammetry (CV) was performed at 0.025 V·s^{-1} from 0 V to 1 V, then from 1V to -0.3 V, then to 0 V. Separate experiments were performed with a 2 µL aliquot containing 50 pM PVP AgNP in 50 mM KCl, and one with a 2 µL aliquot containing 50 pM C-AgNS in 50 mM KOH.

4.3.2.2 Single Particle Oxidation Experiments

Single particle experiments were performed using a freshly diluted particle mixture of 50 pM PVP capped particles in 50 mM KOH. CAs were performed at 0.700 V, 0.900 V, and 1.000 V for 10 seconds, and 10 runs were performed at each potential. Experiments were all performed using a freshly cleaned 10 µm Pt microdisk electrode to maximize the probability of particle oxidation upon electrode contact. To ensure there would be no current spikes from a previously made particle suspension or experiment, CAs were collected in 50 mM KOH alone (without nanoparticles) prior to all experiments. The experiment was only allowed to proceed if no stray current spikes were observed during these blank experiments. If stray spikes occurred, the working electrode was re-polished and the counter electrode was scrubbed with a kimwipe

before repeating the CAs in fresh KOH.

4.3.2.2 Analysis of Single Particle Anodic Spikes

All current spikes with a magnitude of at least three times the background current were integrated, chosen manually. The current spike was determined to end when it reached the extrapolated baseline level. If a step in current was present as observed1.0 V in KOH and 1.650 V in KNO$_3$[42], the current spike was determined to have ended when the baseline noise returned to the level observed prior to the spike in current.

4.4: Results and Discussion

4.4.1. Drop-cast AgNSs in KOH and KCl

Drop-cast and anodic stripping voltammetry was used to quickly assess the suitability of an electrolyte. Figure 4.1 compares CV responses in 50 mM KOH and 50 mM KCl for drop-cast films of PVP-capped and citrate-capped AgNS. The drop-cast PVP-AgNSs in KCl did not result in a stripping peak for the silver metal, consistent with previous observations. The drop-cast PVP-AgNSs in KOH showed a small stripping peak at ~0.3 V and a larger peak at ~0.7 V, indicating oxidation of the particles. Prior work on the oxidation of silver electrodes in KOH has revealed that during CV, Ag (II) forms through a multi-step mechanism, first forming Ag (I) before proceeding to Ag (II),[36, 43, 44] matching the observations from drop-cast AgNS.

In the initial anodic sweep for the drop-cast C-AgNS, the formation of Ag (I) occurs at 0.289 V followed by the formation of Ag (II) at 0.810 V During the following cathodic sweep Ag (II) is first reduced to Ag (I) at 0.468 V, and then Ag (I) is further reduced to Ag at 0.017 V. For the PVP capped particles, the initial oxidation to Ag (I) occurred at 0.383 V, nearly 0.10 V higher than the C-AgNS. However, the formation of Ag (II) occurred at 0.714 V, a potential nearly 0.10 V *lower* than the C-AgNS. The subsequent reduction of Ag (II) to Ag (I) occurred at

0.407 V, then was further reduced to Ag at 0.107 V. All potentials are vs. a Ag/AgCl (sat'd KCL) reference electrode. Opposite of the forward sweep, the reduction of Ag (II) for PVP-AgNS occurred at a *lower* potential than the C-AgNS, but the reduction of Ag (I) occurred at a *larger* potential. It has been documented that formation of Ag (II) is slower than formation of Ag (I).[45-47] The results suggest that the presence of PVP increases the rate, possibly due to localized trapping of hydroxide within the polymer. The same appears to occur during the formation of Ag from Ag (I).

4.4.2. Characteristics of single particle oxidation of AgNSs, AgNPs, and AgNCs in KOH

Figure 4.3 depicts representative examples of single particle oxidations for the different PVP-capped AgNPs in 50 mM KOH and stepped to 900 mV. Particles containing more silver produce larger current spikes. Anodic peaks appear in the first full CA response for a given experiment, as in Figure 4.4, immediately upon immersion of the microelectrode and the oxidation frequency remains overall stable, indicated by the overlay of the first and fifth CA run. This behavior is different than our experience with another polymer ligand, PEG-capped AgNSs in KCl solution, that required time to equilibrate before the first single particle oxidations were observed in Chapter 2. Presently, the hypothesis is that the presence of hydroxide allows electron tunneling through PVP more rapidly than the presence of KCl allows electron tunneling through citrate. Furthermore, the average magnitude of the peak increases with increased applied potential (Figure 4.5)

4.4.3. Quantitative analysis of single particle oxidation of AgNSs, AgNPs, and AgNCs in KOH

To determine the size of the particle from integration of the current (the charge) under the spike from a single particle oxidation requires knowing the geometry of the particle and the number of electrons transferred per atom. Although the cyclic voltammogram in Figure 4.1.

exhibits two distinct anodic peaks in the anodic sweep before reaching 0.900 V, which suggests

the formation of Ag(I) and then Ag (II), the particle dimensions were calculated as if a single-

electron transfer per silver atom (n = 1) occurs within the current spike. Other investigators have

hypothesized that the formation of Ag (II) occurs in a multistep process, even at high potentials.

However, higher potentials increase the reaction rate and the initial formation of Ag (I) above

appx. 0.800 V was previously unresolved.[43] Results of electrochemical sizing assuming

oxidation to Ag(I), summarized in Table 4-1, support the hypothesis of a one-electron transfer

and allowing visible resolution for the first time. Chronoamperometry was also performed at

0.750 and 1.000 V. Few significant peaks occurred at 0.750 V (Figure 4.5). Sizing of particles

oxidized at 1.000 V agreed with the results from 0.900 V.

Integration of current spikes from PVP-AgNS led to a calculated diameter of 29 ± 4 nm,

significantly smaller than the manufacturer-reported size of 39 nm based on TEM measurements.

Typically, sizing NPs via TEM assumes a near-perfect sphere, which leads to an overestimation

of diameter. Previously, research groups have reported that AgNSs are generally more

icosahedral in shape, and only approximately 60% of the expected charge assuming a perfect

sphere, is actually present in the imperfect sphere-like particles.[48]

Analysis of the spikes from PVP-AgNCs further confirmed that complete oxidation was

occurring in 50 mM KOH at 0.900 V. The electrochemical experiments yielded a length of a side

of the AgNCs to be 32 ± 11 nm. The TEM-determined size was 32 nm. The similarity between

these two measurements for cubes in comparison to that for spheres can be explained by the

nanocubes having fewer structural anomalies, and therefore their size as determined by TEM is

more accurate than those of spheres.

For calculation of the size of the AgNPls (depicted in the TEM image in Figure 4.2), they were assumed to be cylinders containing a diameter much larger than the height. The thickness of the plates is more homogenous than the diameter, so the average thickness of 8.5 nm, based on TEM measurements, was used in calculating the plate diameter of 18 ± 5 nm from the integrated current of the spikes. Compared to the TEM measured diameter of 22 ± 4 nm, the standard deviations slightly overlap.

The width of the base of a spike is representative of the time scale of the oxidation of the AgNP. Figure 4.3 shows that this maximum time (t_{max}), regardless of the particle shape, is linearly dependent on charge$^{2/3}$ with an R^2 value of 0.99. The relationship between t_{max} and charge$^{2/3}$ was described previously[42, 49] and is shown in Equation 4.1,

$$t_{max} \propto a \times \frac{Q^{2/3}\rho_2^{1/3}}{2\ln(2)Dn^{2/3}F^{2/3}N_A^{1/3}C_{max}}$$

4.1.

where a represents the shape-dependent variable, Q represents the integrated charge, ρ the atomic density of silver, D the diffusion coefficient of the released AgOx species, N_A Avogadro's number, and C_{max} the maximum concentration of AgOx. The shape-dependent constant must be unity, indicating that the rate of AgNP oxidation is independent of particle shape and surface area, and that oxidation is asymmetric.[38] If the particles were oxidizing from the outside-in, the time required for particle oxidation would be dependent on the surface area. However, the results indicate that the outer layers and the inner layers oxidize simultaneously and therefore are independent of shape. These results are in agreement with those performed previously in KNO_3 at large overpotentials.[42] Furthermore, the slope of the line (3.6×10^8) is on the same order of magnitude as the theoretical slope of 1.8×10^8, calculated using a theoretical diffusion coefficient of 1.18×10^{-5} cm$^2 \cdot$s and C_{max} of 1.23×10^{-7} mol$\cdot$cm^2. The theoretical diffusion coefficient was calculated by estimating the size of a single Ag_2O molecule from its bond length[50] and applying the Stokes-Einstein equation, while

C_{max} was calculated using the reported k_{sp} value, $2x10^{-8}$,[51] for Ag_2O. In the event that diffusion of silver through silver oxide (D = $3.7x10^6$ $cm^2 \cdot s$)[52] is limiting the reaction rate, the estimated slope of peak duration vs. charge$^{2/3}$ is then $3.46x10^8$.

4.5: Conclusions

A quantitative analysis of single particle oxidation in KOH solution of PVP-capped AgNPs of spheres, cubes, and plates suggests that particle shape is unimportant in dictating the rate of the oxidation. This was also found in prior work at large overpotentials in KNO_3 solution. This knowledge is important in addressing contributions of shape in chemical processes of nanoparticles, their reactivity, release, and delivery of their constituent parts. In addition, the unique properties of capping ligands and their consequential interactions with electrolyte must be considered for different applications. For the purpose of quantifying the number of atoms in and estimate size of polymer capped AgNPs, that normally exhibit resistance or slowed oxidation in other electrolytes, single particle oxidation in KOH solution can be used within an easily accessible potential range to attain that information. Immediate oxidation in an AgNP/KCl suspension may not immediately occur for PEG capped particles or at all for PVP-capped particles, where hydroxides are more appropriate. A systematic approach for choosing an electrolyte based on the capping ligand properties still needs developed in order to obtain particle oxidation through all available capping ligands. At this time KOH is a reasonable next step when halide electrolytes have failed to produce single particle oxidations, so long as the system can tolerate an alkaline environment.

References

1.   Vance, M. E.; Kuiken, T.; Verjerano, E. P.; McGinnis, S. P.; Hochella, M. F.; Rejeski, D.; Hull, M. S., Nanotechnology in the real world: Redeveloping the nanomaterial consumer products inventory. *Bielstein Journal of Nanotechnology* **2015,** *5*, 1769-1780.

2.   Dakal, T.; Kumar, A.; Majumdar, R.; Yadav, V., Mechanistic Basis of Antimicrobial Actions of Silver Nanoparticles. *Frontiers in Microbiology* **2016,** *7*.

3.   Loza, K.; Diendorf, J.; Sengstock, C.; Ruiz-Gonzalez, L.; Gonzalez-Calbet, J.; Vallet-Regi, M.; Koller, M.; Epple, M., The dissolution and biological effects of silver nanoparticles in biological media. *Journal of Materials Chemistry B* **2014,** *2* (12), 1634-1643.

4.   Campbell, F. W.; Belding, S. R.; Baron, R.; Xiao, L.; Compton, R. G., The Hydrogen Evolution Reaction at a Silver Nanoparticle Array and a Silver Macroelectrode Compared: Changed Electrode Kinetics between the Macro- and Nanoscales. *The Journal of Physical Chemistry C* **2009,** *113* (33), 14852-14857.

5.   Bansal, V.; Li, V.; O'Mullane, A. P.; Bhargava, S. K., Shape dependent electrocatalytic behaviour of silver nanoparticles. *CrystEngComm* **2010,** *12*, 4280-4286.

6.   Lee, C.-L.; Tsai, Y.-L.; Huang, C.-H.; Huang D, K.-L., Performance of silver nanocubes based on electrochemical surface area for catalyzing oxygen reduction reaction. *Electrochemistry Communications* **2013,** *29*, 37–40.

7.   Chen, S.; Murray, R.; Feldberg, S., Quantized capacitance charging of monolayer-protected Au clusters. *Journal of Physical Chemistry B* **1998,** *102* (49), 9898-9907.

8.   Herves, P.; Perez-Lorenzo, M.; Liz-Marzan, L.; Dzubiella, J.; Lu, Y.; Ballauff, M., Catalysis by metallic nanoparticles in aqueous solution: model reactions. *Chemical Society Reviews* **2012,** *41* (17), 5577-5587.

9.   and, R. N.; El-Sayed, M. A., Shape-Dependent Catalytic Activity of Platinum Nanoparticles in Colloidal Solution. *Nano Letters* **2004,** *4* (7), 1343-1348.

10.   Leif J. Sherry; Shih-Hui Chang; George C. Schatz, a.; Duyne*, R. P. V.; and, B. J. W.; Xia, Y., Localized Surface Plasmon Resonance Spectroscopy of Single Silver Nanocubes. *Nano Letters* **2005,** *5* (10), 2034-2038.

11.   Gorka, D. E.; Osterberg, J. S.; Gwin, C. A.; Colman, B. P.; Meyer, J. N.; Bernhardt, E. S.; Gunsch, C. K.; DiGulio, R. T.; Liu, J., Reducing Environmental Toxicity of Silver Nanoparticles through Shape Control. *Environmental Science & Technology* **2015,** *49*, 10093-10092.

12.   Liz-Marzán*, L. M., Tailoring Surface Plasmons through the Morphology and Assembly of Metal Nanoparticles. *Langmuir* **2006,** *22* (1), 32-41.

13.   Liang, T.; Zhou, D.; Wu, Z.; Shi, P., Size-dependent melting modes and behaviors of Ag nanoparticles: a molecular dynamics study - IOPscience. *Nanotechnology* **2017,** *28* (48), 1-15.

14.   Hwu, S.; Blickenstorfer, Y.; Ihle, S. J.; Garzuel, M.; Forró, C.; Schmidheini, L.; Demkó, L.; Vörös, J., Theoretical and Experimental Investigation of Ligand-Induced Particle–Particle Interactions. *Journal of Physical Chemistry C* **2020,** *124* (2), 1566-1574.

15.   Toh, H. S.; Jurkschat, K.; Compton, R. G., The Influence of the Capping Agent on the Oxidation of Silver Nanoparticles: Nano-impacts versus Stripping Voltammetry. *Chemistry - A European Journal* **2015,** *21* (7), 2998-3004.

16.   Zhang, F.; Durham, P.; Sayes, C. M.; Lau, B. L. T.; Bruce, E. D., Particle uptake efficiency is significantly affected by type of capping agent and cell line. *Journal of Applied Toxicology* **2015,** *35*, 1114-1121.

17.   Ananikov, V. P.; Beletskaya, I. P., Toward the Ideal Catalyst: From Atomic Centers to a "Cocktail" of Catalysts. *Organometallics* **2012,** *31* (5), 1595-1604.

18.   de Heer, W. A., The physics of simple metal clusters: experimental aspects and simple models. *Reviews of Modern Physics* **1993,** *65* (3), 611-676.

19.   Zeng, J.; Zhang, Q.; Chen, J.; Xia, Y., A Comparison Study of the Catalytic Properties of Au-Based Nanocages, Nanoboxes, and Nanoparticles. *Nano Letters* **2009,** *10* (1), 30-35.

20.   Xiao, X.; Fan, F.-R. F.; Zhou, J.; Bard, A. J., Current Transients in Single Nanoparticle Collision Events. *JACS* **2008,** *130* (45), 16669-16677.

21.   Bard, A. J.; Zhou, H.; Kwon, S. J., Electrochemistry of Single Nanoparticles via Electrocatalytic Amplification. *Israel Journal of Chemistry* **2010,** *50* (3), 267-276.

22.   Zhou, Y. G.; Rees, N. V.; Compton, R. G., The Electrochemical Detection and Characterization of Silver Nanoparticles in Aqueous Solution. *Angewandte Chemie International Edition* **2011,** *50* (18), 4219-4221.

23.   Ustarroz, J.; Kang, M.; Bullions, E.; Unwin, P., Impact and oxidation of single silver nanoparticles at electrode surfaces: one shot versus multiple events. *Chemical Science* **2017,** *8* (3), 1841-1853.

24.   Saw, E.; Grasmik, V.; Rurainsky, C.; Epple, M.; Tschulik, K., Electrochemistry at single bimetallic nanoparticles - using nano impacts for sizing and compositional analysis of individual AgAu alloy nanoparticles. *Faraday Discussions* **2016,** *193*, 327-338.

25.   Hao, R.; Fan, Y.; Zhang, B., Imaging Dynamic Collision and Oxidation of Single Silver Nanoparticles at the Electrode/Solution Interface. *Journal of the American Chemical Society* **2017,** *139* (35), 12274-12282.

26.   Gorka, D. E.; Osterberg, J. S.; Gwin, C. A.; Colman, B. P.; Meyer, J. N.; Bernhardt, E. S.; DiGulio, R. T.; Liu, J., Reducing Environmental Toxicity of Silver Nanoparticles through Shape Control. *Environmental Science & Technology* **2015,** *49*, 10093-10092.

27.   Joya, K.; Ahmad, Z.; Joya, Y.; Garcia-Esparza, A.; de Groot, H., Efficient electrochemical water oxidation in neutral and near-neutral systems with a nanoscale silver-oxide catalyst. *Nanoscale* **2016,** *8* (32), 15033-15040.

28.   Li, D.; Wei, C.; Wang, Q.; Liu, L.; Zhong, D.; Hao, G.; Zuo, Z.; Zhao, Q., Oxygen Evolution on in Situ Selective Formation of AgO: Plane Is the Key Factor. *Journal of Physical Chemistry C* **2019,** *123* (17), 10967-10973.

29.   Moreau, A.; Ciracì, C.; Mock, J. J.; Hill, R. T.; Wang, Q.; Wiley, B. J.; Chilkoti, A.; Smith, D. R., Controlled-reflectance surfaces with film-coupled colloidal nanoantennas. *Nature* **2012,** *492*, 86-89.

30.   Chang, S.; Chen, K.; Hua, Q.; Ma, Y.; Huang, W., Evidence for the Growth Mechanisms of Silver Nanocubes and Nanowires. *Journal of Physical Chemistry C* **2011,** *115* (16), 7979-7986.

31.   Sun, Y.; Xia, Y., Shape-Controlled Synthesis of Gold and Silver Nanoparticles. *Science* **2002,** *298* (5601), 2176-2179.

32.   Stuart, E. J. E.; Rees, N. V.; Cullen, J. T.; Compton, R. G., Direct electrochemical detection and sizing of silver nanoparticles in seawater media. *Nanoscale* **2012,** *5*, 174-177.

33.   Zhang, F.; Edwards, M. A.; Hao, R.; White, H. S.; Zhang, B., Collision and Oxidation of Silver Nanoparticles on a Gold Nanoband Electrode. *The Journal of Physical Chemistry C* **2017,** *121*, 23564-23573.

34.   Saw, E. N.; Kratz, M.; Tschulik, K., Time-resolved impact electrochemistry for quantitative measurement of single-nanoparticle reaction kinetics | SpringerLink. *Nano Research* **2017,** *10* (11), 3680-3689.

35.   Hatta, F.; Yahya, M.; Ali, A.; Subban, R.; Harun, M.; Mohamad, A., Electrical conductivity studies on PVA/PVP-KOH alkaline solid polymer blend electrolyte. *Ionics* **2005,** *11* (5-6), 418-422.

36.   Ambrose, J.; Barradas, R. G., The Electrochemical Formation of Ag2O in KOH Electrolyte. *Electrochimica Acta* **1974,** *19* (11), 781-786.

37.   Pound, B. G.; Macdonald, D. D.; Tomlinson, J. W., The electrochemistry of silver in KOH at elevated temperatures—II. Cyclic voltammetry and galvanostatic charging studies. *Electrochimica Acta* **1980,** *25* (5), 563-573.

38.   Sundaresan, V.; Monaghan, J. W.; Willets, K. A., Visualizing the Effect of Partial Oxide Formation on Single Silver Nanoparticle Electrodissolution. *The Journal of Physical Chemistry C* **2018,** *122*, 3138−3145.

39.   Sundaresan, V.; Monaghan, J.; Willets, K., Monitoring Simultaneous Electrochemical Reactions with Single Particle Imaging. *Chemelectrochem* **2018,** *5* (20), 3052-3058.

40.   Zhang, Q.; Li, W.; Moran, c.; Zeng, J.; Chen, J.; Wen, L.-P.; Xia, y., Seed-Mediated Synthesis of Ag Nanocubes with Controllable Edge Lengths in the Range of 30−200 nm and Comparison of Their Optical Properties. *Journal of the American Chemical Society* **2010,** *132*, 11372-11378.

41.   Xiong, Y.; Washio, I.; Chen, J.; Cai, H.; Li, Z.-Y.; Xia, Y., Poly(vinyl pyrrolidone): A Dual Functional Reductant and Stabilizer for the Facile Synthesis of Noble Metal Nanoplates in Aqueous Solutions. *Langmuir* **2006,** *22* (20), 8563-8570.

42.   Sikes, J. C. Electrochemical Oxidation of Individual Silver Nanoparticles: Exploring the Effect of Particle Shape, Capping Ligand, Electrolyte, and Potential on the Signal. University of Arkansas, 2021.

43.   Hepel, M.; Tomkiewicz, M., Study of the Initial Stages of Anodic Oxidation of Polycrystalline Silver in KOH Solutions. *Journal of the Electrochemical Society* **1984,** *131* (6), 1288-1294.

44.   Sulc, O., Über das sogenannte elektrolytische Silbersuperoxyd. *Zeitschrift für anorganische Chemie* **1900,** *24* (1), 305-313.

45.   Dirkse, T. P.; Wiers, B., The Stability and Solubility of AgO in Alkaline Solutions. *Journal of the Electrochemical Society* **1959,** *106* (4), 284-287.

46.   Fleischmann, M.; Lax, D. J.; Thirsk, H. R., Electrochemical Studies of Ag2O/AgO Phase Change in Alkaline Solutions. *Transactions of the Faraday Society* **1968,** *64* (551P), 3137-3146.

47.   Droog, J. M. M.; Hjuisman, F., Electrochemical Formation and Reduction of Silver Oxides in Alkaline Media. *Journal of Electroanalytical Chemistry* **1980,** *115* (2), 211-224.

48.   Sokolov, S. V.; Batchelor-McAuley, C.; Tschulik, K.; Fletcher, S.; Compton, R. G., Are Nanoparticles Spherical or Quasi-Spherical? *Chemistry - A European Journal* **2015,** *21* (30), 10741-10746.

49.   Katelhon, E.; Tanner, E.; Batchelor-McAuley, C.; Compton, R., Destructive nano-impacts: What information can be extracted from spike shapes? *Electrochimica Acta* **2016,** *199*, 297-304.

50.   Trushin, E. V.; Zilberberg, I. L., Anion-radical oxygen centers in small (AgO)n clusters: Density functional theory predictions. *Chemical Physics Letters* **2013,** *560*, 37-41.

51.   Biedermann, G.; Sillén, L. G.; Lindberg, B.; Dodson, R., Studies on the Hydrolysis of Metal Ions. Part 30. A Critical Survey of the Solubility Equilibria of Ag2O. *Acta Chemica Scandinavica* **1960,** *14*, 717-725.

52.   Farhat, E.; Donnadieu, A.; Robin, J., Cinétique de la croissance de couches minces d'oxyde d'argent AgO. *Thin Solid Films* **1975,** *29* (2), 319-324.

Tables

Table 4-1: Sizing of PVP capped AgNP in 50 mM KOH, N = 112-170

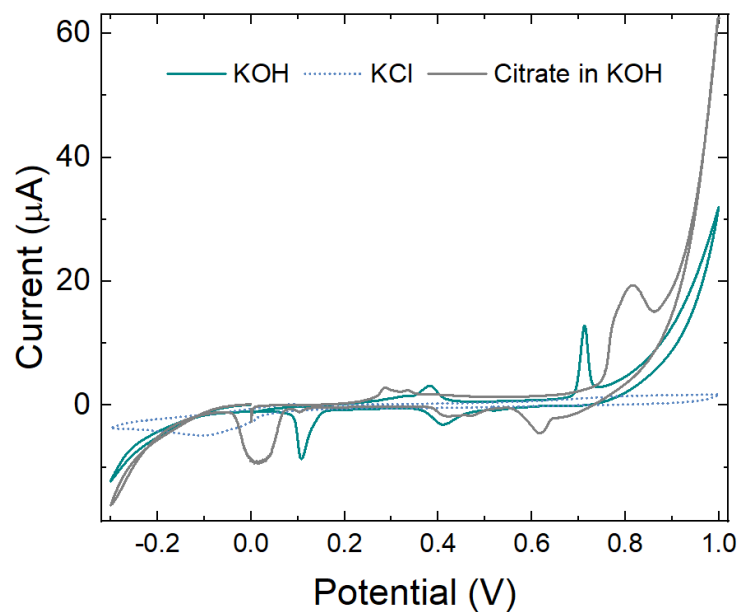| Particle	TEM	900 mV	1000 mV
Sphere	39 ± 4 nm	29 nm ± 4	31 ± 4 nm
Cube	32 ± 7 nm	33 nm ± 11	33 ± 10 nm
Plate	22 ± 4 nm	18 nm ± 5	

Figures

Figure 4.1: Drop-cast and linear sweep vs Ag/AgCl (sat'd KCl) of citrate and PVP-capped AgNS in 50 mM KOH (blue) and KCl (gray). Cyclic voltammetry began at 0 mV for KOH and 100 mV for KOH, then was anodically swept to 1000 mV at 25 mV·s^{-1}
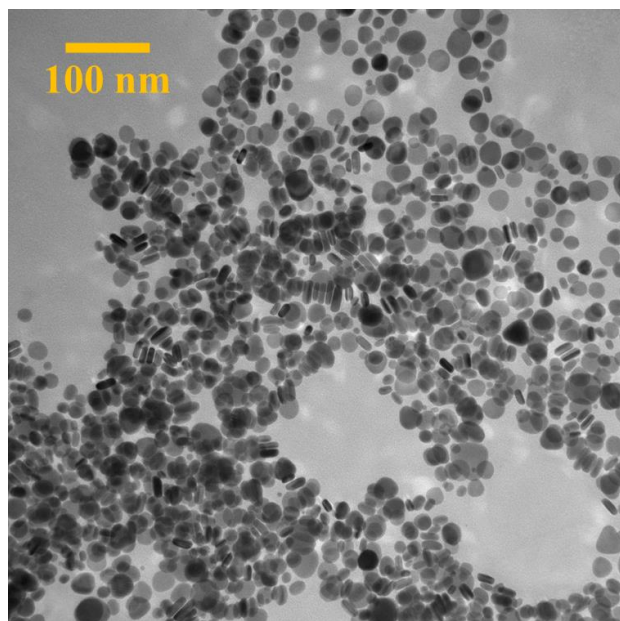

Figure 4.2: TEM of PVP Ag nanoplates synthesized by Isabelle Niyonshunti. TEM image was also provided by Isabelle Niyunshanti
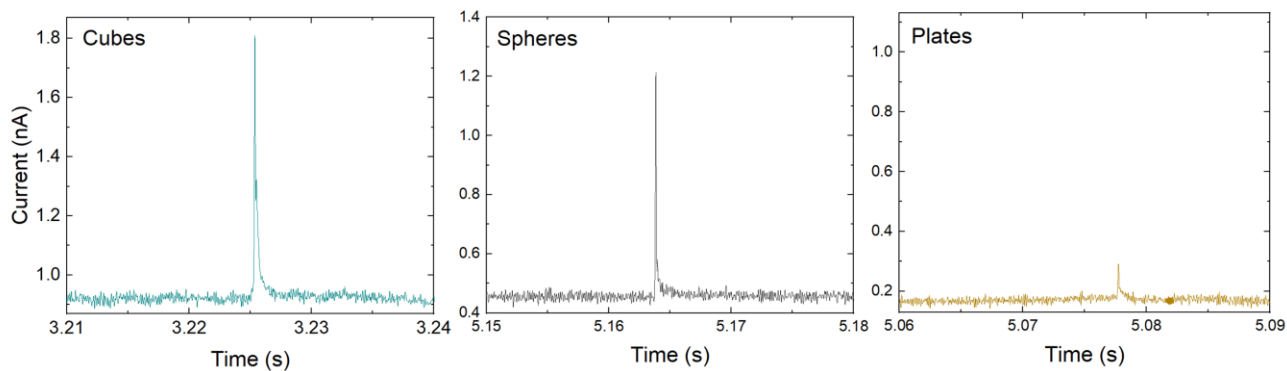
Figure 4.3: Chronoamperograms of PVP capped 32 nm cubes, 40 nm spheres, and 22 nm plates at 0.900 V in 50 mM KOH. The magnitude of each y-axis is 1 nA, and the magnitude of each x-axis is 0.03 s.
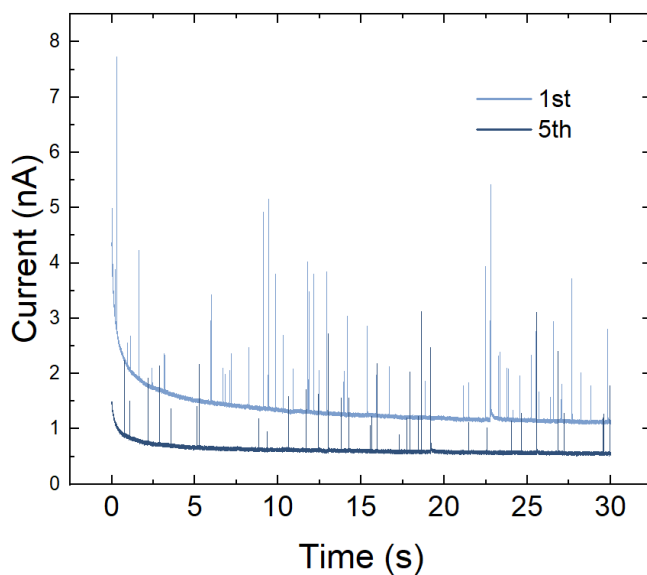

Figure 4.4: Overlay of the first and fifth chronoamperogram of PVP-AgNC in 50 mM KOH. The potential was stepped to 900 mV.
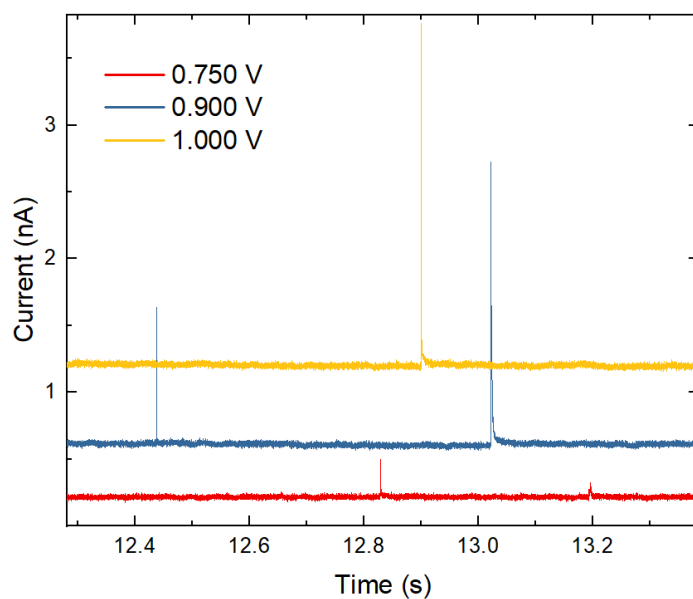
Figure 4.5: Chronoamperograms of 40 nm PVP-AgNS in 50 mM KOH at 0.750 V, 0.90 V, and 1.00 V vs Ag/AgCl (sat'd KCl). There was not an offset applied to any of the chronoamperograms.
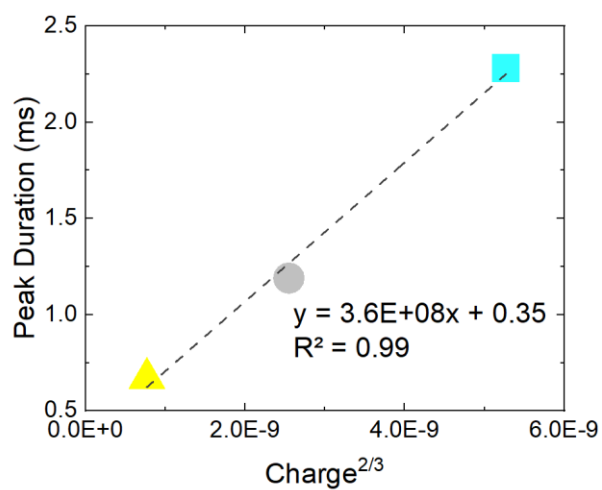

Figure 4.6: Time required for oxidation of varyingly shaped PVP-AgNP in 50 mM KOH at 900 mV vs. the total charge passed during oxidation. The reference electrode was Ag/AgCl (sat'd KCl).
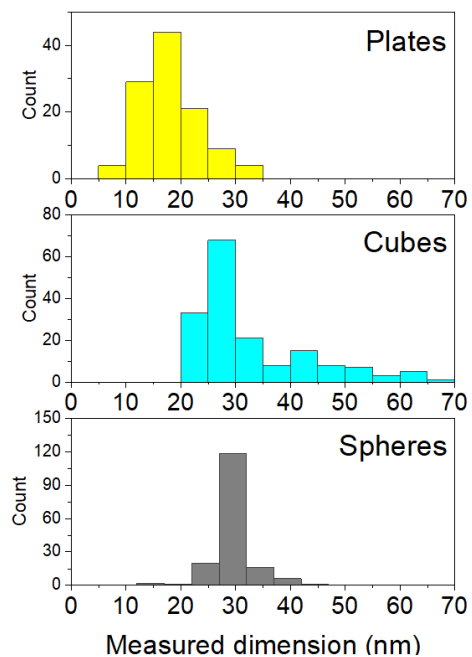
Figure 4.7: Histograms of the plate diameters, cube lengths, and sphere diameters from electrochemical experiments performed at 900 mV vs Ag/AgCl in 50 mM KOH.

Chapter 5: Combined redox magnetohydrodynamics and dark field microscopy for high-throughput characterization of a nanoparticle mixture

5.1 Abstract

A Flow-DFM system was developed as a method for high-throughput single particle differentiation and tracking. Redox magnetohydrodynamics and dark-field microscopy were coupled to provide size information from a flowing mixture of 82 ± 8.4 nm silver and 140 ± 9.9 nm gold-coated silica nanoparticles. Herein we demonstrate the ability to bidirectionally move the sample solution across the field of view without the use of a mechanical pump, allowing for a miniaturized analysis method absent of physical vibrations within the experimental cell. Redox magnetohydrodynamics provides continuous, uniform flow within a cell through the use of a body force, allowing for highly controlled fluid movement and resulting in easier data analysis. Additionally, the amounts of potentially hazardous nanomaterials required for analysis are minimized due to the elimination of the inlet and outlet. Using the combined redox magnetohydrodynamics dark field microscopy (RMHD-DFM) approach, a group of 365-421 nanoparticles in a flowing suspension were differentiated from each other by localized surface plasmon resonance and sized by their Brownian motion. The ability to immediately reverse the flow direction allowed for re-analysis of the particles, allowing for increased statistical analysis to be performed on the particle population.

5.2 Introduction

In recent decades there has been a rising interest in both the commercial and industrial usage of nanomaterials that outpaces the understanding of fundamental nanomaterial properties. Nanomaterials are being researched and utilized for applications ranging from catalysis in alternative fuel cells[1-3] to antimicrobials in medical devices.[4, 5] It has been observed that the

physical properties of materials in the nanophase differ from those in the bulk phase, which is primarily attributed to the higher surface energy of the material in the nano-scale.[2, 6-8] The differences are not only affected by the variation in the particle composition, but are also strongly dependent on the particle's size and shape.[7, 9-11] Thus, there is knowledge gap with respect to the properties of nanomaterials and their incorporation into products.

Characterization of nanoparticles remains challenging. Three commercially available methods are transmission electron microscopy (TEM), dynamic light scattering (DLS), and nanoparticle tracking analysis (NTA). TEM is generally performed in a vacuum but can achieve high spatial resolution and imaging of the structural features of individual nanoparticles. DLS is performed in solution, which allows for real-time monitoring of processes taking place in suspension, but the measured hydrodynamic radius is an average of the population and individual information is lost. Additionally, due to the intensity scaling of 10^6, the presence of just a few larger particles can drastically alter the calculated average size, leading to an inaccurate idea of the distribution. NTA, which combines microscopy with light scattering, provides information on individual particles but offers no particle differentiation methods. The ability to monitor and differentiate individual nanoparticles by localized surface plasmon resonance (LSPR) in-situ and in-operando in a relatively inexpensive way remains the advantage of DFM over TEM and DLS.

The LSPR phenomenon, first described by Michael Faraday in 1857,[12] is based on the interaction of light with nanostructures and determines the visual color of plasmonic nanoparticle suspensions. Because only the scattered light is detected in DFM, it a useful tool for observing individual nanoparticles that exhibit strong LSPRs such as silver, gold, and copper, [13-16] as well as for monitoring chemical reactions of themselves or on their surfaces.[17-20] Although the size of nanoparticle cores is well below the spatial resolution limit of a light microscope, the strong

LSPR of these particles makes the tracking of them possible. DFM combined with nanoparticle tracking analysis has been previously used to determine the diffusion coefficients of nanomaterials by tracking a static suspension of single particles.[13] In addition to providing diffusion coefficients, single particle tracking methods have been developed to monitor the behavior of particles in solution[21-23] and the uptake of particles into bacterium cells.[24]

Because redox-magnetohydrodynamics (RMHD) microfluidics is driven by a body force, the fluid being moved can be contained within the sample chamber. Thus an inlet, outlet, and reservoir of fluid are not required and nanoparticles in very small sample volumes of a few microliters can be analyzed which results in lower overall costs and less waste of nanomaterials, of which environmental effects are poorly understood.[25-29] The approach of employing dark-field microscopy (DFM) for the tracking and analyzing nanoparticles and RMHD for highly controlled sample delivery described herein provides a method of tracking and analysis while simultaneously minimizing nanoparticulate waste.

To observe the diffusion of nanomaterials, sources of fluid movement and vibrations must be managed. Thus, the usage of mechanical pumps for sample movement and delivery can be troublesome, as they create pulsed flow and typically involve a parabolic flow profile.[30, 31] Electroosmotic pumping has been used to overcome the pulsed flow, but requires a high electric field.[30] As such, diffusion coefficient analysis is often limited to a static suspension. In contrast, R-MHD produces a flat flow profile within a given horizontal plane with low electric fields,[32] facilitating data analysis of the particle motion without worry of particle migration. Uniform fluid flow is especially important when there are other superimposed forces such as Brownian motion.

MHD microfluidics is propelled by the magnetic portion of the Lorentz force, F_B, which

is created when a current flux, **j** (Coul/(s·m^2)) in a fluid (electronic current in a liquid metal or ionic current in a gas or solution) passes orthogonally to a magnetic flux, **B** (T), and follows the right hand rule, [32-36]

$$\mathbf{F_B} \;=\; \mathbf{j} \times \mathbf{B}. \quad (5.1)$$

This relationship gives MHD its unique ability to program microfluidics—to stop, start, reverse, and tune flow without requiring valves or retooling a device. To facilitate this pumping approach on a small scale, a sample solution containing electrolyte is added to a chip that is patterned with individually addressable electrodes and placed on a permanent magnet. Electronic current is passed between at least two electrodes, which converts the electronic current to ionic current at the electrode/solution interface when a redox species[37-42] in solution or immobilized on the electrodes[32, 43] are oxidized and reduced.

Combining microscopy with RMHD has provided key insights into the mechanisms and usefulness of the pair. Optical microscopy combined with RMHD microfluidics has characterized velocity in horizontal planes as a function of different conditions and geometries. In these cases, microspheres with 10 µm diameter were added to the solution to track the fluid flow.[32, 38, 44] Here, R-MHD microfluidics employing PEDOT is used for sample analysis of the smallest particles pumped by this approach to-date, and provides the precise control needed to enable Flow-DFM for nanoparticles. Flow-DFM is used to identify, quantify, and size a flowing suspension mixture of two types of particles (Ag and Au@Si) in a volume beyond the confines of the microscope's viewing window. The particle groups could be differentiated from each other based on their LSPR wavelengths[13] and the diffusion coefficients determined from the moving suspension. Additionally, the pumping direction was reversed to provide multiple observations of the same mixture sample, allowing for more statistically relevant information about the size

distribution to be obtained.

5.3 Experimental

5.3.1: Chemicals and Materials

UV-treated ultrapure water (Thermo Scientific Barnstead GenPure xCAD Plus) exhibiting a conductivity of 0.055 µS cm^{-1} (18.2 MΩ) at 23 °C was used. The citrate-capped silver nanoparticles (AgNP, reported by the manufacturer to be 70 nm with a zeta potential of -41 mV) and spherical PVP-capped gold-coated silica particles (Au@SiNP, reported by the manufacturer to be 137 nm with a zeta potential of -31 mV) depicted in Figure 5.1 were purchased from *nanoComposix Inc.* (Prague, Czech Republic). Potassium nitrate (KNO$_3$) of 99.999 % purity and the propylene carbonate (PC) were purchased from *Sigma-Aldrich* (Germany). The 3,4-ethylenedioxythiophene (EDOT) was purchased from *Sigma-Aldrich* (St. Louis, Missouri, USA). Tetra-n-butylammonium hexafluorophosphate (TBAPF$_6$) was of 98 % purity obtained from Alfa Aesar by Thermo Fisher (Kandel) GmbH. The edge connector (solder contact, 20/40 position, and 0.05 in. pitch) was acquired from Sullins Electronics Corp. (San Marcos, CA, USA). Borosilicate glass wafers (Borofloat 33, 125 mm ± 0.2 mm outer diameter, 700 µm ± 100 µm thickness) were obtained from Mark Optics, Inc. (Santa Ana, CA, USA). The NdFeB ring magnet was purchased from Conrad Electronic SE. The cover slip (Menzel-Glas) with a dimension of 20 x 20 mm was purchased from Thermo Fischer Scientific.

5.3.2: Preparation of PEDOT-modified chip electrodes

Gold band electrodes with a chromium adhesion layer (nominally, 650 µm wide, 1.5 cm long, and 0.25 µm thick) were patterned onto a borosilicate glass wafer via conventional photolithography, similar to that previously described for silicon wafers.[45] The patterned wafer was then diced into 2.54 cm x 5.08 cm (1 in x 2 in) chips. The separation of the inner pair of

electrodes which were activated for R-MHD pumping measures 0.47 cm. The outermost band electrodes and other smaller electrodes on the chip were not used in the studies reported here.

Prior to electropolymerization of PEDOT, the chip was gently cleaned with a Kim Wipe in a sequence of solvents (acetone, ethanol, isopropyl alcohol, and water), rinsed with water, plasma cleaned (Model 1070 NanoClean, Fischione Instruments, Inc.) for 7 min in 25 % O_2 and 75 % Ar at 2 x 10^{-2} torr, 46 W with 1.31 W reflected, and then immediately immersed into the electropolymerization solution of 0.01 M EDOT and 0.10 M $TBAPF_6$ in PC. When ready for deposition, the chip was removed from the solution and contact pads quickly wiped with a PC-soaked Kimwipe, then water and wiped dry. The contact pads were inserted into the edge connector and the chip was re-immersed sufficiently for the solution to cover the band electrodes. A thick film of PEDOT was electropolymerized onto each band electrode based on a previously described procedure[32] using cyclic voltammetry (CV). A PalmSens4 (Palmsens, Houten, Netherlands), Ag/AgCl (3M KCl) reference electrode, and a platinum counter electrode were used for the deposition. There were 24 sequential CV cycles performed at 0.050 V/s between -0.4 V and 1.6 V vs. Ag/AgCl (3M KCl). The deep purple PEDOT films were further stabilized in a solution of 0.10 M $TBAPF_6$ in PC by shorting them together and cycling ten times from 0 V to 0.5 V and back vs. Ag/AgCl (3M KCl) at 0.010 V/s, yielding the typical shape with charging current usually associated with a capacitor.[43] The chip was then rinsed with PC and water, and stored in water until use for R-MHD pumping studies.

5.3.3: The R-MHD Flow-DFM Experimental Setup

Optical tracking of the NPs with DFM while interfaced to R-MHD microfluidics was achieved by the assembly depicted in Figure 5.2-a. DFM was performed using an Olympus BX43 Microscope equipped with an infinity corrected 10X Plan n Achromat Objective (0.25

aperture, no defined cover slip thickness, field number 22), a CytoVita Optical Illuminator

incorporated with a halogen lamp and liquid light guide, and a Retiga RI OEM CCD camera.

Light generated by the halogen lamp was focused and aligned by the illuminator towards the

sample. In DFM, non-scattered light is blocked by apertures while light specifically scattered by

the sample reaches the objective. Due to this, only light which interacts with the sample is

detected, and all else appears black under the DFM.

The RMHD apparatus (Figure 5.2-b) containing the suspension of nanoparticles was

placed in a 3D-printed polylactic acid (PLA) holder on the stage of the DFM microscope. This

apparatus consisted of a transparent electrochemical cell that was coupled with the NdFeB

permanent magnet to provide **B** and connected to a galvanostat/potentiostat to allow activation of

the pumping electrodes on the chip for controlling **j,** therefore engage R-MHD microfluidics. A

700 µm thick poly(dimethylsiloxane) (PDMS) film was first placed on the chip, then 700 µL of a

nanoparticle suspension was pipetted into it and topped with a cover slip and excess particle

suspension carefully blotted with a Kimwipe. The PDMS served as a gasket between the

electrode chip and cover slip to prevent leakage and its opening formed the shape and height of

the solution chamber. Leads from the galvanostat/potentiostat were connected to the contact

pads through silver wires that were adhered to the contact pads on the chip with conductive

copper tape.

A ring magnet with outer diameter of 24.75 mm, and thickness of 2.5 with a 5-mm wide

hole was placed on top of the cover slip. The hole in the center of the magnet is necessary for

transmission of light. The outer dimensions of the magnet were chosen to be as large as possible

to maximize the magnetic flux but would be small enough for the assembly to fit on the stage

between the objective lens and the light source when combined with the electrochemical

chamber. The magnetic flux measured 270 mT at the center of the hole in the location which was in contact with the assembly's cover slip.

5.4.4: Operation and characterization for RMHD-DFM pumped nanoparticles

Three different nanoparticle suspensions were evaluated by DFM. One contained 140 nm Au@SiNP in 50 mM KNO_3, another contained 82 nm AgNP in 50 mM KNO_3, and the other was prepared as a 50/50 mixture of the AgNPs and Au@SiNPs in 50 mM KNO_3. The separate suspensions of Au@SiNPs and AgNPs were used to confirm the LSPR color associated with each particle, and to confirm that the particles would not agglomerate significantly in the 50 mM KNO_3 electrolyte during the studies. All suspensions were sonicated for approximately 7 s immediately prior to use.

For R-MHD pumping studies, one PEDOT-modified gold electrode was used as the working electrode (WE), and another was used as a combined counter and reference electrode (CE/RE). The PalmSens4 was used to perform chronopotentiometry (CP) with three sequential, 15-s current steps, starting at +50 µA, switching to -50 µA, and then repeating +50 µA. This sequence was carried out both in the presence and in the absence of the magnet. The latter served as a control experiment to determine underlying motion that is independent of R-MHD microfluidics

Characterization of nanoparticles

Scanning transmission electron microscopy (STEM) images of nanoparticles to determine size were recorded on a *JEOL JEM-2800* electron microscope equipped with *Schottky* electron gun working at 200 kV. Point-to-point resolution is 0.14 nm. Elemental mapping by energy dispersive X-ray spectroscopy (EDS) was obtained with *JEOL double SDD* X-ray detectors, with a 133 eV spectral resolution, a solid angle of 0.98 sr and a detection area of

100 mm^2. The EDS results confirmed the manufacturer's stated composition of the nanoparticles.

Each sample was prepared by drop casting the nanoparticle suspensions on a *PLANO S-160*

TEM grid (carbon film on 200 mesh copper grid). The particles measured 82 ± 8.4 nm and

140 ± 9.9 nm for the AgNP and Au@SiNP, respectively. The EDS confirmed the elemental

composition of the particles. Dynamic light scattering was performed with a *Zetasizer Ultra*

purchased from M*alvern Panalytical GmbH.* The nanoparticle suspension was measured in a

polystyrol/polystyrene with a HE-Ne Laser of 633 nm.

 To determine the color assignments for the two kinds of nanoparticles used here, a pure

suspension of Au@SiNPs in 50 mM KNO$_3$ was analyzed using ImageJ. Using the color

threshold tool in ImageJ, the red/orange group (hues 0-55) were assigned to Au@SiNPs and the

blue/green group (hues 56-255) were assigned to AgNPs. The video for the mixed particle

suspension was then converted to individual frames, imported as an image sequence, and filtered

to produce two sets of images using the appropriate settings by adjusting the color threshold.

Black was chosen to replace all "filtered" colors. After color separation, the *MosaicSuite* plugin[46]

for *Image J* was used to track the particles and provide the (x,y) coordinates of each particle

track.

5.4 Results and Discussion

R-MHD-DFM tracking of AgNPs and Au@SiNPs and comparison to TEM results

 Figure 5.1 depicts the TEM images of the AgNPs and Au@SiNPs. The shapes are semi-

spherical, and the diameters measure of 82 ± 8.4 nm and 140 ± 9.9 nm, respectively. The

standard deviation around the average diameter for the Au@SiNPs brackets the manufacturer's

reported diameter of 137 nm. However, that for the AgNPs is higher than and does not include

the source's 70 nm specification. The LSPR of these particles appears blue/green for the AgNPs

and red/orange for the Au@SiNPs. Figure 5.3 is a still image taken by DFM of a mixture in the R-MHD apparatus without pumping. The count of particles belonging to the two different populations based on the color differentiation yields a measured ratio of AgNPs to Au@SiNPs in the suspension of 58 ± 6 % to 42 ± 6 %, respectively.

Due to physical limitations, only the lowest objective fit with the experimental cell and thus the LSPR images have relatively low resolution. A pixel is 653 nm, which is ~10x larger than the smaller particles. This is primarily a result of the 10X objective needed to clear the height of the R-MHD apparatus. Other microscope components could be considered for DFM to improve the resolution. However, as is demonstrated later, DFM coupled with R-MHD flow is more forgiving so that higher spatial resolution is not as important in obtaining accurate mean squared displacements.

5.4.1: The effect of R-MHD on nanoparticle motion

To engage RMHD fluid flow of the nanoparticle suspension, an electronic current of 50 µA was applied between the two PEDOT-modified electrodes in the presence of the magnet. The oxidation of PEDOT attracts anions from solution to compensate charge (and repels cations) and the opposite process occurs at the cathode, thus creating an ionic current between them. The small ratio of 0.15 for the height of the chamber to the separation between the active band electrodes is expected to produce a relatively parallel ionic current distribution between the electrodes and across the gap (in the y-direction). The MHD force that the ions experience in the presence of the magnetic field (in the z-direction), which is primarily orthogonal to the ionic current, moves them along the length of the gap between the electrodes (in the x-direction). A momentum transfer occurs to the surrounding fluid around those ions, resulting in "pumping" of fluid in that direction. Because PEDOT holds a finite amount of charge, its pumping duration is

also finite.[34] However, it can be recharged by reversing the current, which reverses flow in the presence of a fixed magnetic field. This causes the reversibility of pumping that was used for the multiple analysis of the same particles.

Video of LSPR of the mixture of nanoparticles obtained by the DFM in the presence of a magnet depicts what appears to be random particle movement, presumably due to Brownian motion, when the pumping electrodes are off. A net translation in the x-direction is superimposed on the random movement when the electrodes are activated with 50 µA, a quick change to translation in the –x-direction occurs when the current is switched to -50 µA, and a reversal of direction again in the +x-direction happens when the current goes back to +50 µA. Figure 5.4 shows the tracks over the course of 74 frames in the (a) absence of a magnet and (b) presence of a magnet during one direction of R-MHD flow. When the current returns to zero, translation in the x-direction ends and random movement remains. The R-MHD creates an easily reversible "pump" by merely switching the polarity of the electrode to reverse the direction of the fluid movement, so long as the magnet orientation remains unchanged.

The particles do not translate in a true x-direction during R-MHD pumping. One possible reason for this is a longer portion of one of the electrodes (designated as the CE/RE electrode) is covered with PEDOT than the other, which can skew the direction of the ionic current across the gap and therefore skew the fluid flow off the central axis. Another possible reason is migration of the slightly negatively charged particles toward the positive electrode. However, there is no measurable net motion in the direction of the anode or cathode. To determine whether migration is affecting the particles, the same type of experiment was performed but without the magnet. Figure 5.4-a illustrates that there is no discernable translation upward or downward toward the electrodes during the application of current. This is indicative that the electric field has little

effect on the motion of the particles, if at all.

One video depicted, however, a global movement of particles to the left regardless of the application and direction of current, but is much slower than the speed of the R-MHD flow attained in the presence of the magnet. The global drift in the absence of a magnet and applied current is depicted in Figure 5.6, where the crosshairs are placed at (0,0). With normal Brownian motion, it is expected that the net change of the particle population would be 0 μm, given a large enough population and Δt. There is no confirmed explanation for this slow drift at this time, but it may be related to a slow leak in the PDMS cell. The particles also remain within the focal plane for the duration of the experiment. Because the materials contained in the particles are not paramagnetic, we do not expect any motion toward higher magnetic field gradients and flux densities, which would be upward (in the z-direction) toward the magnet and sideways toward the edges of the hole when the magnet is in place, and not the indicated x-direction.

To observe the Brownian motion of nanoparticles in a moving suspension, the fluid velocity must be slow enough for several random steps to be visible while the nanoparticles remain in the field of view. The average speed of the RMHD flow under our conditions was measured to be 13.9 ± 1.48 μm·s^{-1} for the blue/green particles and 13.8 ± 1.36 μm·s^{-1} for the red/orange particles, assuming that a measurement of the translation of the nanoparticles is a good reflection of the fluid speed. Analysis of individual video portions is summarized in Table X. The pumping speeds were determined by dividing the distance between the first and last point of the particle tracks by the time between those positions and then averaged. Previous R-MHD microfluidics at the same current of 50 μA, and a similar electrode design and chamber height attained speeds of 50 μm/s, but with a 370 mT disk magnet and ionic strength of 0.16 M, and a gap between pumping electrodes of 3.0 mm.[43] Accounting for the lower magnetic flux and ionic

strength reported here, which should scale the speed proportionally, the predicted fluid speed is 11 µm/s. The decreased viscosity increases the expected speed[45], which is consistent with the observed value here.

The velocity within individual particle tracks varied significantly due to the contribution from the particles' random motion, which is most noticeable by sideways deviations from a line connecting the starting and ending position. Because Brownian motion along the R-MHD-driven translation is expected to be random (equal displacements in forward and reverse directions), it should not affect the measurement of the fluid speed. The R-MHD fluid speed is consistent with expectations for the conditions used here.

5.4.2: Determination of diffusion coefficients and size of nanoparticles in the absence of R-MHD flow

Diffusion coefficients and sizes of the different populations of AgNPs and Au@SiNPs in the mixture were determined first in the absence of R-MHD flow, under conditions without a magnet but with the current engaged. This exercise sets a baseline for obtaining information and provides insight into whether migration is of significance or not. Mean square displacement (MSD) plots, which have been previously used for the sizing of individual particles,[13, 19, 47, 48] were generated for each particle. Each individual frame was treated as a different time step, and the average MSD value for each step one through five were used to create the plots (Figure 5.7). From these plots, the diffusion coefficients for each particle can be extracted from the slope, then the size can be estimated using the *Stokes-Einstein* equation[49] (Equation (5.2)). Note that the scale needed for the smaller blue-green particles is 10x larger than that of the larger red-orange particles, which was to be expected. Any lines with an r^2 of < 0.8 were not included in further analysis.

$$D = \frac{k_B \cdot T}{6\pi \cdot \mu \cdot r} \qquad (5.2)$$

The particles were analyzed with *NanoTrackJ,*[13] the results of which are depicted in

Figure 5.8.The size distributions (Walker's Method) were centered at 105 nm and 135/139 nm

for the blue/green and red/orange groups, respectively. The total number of particles tracked in

the mixture was 733. The blue/green group contained 384 particles and the red/orange group

contained 389 particles, indicating that the color analysis built into *ImageJ* was sufficient for the

microscope and camera settings required for paring with the magnet, though only a low

magnification objective was used. Using our 1-dimensional MSD method, 417 blue/green and

360 red/orange particles were tracked. The histograms were centered at 82.5 nm and 165 nm for

the blue/green and red/orange groups, respectively. This method agrees with the TEM

determined sizes of 82 ± 8.4 nm and 140 ± 9.9 nm. The similarity of the sizes determined by

MSD under an applied current and the TEM provides further support that migration is not

playing a significant role in the mass transport of the nanoparticles. Table 1 lists the particle sizes

for both nanoparticle populations.

5.4.3: Determination of diffusion coefficients and size of nanoparticles in the presence of R-

MHD flow

Analysis of the sizes of particles and their diffusion coefficients in the presence of R-MHD flow

was carried out in a similar way as for the case without flow, with a few notable exceptions and

benefits that arise when there is flow. Because the motion of nanoparticles during R-MHD flow

was slightly skewed, the video images were all rotated 12° to align the fluid pumping with the x-

axis. Since the movement in the x direction was assumed to be dominated by R-MHD, only the y

dimension was used to create the plots of MSD vs. Time Step (τ). This approach also has the

advantage that the large displacement in x arising from the fluid flow more than offsets the low

resolution and facilitates measurement of displacement due to Brownian motion. One-

dimensional MSD curves were created from displacement along the y-axis with $\tau = 1$-5 (Figure

5.8). The diffusion coefficients were extracted from the slope, and the *Stokes-Einstein* equation

was used to estimate the particle sizes. Three pumping excursions were performed by switching

the applied current: forward 1, reverse, and forward 2. For each color associated with the

nanoparticles, the forward 1, reverse, forward 2 segments of the video were analyzed separately.

The size distributions are shown in Figures 5.9 for the AgNPs and Au@SiNPs. The results are

also summarized in Table 1, alongside the results in the absence of the magnet. Particles larger

than 500nm were filtered from the histograms. As depicted in Figure 5.9 (left), with the magnet

in place the blue/green group had histograms centered around 87.5 and 67.5 nm for the pumped

suspension, and 82.5 nm for the non-pumped suspension. Figure 5.9 (right) depicts that the

red/orange groups were centered at 127.5 and 117.5 nm for the pumped suspensions, and 165 nm

for the non-pumped suspension. These results are consistent with those obtained in the absence

of R-MHD pumping, and compare similarly with the sizes obtained by TEM, validating the

method of using 1D MSD curves to size nanomaterials in a pumped suspension.

5.5 Conclusion

      Combining dark field microscopy with Redox-magnetohydrodynamics allows for

high-throughput analysis of nanoparticle mixtures. The adaptations made to previously used R-

MHD systems still allow for the precisely controlled motion of fluid within the DFM field of

view, allowing for the pumpless movement of nanoparticles. Figure 5.10 indicates that measured

sizes are similar to the TEM and DLS data when compared to the respective pure suspensions.

Hence it can be concluded that R-MHD-DFM is a strong method to efficiently obtain size, LSPR

information, and particle behaviors *in situ* and *operando* of non-paramagnetic nanoparticles

particles during precisely controlled fluid motion, leading to an increase in the sampling

capabilities. Additionally, the sizes of the particles can be estimated while they are in motion by

calculating their respective 1-diminsional mean square displacements.

References

1.   Herves, P.; Perez-Lorenzo, M.; Liz-Marzan, L.; Dzubiella, J.; Lu, Y.; Ballauff, M., Catalysis by metallic nanoparticles in aqueous solution: model reactions. *Chemical Society Reviews* **2012,** *41* (17), 5577-5587.

2.   Ananikov, V. P.; Beletskaya, I. P., Toward the Ideal Catalyst: From Atomic Centers to a "Cocktail" of Catalysts. *Organometallics* **2012,** *31* (5), 1595-1604.

3.   Wildgoose, G. G.; E., C.; Compton, R. G., Metal Nanoparticles and Related Materials Supported on Carbon Nanotubes: Methods and Applications. *Small* **2005,** *2* (2), 182-193.

4.   Dakal, T.; Kumar, A.; Majumdar, R.; Yadav, V., Mechanistic Basis of Antimicrobial Actions of Silver Nanoparticles. *Frontiers in Microbiology* **2016,** *7*.

5.   El Arrassi, A.; Bellova, P.; Javid, S.; Motemani, Y.; Khare, C.; Sengstock, C.; Koller, M.; Ludwig, A.; Tschulik, K., A Unified Interdisciplinary Approach to Design Antibacterial Coatings for Fast Silver Release. *Chemelectrochem* **2017,** *4* (8), 1975-1983.

6.   Robbins, E. J.; Leckenby, R. E.; Willis, P., The ionization potentials of clustered sodium atoms. *Advances in Physics* **1967,** *64*, 739-744.

7.   Liang, T.; Zhou, D.; Wu, Z.; Shi, P., Size-dependent melting modes and behaviors of Ag nanoparticles: a molecular dynamics study - IOPscience. *Nanotechnology* **2017,** *28* (48), 1-15.

8.   de Heer, W. A., The physics of simple metal clusters: experimental aspects and simple models. *Reviews of Modern Physics* **1993,** *65* (3), 611-676.

9.   Chao, Y.-J.; Lyu, Y.-P.; Wu, Z.-W.; Lee, C.-L., Seed-mediated growth of Ag nanocubes and their size-dependent activities toward oxygen reduction reaction. *International Journal of Hydrogen Energy* **2016,** *41* (6), 3896–3903.

10.   and, R. N.; El-Sayed, M. A., Shape-Dependent Catalytic Activity of Platinum Nanoparticles in Colloidal Solution. *Nano Letters* **2004,** *4* (7), 1343-1348.

11.   Liz-Marzán*, L. M., Tailoring Surface Plasmons through the Morphology and Assembly of Metal Nanoparticles. *Langmuir* **2006,** *22* (1), 32-41.

12.   Faraday, M., Experimental relations of gold (and other metals) to light. *Philosophical Transactions* **1857,** *147*, 145-181.

13.   Wagner, T.; Lipinski, H. G.; Wiemann, M., Dark field nanoparticle tracking analysis for size characterization of plasmonic and non-plasmonic particles. *Journal of Nanoparticle Research* **2014,** *16* (5), 2419-2434.

14.   Xiaohua Huang; Ivan H. El-Sayed; Wei Qian, a.; Mostafa A. El-Sayed*, Cancer Cell Imaging and Photothermal Therapy in the Near-Infrared Region by Using Gold Nanorods. *Journal of the American Chemical Society* **2006,** *128* (6), 2115-2120.

15.   and, A. D. M.; Duyne*, R. P. V., Single Silver Nanoparticles as Real-Time Optical Sensors with Zeptomole Sensitivity. *Nano Letters* **2003,** *3* (8), 1057-1062.

16.   Leif J. Sherry; Shih-Hui Chang; George C. Schatz, a.; Duyne*, R. P. V.; and, B. J. W.; Xia, Y., Localized Surface Plasmon Resonance Spectroscopy of Single Silver Nanocubes. *Nano Letters* **2005,** *5* (10), 2034-2038.

17.   Wonner, K.; Evers, M. V.; Tschulik, K., Simultaneous Opto- and Spectro-Electrochemistry: Reactions of Individual Nanoparticles Uncovered by Dark-Field Microscopy. **2018**.

18.   Want, H.; Zhang, T.; Zhou, X., Dark-field spectroscopy: development, applications and perspectives in single nanoparticle catalysis - IOPscience. *Journal of Physics: Condensed Matter* **2019,** *31*, 473001 1-14.

19.   Wang, K.; Shangguan, L.; Liu, Y.; Jiang, L.; Zhang, F.; Wei, Y.; Zhang, Y.; Qi, Z.; Wang, K.; Liu, S., In Situ Detection and Imaging of Telomerase Activity in Cancer Cell Lines via Disassembly of Plasmonic Core–Satellites Nanostructured Probe. *Analytical Chemistry* **2017,** *89* (13).

20.   Wonner, K.; Rurainsky, C.; Tschulik, K., Operando Studies of the Electrochemical Dissolution of Silver Nanoparticles in Nitrate Solutions Observed With Hyperspectral Dark-Field Microscopy. *Frontiers in Chemistry* **2020,** *7*.

21.   Matsuura, Y.; Ouchi, N.; Nakamura, A.; Kato, H., Determination of an accurate size distribution of nanoparticles using particle tracking analysis corrected for the adverse effect of random Brownian motion. *Physical Chemistry Chemical Physics* **2018,** *20* (26), 17839-17846.

22.   Ma, W.; Ma, H.; Chen, J.; Peng, Y.; Yang, Z.; Wang, H.; Ying, Y.; Tian, H.; Long, Y., Tracking motion trajectories of individual nanoparticles using time-resolved current traces. *Chemical Science* **2017,** *8* (3), 1854-1861.

23.   Lee, B.; Park, H., HybTrack: A hybrid single particle tracking software using manual and automatic detection of dim signals. *Scientific Reports* **2018,** *8*.

24.   Zhang, F.; Durham, P.; Sayes, C. M.; Lau, B. L. T.; Bruce, E. D., Particle uptake efficiency is significantly affected by type of capping agent and cell line. *Journal of Applied Toxicology* **2015,** *35*, 1114-1121.

25.   NanoTechnology, C. f. t. E. I. o. Silver Nanoparticles May Adversely Affect Environment | Center for the Environmental Implications of NanoTechnology. http://ceint.duke.edu/news-events/silver-nanoparticles-may-adversely-affect-environment (accessed 02/26/2017).

26.   Li, X.; Lenhart, J.; Walker, H., Aggregation Kinetics and Dissolution of Coated Silver Nanoparticles. *Langmuir* **2012,** *28* (2), 1095-1104.

27.   V, V.; C, C.; G, K.; S, C.; E, P.; B, L.; JP, T., Neuronal cytotoxicity and genotoxicity induced by zinc oxide nanoparticles. *Environment International* **2013,** *55*, 92–100.

28.   Gorka, D. E.; Osterberg, J. S.; Gwin, C. A.; Colman, B. P.; Meyer, J. N.; Bernhardt, E. S.; Gunsch, C. K.; DiGulio, R. T.; Liu, J., Reducing Environmental Toxicity of Silver Nanoparticles through Shape Control. *Environmental Science & Technology* **2015,** *49*, 10093-10092.

29.   Loza, K.; Diendorf, J.; Sengstock, C.; Ruiz-Gonzalez, L.; Gonzalez-Calbet, J.; Vallet-Regi, M.; Koller, M.; Epple, M., The dissolution and biological effects of silver nanoparticles in biological media. *Journal of Materials Chemistry B* **2014,** *2* (12), 1634-1643.

30.   Ghosal, S., Fluid mechanics of electroosmotic flow and its effect on band broadening in capillary electrophoresis. *Electrophoresis* **2004,** *25* (2), 214-228.

31.   Zeng, W.; Jacobi, I.; Beck, D.; Li, S.; Stone, H., Characterization of syringe-pump-driven induced pressure fluctuations in elastic microchannels. *Lab on a Chip* **2015,** *15* (4), 1110-1115.

32.   Nash, C. K.; Fritsch, I., Poly(3,4-ethylenedioxythiophene)-Modified Electrodes for Microfluidics Pumping with Redox-Magnetohydrodynamics: Improving Compatibility for Broader Applications by Eliminating Addition of Redox Species to Solution. *Analytical Chemistry* **2016,** *88* (3), 1601-1609.

33.   Fritsch, I.; Carter, C. S.; Aguilar, Z. Microfluidics and small volume mixing based on redox magnetohydrodynamics methods. 2004.

34.   Khan, F.; Hutcheson, J.; Hunter, C.; Powless, A. J.; Benson, D.; Fritsch, I.; Muldoon, T. J., Redox-Magnetohydrodynamically Controlled Fluid Flow with Poly(3,4-ethylenedioxythiophene) Coupled to an Epitaxial Light Sheet Confocal Microscope for Image Cytometry Applications. *Analytical Chemistry* **2018,** *90* (13), 7862-7870.

35.   Leventis, N.; Gao, X., Magnetohydrodynamic electrochemistry in the field of Nd-Fe-B magnets. Theory, experiment, and application in self-powered flow delivery systems. *Analytical Chemistry* **2001,** *73* (16), 3981-3992.

36.   Leventis, N.; Xuerong, G., Nd−Fe−B Permanent Magnet Electrodes. Theoretical Evaluation and Experimental Demonstration of the Paramagnetic Body Forces. *Journal of the American Chemical Society* **2002,** *124* (6), 1079-1088.

37.   Ensafi, A.; Nazari, Z.; Fritsch, I., Redox magnetohydrodynamics enhancement of stripping voltammetry of lead(II), cadmium(II) and zinc(II) ions using 1,4-benzoquinone as an alternative pumping species. *Analyst* **2012,** *137* (2), 424-431.

38.   Anderson, E.; Weston, M.; Fritsch, I., Investigations of Redox Magnetohydrodynamic Fluid Flow At Microelectrode Arrays Using Microbeads. *Analytical Chemistry* **2010,** *82* (7), 2643-2651.

39.   Weston, M.; Anderson, E.; Arumugam, P.; Narasimhan, P.; Fritsch, I., Redox magnetohydrodynamic enhancement of stripping voltammetry: toward portable analysis using disposable electrodes, permanent magnets, and small volumes. *Analyst* **2006,** *131* (12), 1322-1331.

40.   Weston, M.; Nash, C.; Fritsch, I., Redox-Magnetohydrodynamic Microfluidics Without Channels and Compatible with Electrochemical Detection Under Immunoassay Conditions. *Analytical Chemistry* **2010,** *82* (17), 7068-7072.

41.   Anderson, E.; Fritsch, I., Factors influencing redox magnetohydrodynamic-induced convection for enhancement of stripping analysis. *Analytical Chemistry* **2006,** *78* (11), 3745-3751.

42.   Arumugam, P.; Fakunle, E.; Anderson, E.; Evans, S.; King, K.; Aguilar, Z.; Carter, C.; Fritsch, I., Characterization and pumping - Redox magnetohydrodynamics in a microfluidic channel. *Journal of the Electrochemical Society* **2006,** *153* (12), E185-E194.

43.   Khan, F.; Fritsch, I., Chip-Scale Electrodeposition and Analysis of Poly(3,4-ethylenedioxythiophene) (PEDOT) Films for Enhanced and Sustained Microfluidics Using DC-Redox-Magnetohydrodynamics. *Journal of the Electrochemical Society* **2019,** *166* (13), H615-H627.

44.   Sahore, V.; Fritsch, I., Microfluidic rotational flow generated by redox-magnetohydrodynamics (MHD) under laminar conditions using concentric disk and ring microelectrodes. *Microfluidics and Nanofluidics* **2015,** *18* (2), 159-166.

45.   Sahore, V.; Fritsch, I., Flat Flow Profiles Achieved with Microfluidics Generated by Redox-Magnetohydrodynamics. *Analytical Chemistry* **2013,** *85* (24), 11809-11816.

46.   Sbalzarini, I. F.; Koumoutsakos, P., Feature point tracking and trajectory analysis for video imaging in cell biology. *Journal of Structural Biology* **2005,** *151*, 182-195.

47.   Ernst, D.; Köhler, J., How the number of fitting points for the slope of the mean-square displacement influences the experimentally determined particle size distribution from single-particle tracking. *Physical Chemistry Chemical Physics* **2013,** *15* (10), 3429-3432.

48.   Tinevez, J.; Perry, N.; Schindelin, J.; Hoopes, G.; Reynolds, G.; Laplantine, E.; Bednarek, S.; Shorte, S.; Eliceiri, K., TrackMate: An open and extensible platform for single-particle tracking. *Methods* **2017,** *115*, 80-90.

49.   Miller, C. C., The Stokes-Einstein law for diffusion in solution. *Royal Society of Chemistry* **1924,** *106*, 724.

50.   Wegner, K.; Ly, H.; Weiss, R.; Pratsinis, S.; Steinfeld, A., In situ formation and hydrolysis of Zn nanoparticles for H-2 production by the 2-step ZnO/Zn water-splitting thermochemical cycle. *International Journal of Hydrogen Energy* **2006,** *31* (1), 55-61.

Tables

Table 5-1: RMHD pumping speeds determined from a mixture of Ag and Au@Si nanoparticles in 50 mM KNO_3. The distance traveled for each particle between the first and last frame in the track was assumed to be the distance contributed by the RMHD flow. The speed was calculated by dividing this distance by the amount of time in which the particle track was visible.

Video	Pumping Speed ($\mu m \cdot s^{-1}$)
	Blue/Green
Forward 1	13.5 ± 1.41
Reverse	14.7 ± 1.38
Forward 2	13.5 ± 1.65
	Red/Orange
Forward 1	13.3 ± 1.52
Reverse	14.5 ± 1.22
Forward 2	13.3 ± 1.52

Table 5-2: Sizes of the particles determined from a mixture of Ag and Au@Si nanoparticles in 50 mM KNO_3 in the presence and absence of RMHD flow. Each particle was first identified by its localized surface plasmon resonance (LSPR) color and its diffusion coefficient determined by the MSD analysis of its motion during RMHD in forward 1, reverse, and forward 2 passes (in the presence of the magnet) and in the absence of the magnet, but with current applied.

| Video	Particle size (nm)	# particles analyzed
	Blue/Green	
Forward 1	Average 153; Peak max 87.5; Median 116	207
Reverse	Average 123; Peak max 87.5; Median 80	230
Forward 2	Average 163; Peak max 67.5; Median 99	240
No magnet	Average 232; Peak max 82.5; Median 150.3	385
	Red/Orange	
Forward 1	Average 144; Peak max 127.5; Median 143	186
Reverse	Average 144; Peak max 127.5; Median 110	164
Forward 2	Average 185; Peak max 117.5; Median 161	125
No magnet	Average 246; Peak max 165; Median 194	335

Figures
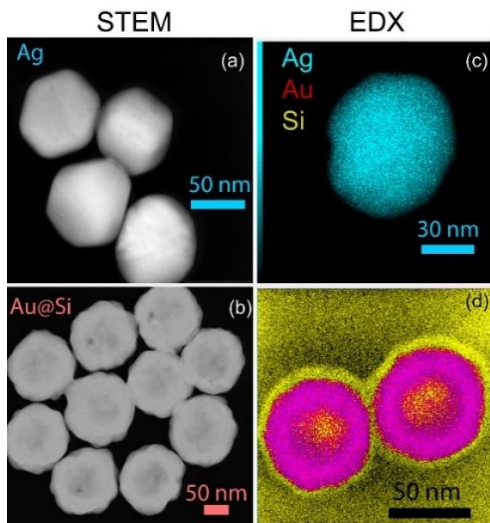
Figure 5.1: STEM and EDX images of the (a and c) 82 ± 8.4 nm AgNPs and (b and d) 140 ± 9.9 nm Au@SiNPs
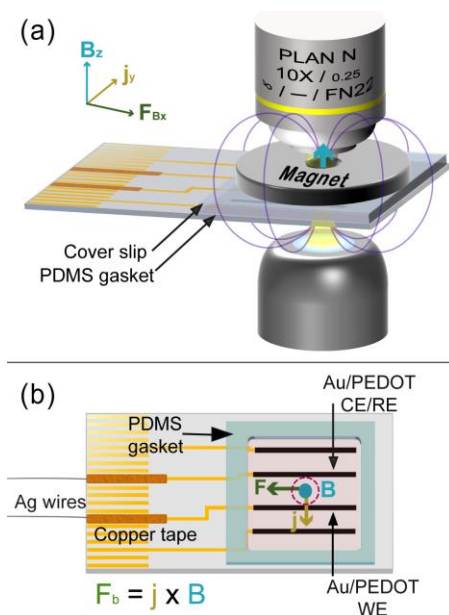

Figure 5.2: The RMHD-DFM setup. (a) The electrochemical cell/magnet assembly used for RMHD-DFM, located between the illuminating system and the microscope objective, the right coordinate system assignments and the directions of applied **j, B** from the magnet**,** and **F$_B$**, which directs fluid flow between the activated electrodes (b) Top-down view of the electrochemical portion of the RMHD assembly showing the innermost band electrodes that are activated. The region inside the PDMS gasket contains the nanoparticle suspension. The DFM viewing field of the microscope is indicated in the dashed circle.
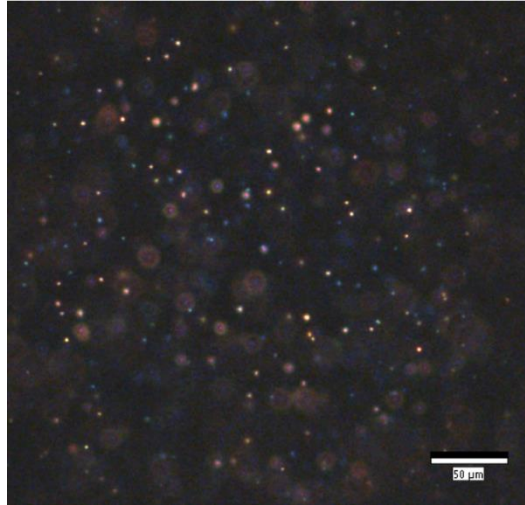
Figure 5.3: DFM image of the mixed Ag and Au@Si particle suspension in 50 mM KNO₃. The image is taken from a video recorded during the application of a 50 µA current and in the absence of the magnet (non-pumped).
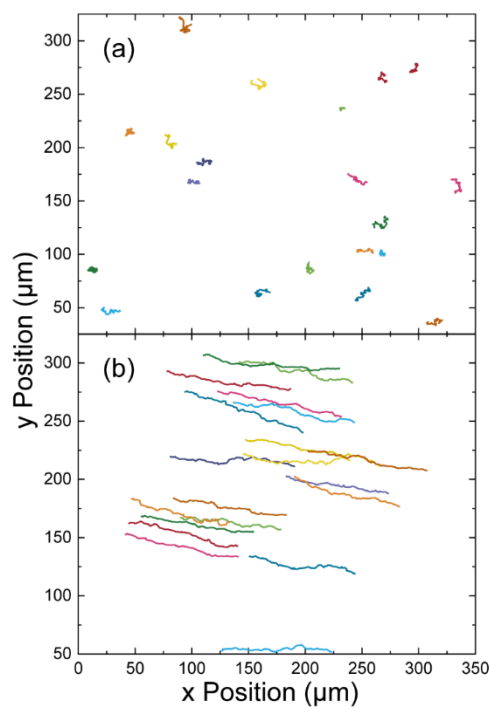

Figure 5.4: Particle tracks of the mixed particle suspension in 50 mM KNO3 over 74 frames during an applied current of 50 µA and in the (a) absence and (b) presence of the magnet.
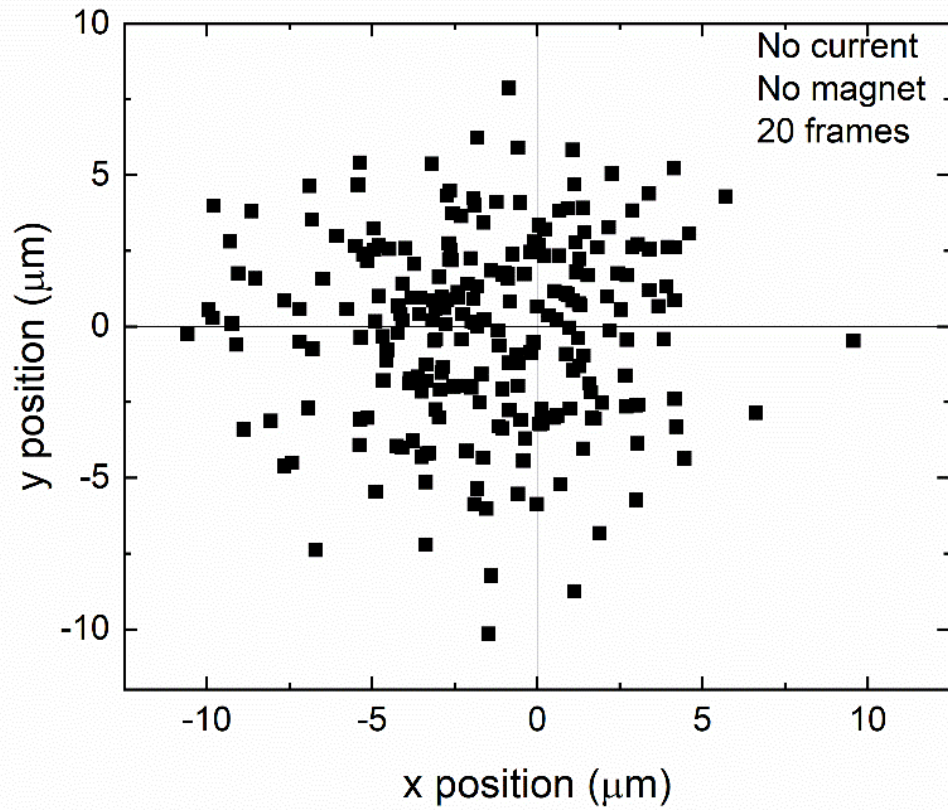
Figure 5.6: Global drift in the beginning and ending positions of the particle mixture over 20 frames in the absence of an ionic current or a magnet.
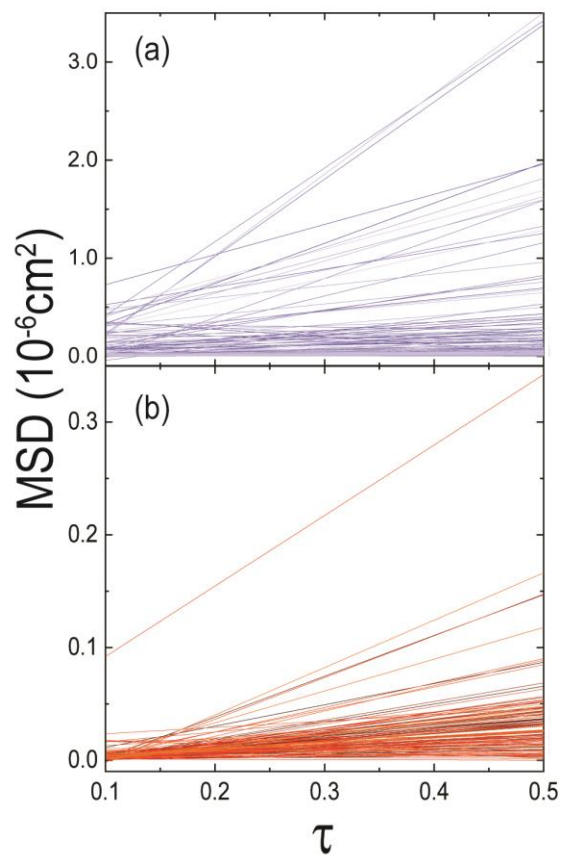
Figure 5.7: 1-D MSD plots generated by time steps 1-5 of each particle in the mixture. Plots were generated from the video recording of RMHD pumping in the forward 1 direction of (A) AgNPs and (B) Au@SiNPs. Note the diffusion coefficient (calculated from the slope of the least squares fit to a line) is approximately 10x larger for the blue/green AgNP when compared to that of the red Au@SiNP. Of the particles tracked for Ag, 213 tracks produced an $R^2 \geq 0.9$, and 77 gave an $R^2 \geq 0.985$. Lines with negative slopes from some of the particles were due to tracking errors and removed and are not reflected in the histogram of Figure 6. The blue-colored LSPR was not as intense as the red, making tracking more difficult. Of the particles tracked for Au@Si, 141 tracks produced an $R^2 \geq 0.9$, and 93 gave an $R^2 \geq 0.985$.
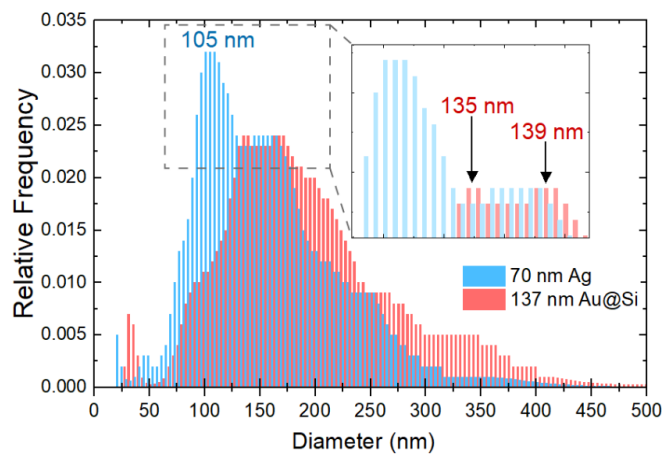
Figure 5.8: The size distributions of the Ag (blue) and Au@Si (red) nanoparticles in the mixture in 50 mM KNO_3 in the absence of a magnetic field and presence of an ionic current (non-pumped), analyzed in NanoTrackJ.[50] For clarity, the inset indicates the maximum peak locations for the Au@Si particles.
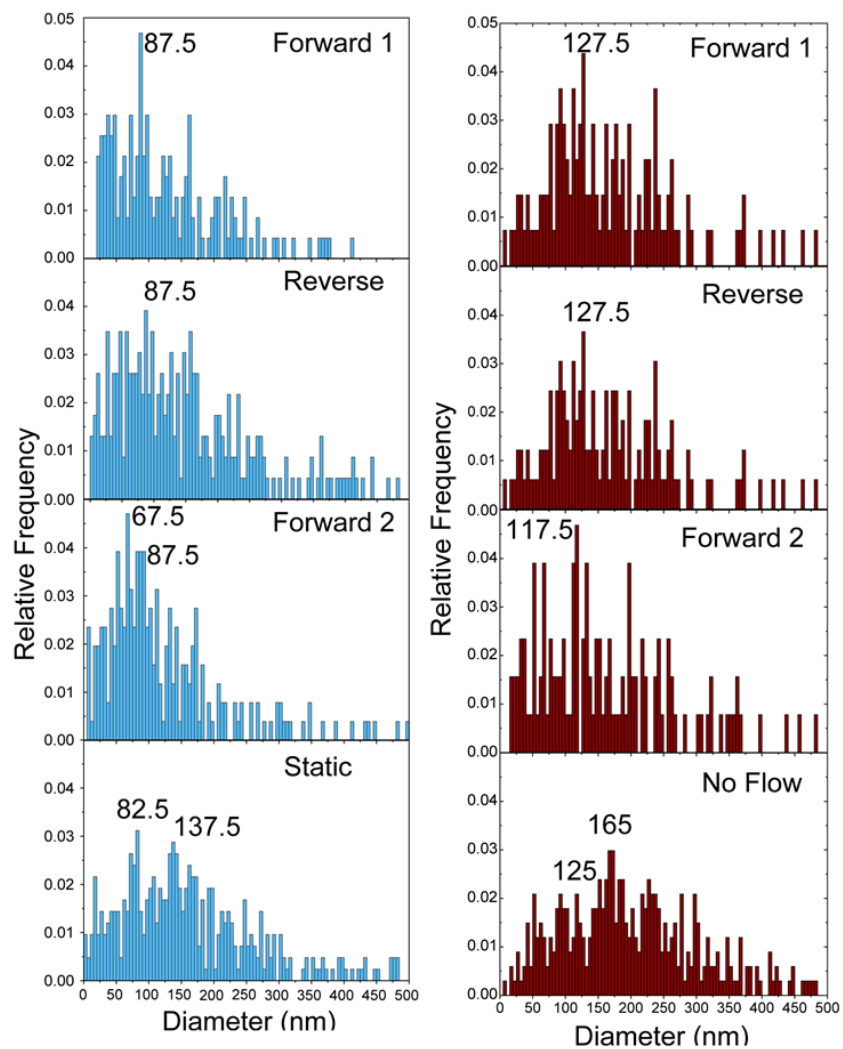
Figure 5.9: Size distributions of the particles with LSPR having hues 56-255, assigned to AgNPs in the mixture and calculated from the 1D mean square displacement of the RMHD-pumped (forward 1, reverse, and forward 2) and of the static suspension.
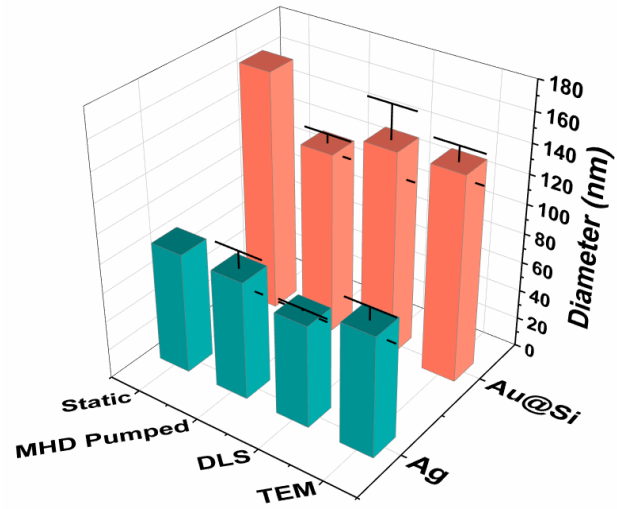
Figure 5.10: Comparison of size determination from several methods. A mixed suspension in 50 mM KNO$_3$ was used for the static and MHD pumped method, and pure nanoparticle suspensions in the absence of KNO$_3$ were used for DLS and TEM.

Chapter 6: Conclusions and future direction

Detection and characterization of individual nanoparticles is important for understanding their fundamental properties, and for predicting the behavior resulting from a change in environment, capping ligand, size, or shape. Electrochemical oxidation allows for a relatively cost-effective method of assessing the electroactive activity of single particles in a suspension and for probing the electrode-particle interface.[1-4] Oxidation through polymer capping ligands adds additional barriers to oxidation of the particle at the electrode,[5] thus the experimental environment needs tailored to the capping ligand in addition to the core particle material. Single particle tracking is an alternative method of single particle characterization, but the system must be carefully controlled and at this time, electrochemical information cannot be obtained from the individual particles during this process.[6-9]

Herein we explored the oxidation of polyethylene glycol (PEG) and poly vinylpyrrolidone (PVP) capped silver nanoparticles and observed the single particle oxidation of silver nanospheres (AgNS), nanocubes (AgNC), and nanoplates (AgNPl). In the presence of KCl, PEG capped particles require a "conditioning time" before particle oxidation occurs upon electrode interaction. Once the particles have conditioned, oxidation and formation of AgCl occurs to completion within a single current spike. Furthermore, higher concentrations of KCl required less conditioning time, indicating that an interaction between the electrolyte and PEG occurs that allows for tunneling through the ligand.

The same procedure is ineffective for oxidation of particles containing PVP as the capping ligand. While performing in-situ cyclic voltametric cleaning of the working electrode in KNO_3, preliminary signs of single particle oxidation of PVP-AgNP appeared when the potential reached around 1500 mV. Chronoamperometric experiments performed at 1500 mV and 1650

mV resulted in single particle oxidative events, but the possible formation of silver superoxide structures[10] and oxidation of water on top of the newly formed silver oxides[11, 12] complicates analysis of the particle spikes. Integration of the spikes occurring at 1500 mV indicated that incomplete particle oxidation was occurring. Integration of the spikes at 1650 mV revealed that oxidation to Ag (I) was likely occurring, but additional chemistry was also present. Further experimentation is needed to determine whether formation of silver superoxides or water oxidation was the contributor to the increased charge passed within the current spike.

Using KOH instead of KNO_3 proved successful in lowering the potential at which single particle oxidation occurs. Not only does the presence of hydroxides lower the potential at which silver oxide is formed,[13, 14] but it also has been documented to increase the conductivity of PVP.[15] Integration of current spikes produced at 900 mV indicated total oxidation of the particles due to formation of Ag (I) occurred within the current spike. Subsequent oxidation to Ag (II) likely occurs,[16] but not at rates detectable in the existing experimental setup and should be confirmed with additional tests.

Both methods of oxidizing PVP capped AgNP allowed for the investigation of particle shape on the current spike produced upon oxidation. Under both sets of conditions, the rate of oxidation was dependent on the total amount of silver present, regardless of particle shape. One explanation is a lattice mismatch which allows the inner layers of silver to oxidize simultaneously with the outer layers, but further experimentation is required. Observation of the shape of the particle immediately prior to and following oxidation could give insight into the morphology changes which occur during the oxidative process.

When it is not ideal to monitor the electrochemical properties of individual particles, single particle tracking can be utilized for observation of particle size.[7] Pairing of dark field

microscopy (DFM) with redox magnetohydrodynamics (RMHD) allowed for the simultaneous pumping and sizing of a mixture of silver and gold shelled silica nanoparticles. However, RMHD requires the presence of an ionic current and magnetic flux.[17] Observation of the particles in the ionic current (**j**) confirmed that the particles motion was not noticeably affected; tracking revealed that migration did not occur towards either electrode. If characterizing smaller particles, quantum dots, or particles containing a higher zeta potential is desired, the effect of the ionic current on the Brownian motion would need to be reobserved. Additionally, the magnetic flux would likely affect paramagnetic particles.

References:

1.   Zhou, Y. G.; Rees, N. V.; Compton, R. G., The Electrochemical Detection and Characterization of Silver Nanoparticles in Aqueous Solution. *Angewandte Chemie International Edition* **2011,** *50* (18), 4219-4221.

2.   Oja, S.; Robinson, D.; Vitti, N.; Edwards, M.; Liu, Y.; White, H.; Zhang, B., Observation of Multipeak Collision Behavior during the Electro-Oxidation of Single Ag Nanoparticles. *Journal of the American Chemical Society* **2017,** *139* (2), 708-718.

3.   Chen, C.-H.; Ravenhill, E. R.; Momotenko, D.; Kim, Y.-R.; Lai, S. C. S.; Unwin, P. R., Impact of Surface Chemistry on Nanoparticle–Electrode Interactions in the Electrochemical Detection of Nanoparticle Collisions. *Langmuir* **2015,** *31*, 11932-11942.

4.   Saw, E. N.; Kratz, M.; Tschulik, K., Time-resolved impact electrochemistry for quantitative measurement of single-nanoparticle reaction kinetics | SpringerLink. *Nano Research* **2017,** *10* (11), 3680-3689.

5.   Toh, H. S.; Jurkschat, K.; Compton, R. G., The Influence of the Capping Agent on the Oxidation of Silver Nanoparticles: Nano-impacts versus Stripping Voltammetry. *Chemistry - A European Journal* **2015,** *21* (7), 2998-3004.

6.   Ernst, D.; Köhler, J., How the number of fitting points for the slope of the mean-square displacement influences the experimentally determined particle size distribution from single-particle tracking. *Physical Chemistry Chemical Physics* **2013,** *15* (10), 3429-3432.

7.   Wagner, T.; Lipinski, H. G.; Wiemann, M., Dark field nanoparticle tracking analysis for size characterization of plasmonic and non-plasmonic particles. *Journal of Nanoparticle Research* **2014,** *16* (5), 2419-2434.

8.   Ma, W.; Ma, H.; Chen, J.; Peng, Y.; Yang, Z.; Wang, H.; Ying, Y.; Tian, H.; Long, Y., Tracking motion trajectories of individual nanoparticles using time-resolved current traces. *Chemical Science* **2017,** *8* (3), 1854-1861.

9.   Tinevez, J.; Perry, N.; Schindelin, J.; Hoopes, G.; Reynolds, G.; Laplantine, E.; Bednarek, S.; Shorte, S.; Eliceiri, K., TrackMate: An open and extensible platform for single-particle tracking. *Methods* **2017,** *115*, 80-90.

10.   Sulc, O., Über das sogenannte elektrolytische Silbersuperoxyd. *Zeitschrift für anorganische Chemie* **1900,** *24* (1), 305-313.

11.   Zhang, F.; Defnet, P. A.; Fan, Y.; Hao, R.; Zhang, B., Transient Electrocatalytic Water Oxidation in Single-Nanoparticle Collision. *Journal of Physical Chemistry C* **2018,** *122* (11), 6447-6455.

12.   Sundaresan, V.; Monaghan, J. W.; Willets, K. A., Visualizing the Effect of Partial Oxide Formation on Single Silver Nanoparticle Electrodissolution. *The Journal of Physical Chemistry C* **2018,** *122*, 3138−3145.

13.   Droog, J. M. M.; Hjuisman, F., Electrochemical Formation and Reduction of Silver Oxides in Alkaline Media. *Journal of Electroanalytical Chemistry* **1980,** *115* (2), 211-224.

14.   Dirkse, T. P., The Oxidation of the Silver Electrode in Alkaline Solutions. *Journal of the Electrochemical Society* **1959,** *106* (11), 920-925.

15.   Hatta, F.; Yahya, M.; Ali, A.; Subban, R.; Harun, M.; Mohamad, A., Electrical conductivity studies on PVA/PVP-KOH alkaline solid polymer blend electrolyte. *Ionics* **2005,** *11* (5-6), 418-422.

16.   Dirkse, T. P.; Wiers, B., The Stability and Solubility of AgO in Alkaline Solutions. *Journal of the Electrochemical Society* **1959,** *106* (4), 284-287.

17.   Leventis, N.; Gao, X., Magnetohydrodynamic electrochemistry in the field of Nd-Fe-B magnets. Theory, experiment, and application in self-powered flow delivery systems. *Analytical Chemistry* **2001,** *73* (16), 3981-3992.